

Improved third harmonic generation and nonlinear beamforming with resonant silicon metasurfaces

Dissertation zur Erlangung des akademischen Titels

Doctor rerum naturalium

(Dr. rer. Nat.)

von

Bernhard Johannes Reineke Matsudo

Gutachter: **Prof. Dr. Thomas Zentgraf**

Prof. Dr. Cedrik Meier

Erklärung der Selbstständigkeit

Hiermit versichere ich die vorliegende Arbeit mit dem Titel „**Improved third harmonic generation and nonlinear beamforming with resonant silicon metasurfaces**“ selbständig verfasst und keine anderen als die angegebenen Quellen und Hilfsmittel verwendet, sowie Zitate kenntlich gemacht zu haben. Diese Arbeit hat in gleicher oder ähnlicher Form noch keiner Prüfungsbehörde vorgelegen.

Bernhard Johannes Reineke Matsudo

Paderborn, Dienstag, 14. Juni 2022

Zusammenfassung

In dieser Arbeit haben wir das nichtlineare geometrische Phasenverhalten von amorphen Silizium Metaoberflächen untersucht. Die Metaoberflächen wurden aus einem dünnen Film aus amorphem Silizium durch Elektronenstrahlolithografie und reaktives Ionenätzen hergestellt. Das geometrische Phasenverhalten und die nichtlineare Umwandlungseffizienz wurden mit Hilfe eines Fourier-Raum Aufbaus untersucht, der es uns ermöglicht, die räumliche Fourier-Transformation der Metaoberflächen auf eine Kamera abzubilden und von dieser auf das Phasenverhalten der Metaoberfläche zu schließen. Um die Phasenantwort bei der Erzeugung der dritten Harmonischen zu untersuchen, haben wir ein Phasenprofil ähnlich einem Blaze-Gitter und ein Multiplex Hologramm kodiert, um die Machbarkeit dieses Ansatzes zu demonstrieren. Zusammenfassend lässt sich sagen, dass die geometrische Phase in den Prozess der nichtlinearen Erzeugung der dritten Harmonischen integriert werden kann und zur Lenkung und Formung des erzeugten Lichts verwendet werden kann. Darüber hinaus erwarten wir unterschiedliche geometrische Phasenreaktionen in Abhängigkeit von der Rotationssymmetrie. Im Falle einer C_1 - oder C_2 -Rotationssymmetrie ist die geometrische Phase proportional zum 2-fachen Drehwinkel bei Kopolarisation und zum 4-fachen Drehwinkel bei Kreuzpolarisation. Da die geometrische Phase in zwei orthogonalen Polarisationskanälen unterschiedlich ist, kann das Prinzip der nichtlinearen geometrischen Phase zur Codierung von Multiplex-Hologrammen verwendet werden, die durch Umschalten des Polarisationszustands von Ko- auf Kreuzpolarisation von einem auf das andere Bild umschalten können.

Hier verwenden wir amorphes Silizium zur Realisierung der Metaoberflächen. Wie in dieser Arbeit gezeigt wurde, erfordert das nichtlineare geometrische Phasenprinzip jedoch eine zirkular polarisierte Grundanregung im Vergleich zu einer linear polarisierten Anregung im Fall von nichtlinearen Huygens-Metaoberflächen. Daher scheint amorphes Silizium im Zusammenhang mit der nichtlinearen PB-Phasenkontrolle aufgrund seiner isotropen Natur einen Nachteil zu haben, da THG aus einem isotropen Material unter zirkular polarisierter Anregung verboten ist. Es scheint, dass dem Mechanismus der Resonanzverstärkung besondere Aufmerksamkeit gewidmet werden muss. Aus diesem Grund war die nichtlineare Umwandlungseffizienz begrenzt und lag näher an dem, was man von plasmonischen Antennen erwartet: 10^{-18} 1/W^2 .

Aus dem Grund die Effizienz der nichtlinearen Konversion zu erhöhen, haben wir eine Metaoberflächen entwickelt, die Resonanzen unterstützt, die aufgrund ihrer Symmetrie vom Strahlungsspektrum entkoppelt sind: Quasi-bound states in the continuum (QBIC). Bound states in the continuum sind Resonanzen, die aufgrund ihrer Symmetrie vom Strahlungsspektrum entkoppelt sind. Bricht man diese Symmetrie, kann man vom freien Raum aus auf diese Mode zugreifen. Da QBIC-Resonanzen immer noch hohe Qualitätsfaktoren aufweisen, sind sie für die Erzeugung höherer Harmonischer von Vorteil. Es hat sich gezeigt, dass QBIC-Zustände die nichtlineare Umwandlungseffizienz auf bis zu 10^{-8} 1/W^2 erhöhen

können. Darüber hinaus wurden die Metaoberflächen so gestaltet, dass sie Mie-Resonanzen unterstützt, die ebenfalls die nichtlineare Effizienz auf 10^{-16} 1/W^2 bis 10^{-14} 1/W^2 erhöhen können. Wir zeigen numerisch und experimentell, dass eine Metaoberfläche aus amorphem Silizium mithilfe von Mie-Resonanzen und dem geometrischen Phasenprinzip effizient TH-Licht erzeugen und formen kann. Das Design erreicht Wirkungsgrade für die Umwandlung der dritten Harmonischen von 10^{-14} 1/W^2 , wenn es mit zirkular polarisiertem, fundamentalem Laserlicht in einem Wellenlängenbereich von 1240 bis 1360 nm beleuchtet wird. Die numerischen Studien zeigen, dass das Design QBIC unterstützt, um die nichtlineare Umwandlungseffizienz zu verbessern. Der Hauptgrund für die Dominanz der Mie-Resonanz ist der niedrige Qualitätsfaktor der BIC Mode, der auf unvermeidbaren Abweichungen im Nanofabrikationsprozess zurückzuführen ist, wie z. B. Oberflächenrauigkeit und Oberflächenzustände, die durch reaktives Ionenätzen entstehen. Daher kann es eine Herausforderung sein, eine QBIC-Resonanz in einem Experiment zu realisieren, da es leicht ist mit Moden mit sehr kleiner Linienbreite über- oder unterzukoppeln. Während des Designprozesses muss man Verbreiterungsmechanismen wie materialbedingte Verluste und Variationen der QBIC-Resonanzwellenlänge aufgrund der Standardabweichung in der Geometrie der einzelnen Nanoresonatoren berücksichtigen. Die Metaoberflächen bietet jedoch eine hohe Beugungseffizienz bei der Wellenlänge der dritten Harmonischen, basierend auf dem Prinzip der nichtlinearen geometrischen Phase. Außerdem kann das Prinzip der geometrischen Phase genutzt werden, um ein Vortex Beam Array in der dritten harmonischen mit hoher Genauigkeit zu kodieren. Da jedoch die Mie-Resonanz den Hauptbeitrag zum nichtlinearen Signal leistete, konnte die Frage, wie die geometrische Phase den QBIC-Zustand beeinflusst, nicht eindeutig untersucht werden.

Abstract

In this work, we have investigated the efficient nonlinear geometric phase response of amorphous silicon Metasurfaces. The Metasurfaces are fabricated from a thin amorphous silicon film by electron beam lithography and reactive ion etching. The geometric phase response and the nonlinear conversion efficiency were investigated using a Fourier spatial imaging setup, which allows us to map the spatial Fourier transform of the Metasurfaces, which can be used to understand the phase response of the Metasurfaces at the third harmonic wavelength. To investigate the phase response in the third harmonic generation, we coded a phase profile similar to a blazed grating and a multiplexed hologram to demonstrate the feasibility of this approach. In summary, the geometric phase can be integrated into the nonlinear third-harmonic generation process and can be used to direct and shape the generated light.

Furthermore, we expect different geometric phase responses depending on the rotational symmetry. In the case of C_1 or C_2 rotational symmetry, the geometric phase is proportional to two times the rotation angle and four times the rotation angle for cross-polarization. Since the geometric phase is different in two orthogonal polarization channels, the principle of the nonlinear geometric phase can be used to encode multiplexed holograms, which can be switched from co- to cross-polarization by switching the polarization state. Here we use amorphous silicon to realize the Metasurfaces. However, as shown in this work, the nonlinear PB phase principle requires circularly polarized fundamental excitation compared to linearly polarized excitation in the case of nonlinear Huygens Metasurfaces. Therefore, amorphous silicon seems to have a disadvantage in the context of nonlinear PB phase control due to its isotropic nature since THG from an isotropic material is forbidden under circularly polarized excitation. It seems that special attention must be paid to the mechanism of resonance enhancement. For this reason, the nonlinear conversion efficiency was limited and closer to what is expected from plasmonic antennas: 10^{-18} 1/W^2 .

To increase nonlinear conversion efficiency, we have developed a Metasurface that supports resonances decoupled from the radiation spectrum due to their symmetry: Quasi-bound states in the continuum (QBIC). Bound states in the continuum are resonances that are decoupled from the radiation spectrum due to their symmetry. If one breaks this symmetry, one can access the mode from free space. Since QBIC resonances still offer high quality factors, they are advantageous for generating higher harmonics. It has been shown that QBIC states can increase the nonlinear conversion efficiency up to 10^{-8} 1/W^2 . In addition, the Metasurface was designed to support Mie resonances, which can also increase nonlinear efficiency up to 10^{-16} 1/W^2 to 10^{-14} 1/W^2 . We show numerically and experimentally that an amorphous silicon Metasurface can efficiently generate and shape TH light using Mie resonances. The design achieves third-harmonic conversion efficiencies as high as 10^{-14} 1/W^2 when illuminated with circularly polarized fundamental laser light in a wavelength range from 1240 to 1360 nm. The

numerical studies show that the design supports QBIC to improve the nonlinear conversion efficiency. The main reason for the dominance of the Mie resonance is the low quality factor of BIC, which is due to inaccuracies in the nanofabrication process, such as surface roughness and surface states formed by reactive ion etching. Therefore, it can be challenging to implement a QBIC resonance in an experiment because it can easily over-or under-couple with modes with a very small linewidth. During the design process, one must keep in mind and account for broadening mechanisms such as material-related losses and variations in the QBIC resonant wavelength due to the variance in the geometry of the individual nanoresonators in the Metasurface. However, the Metasurface provides high diffraction efficiency at the third harmonic wavelength based on the principle of the nonlinear geometric phase. Moreover, the principle of geometric phase can be used to encode a vortex beam array in the nonlinear generation process with high fidelity. However, since the Mie resonance was the main contributor to the nonlinear signal, the question of how the geometric phase affects the QBIC state could not be clearly investigated.

Table of Contents

Chapter 1 Introduction	4
Chapter 2 Scattering of light: From natural effect to nonlinear engineering	8
2.1 The flow of electromagnetic energy and the optical theorem.....	10
2.2 Mie resonances.....	13
2.3 The “material side” of optical scattering and the optical properties of amorphous silicon ...	21
2.4 Nonlinear Optics	24
2.5 The third-order response of amorphous silicon	26
2.6 The nonlinear conversion efficiency.....	29
2.7 Third harmonic generation from a nano cylinder	33
Chapter 3 Enabling nonlinear optical engineering: Fabrication technology	38
3.1 Plasma Enhanced Deposition of amorphous silicon.....	39
3.2 Resist Spin-Coating	39
3.3 Electron beam lithography (EBL) and development.....	40
3.4 Etch mask deposition and lift-off.....	44
3.5 Reactive ion etching and Cr removal.....	44
Chapter 4 The propagation of light and nonlinear beam shaping with dielectric metasurfaces.....	47
4.1 Resonant wavefront shaping: The Huygens Principle	49
4.2 Geometric Phase Principle.....	52
4.3 Derivation of the PB phase for THG.....	53
4.4 Gradient design.....	57
4.5 The geometry of the unit cell and optical characterization	58
4.6 Nonlinear optical characterization by Fourier plane imaging	60
4.7 Nonlinear measurements	62
4.8 Power dependence of the third harmonic signal and conversion efficiency.....	65
4.9 Holography and the Gerchberg Saxton Algorithm	67
4.10 Nonlinear Metasurface Holography	71
4.11 Nonlinear generation and geometric phase in view of rotational symmetries	73
4.12 Geometric Phase for C_2 Rotational Symmetry	76
4.13 Additional discussion about coupling effects in C_2 symmetry.....	80
4.14 C_1 rotational symmetry.....	83
4.15 Experimental verification for C_1	84
4.16 C_4 Rotational Symmetry	85

4.17 Experimental Results C_4	86
4.18 Conclusion	87
Chapter 5 Third harmonic generation and phase control with quasi-BIC and Mie resonances	90
5.1 Symmetry protected BIC in cylindrical nanostructures and quasi-BIC	94
5.2 Nonlinear geometric Phase of QBIC	97
5.3 Experimental Results	99
5.4 Linear Transmission	99
5.5 Nonlinear Measurement Setup	100
5.6 Nonlinear Measurements	102
5.7 Coupled Harmonic Oscillator Model	103
5.8 Model Results	106
5.9 Influence of fabrication tolerances	111
5.10 Diffraction Efficiency	114
5.11 Experimental Results	116
5.12 Vortex Beam Array	118
5.13 Conclusion	121
Chapter 6 Outlook	122
Chapter 7 References	125
Chapter 8 Appendix	136
8.1 Journal Publication during PhD	136
8.2 Conference Presentations	136
8.3 Other Contributions	137
Chapter 9 Acknowledgements	138

Chapter 1 Introduction

Sixty years ago, Franken et al. first demonstrated second-harmonic generation from a beta barium oxide crystal, and Bloembergen et al. theoretically investigated wave mixing. [1, 2] These discoveries established the field of nonlinear optics, and the contributions of various researchers around the world discovered nonlinear optical phenomena that led to a vast space of possible applications in the control and generation of light that would not have been possible otherwise: Harmonic and supercontinuum generation, Raman scattering, entangled photon and ultrashort pulse generation and measurements, to name a few. [3, 4] All these ideas have a common theme: Controlling or measuring light with light, and this theme is a promising route to realizing various new technologies. For example, optical computing is about controlling light with light: An essential logical operation for realizing optical (quantum) computing is the Controlled Not (CNOT) gate. [4] The CNOT gate operates on two quantum bits and inverts the first quantum Bit if and only if the other quantum Bit is set to $|1\rangle$. In optics, this process requires an interaction between two photons, which can be realized with nonlinear optical effects. Even though the idea of an optical computer is far-fetched and not yet feasible, first steps have been taken toward optical (quantum) computing. First, companies like Intel integrate photonic waveguides directly in their chips to reduce the latency of optical fiber communication between computers. [5] Even more interestingly, Feldmann et al. have realized an integrated optical waveguide network for processing matrix operations, which is a promising way to accelerate computations in areas such as computer vision. [6] Unfortunately, the nonlinear interaction between photons needed for optical computation is weak and requires strong fields and long interaction times in materials with strong nonlinear coefficients. Thus, nonlinear optical effects were discovered after the invention of the Laser in 1960 by Maiman.

Researchers have historically used thick, specially cut optical crystals and resonators to prolong the interaction of light with nonlinear optical materials to improve the nonlinear conversion efficiency and light-light or light-matter interaction. [3, 7] This approach results in bulky optical devices. However, for devices that require many nonlinear elements like a network, the size of the nonlinear optical elements must shrink, and due to the small size of the required optical elements, we face some restrictions: First, the smaller size of the optical elements has an impact on the efficiency of the nonlinear conversion process. Second, a single nonlinear optical element must perform more than one function, as the elements should be compact. One technology that helps us solve these limitations are resonant nanoparticles and Metasurfaces. Metasurfaces are arrays of resonant nanoparticles which can be arbitrarily shaped by nanofabrication, and therefore, they can be used to encode a wide range of functionalities. Because of their flexibility, metasurfaces are fascinating to realize functional nonlinear optical devices, which we investigate in view of its restrictions. We use amorphous silicon metasurfaces to enhance and, at the same time, shape light in the third harmonic

generation process. The goal of this work is to investigate how to enhance the nonlinear interaction between three photons and manipulate the propagation of the generated light to realize various functions.

There are several aspects to this goal. First, how to manipulate light propagation at the third harmonic frequency, second, how to improve third harmonic generation by using specific resonances of the metasurface/nanoresonators, and third, how to find a good compromise between resonance enhancement and propagation manipulation. On the first point, to manipulate the propagation of light at the third harmonic frequency, we use the geometric phase principle. This principle uses the rotation of a single nanoparticle in an array to manipulate the phase of light at triple frequency. This principle was first introduced for plasmonic systems and allows light to be directed and manipulated to realize essential functions such as beam steering [8], focusing, [9] multiplexed holography, [10, 11], and nonlinear optical chirality. [12] However, the nonlinear conversion efficiency of these processes in plasmonic systems is limited because the localized surface plasmon resonance (LSPR), which is the fundamental functional mechanism of plasmonic resonances, has some limitations. Ohmic losses, low quality factors of LSPR, and low contribution of nonlinear coefficients in the bulk material due to the skin effect in metals limit the nonlinear conversion efficiency [13, 14]. To increase the nonlinear conversion efficiency, researchers have used dielectric nanoparticles that support Mie resonances when the size of the particles becomes comparable to the size of the wavelength. However, the advantage of higher conversion efficiency comes with a disadvantage: dielectric nanoparticles have a larger three-dimensional extent than their plasmonic counterpart. [14, 15] For this reason, dielectric metasurfaces require a higher density of resonators for reliable phase control compared to plasmonic metasurfaces. In addition, the size of the dielectric resonators is similar to the wavelength of the second and third harmonics of the generated light at visible frequencies. Therefore, near-field coupling between resonators and diffraction effects are not as negligible as in the case of plasmonics, and the phase-matching and the direction of the generated light required for nonlinear wavefront control becomes a complex task. Wang et al. and Gao et al. demonstrated the wavefront control of the third-harmonic light generated by fully dielectric silicon metasurfaces. [16, 17] Their approach is based on the generalized Huygens principle of nonlinear optics. By exploiting the (Mie) resonance behavior of a single silicon nanoresonator, they designed a library of individual structures that lead to different phase delays for the locally generated third harmonic signal. However, to smoothly cover the entire phase range of $0-2\pi$, many structures must be designed. Such a design is a computationally intensive task because a single nanoresonator has multiple geometric degrees of freedom, and the optical properties must be tuned for the nonlinear process with the desired phase and amplitude. Therefore, the Huygens method of nonlinear phase control is sensitive to the precise geometry and refractive index of the nanostructures, complicating fabrication and making the optical properties susceptible to fabrication tolerances. In contrast, geometric phase principles can be used to continuously adjust the phase of the generated light. The significant

advantage of the geometric phase principle is that one only needs to design and optimize a single resonator geometry and can rotate the structures on a metasurface to match a desired nonlinear phase profile. However, the disadvantage of this approach concerning dielectric metasurfaces is that the crosstalk and near-field coupling between the nanostructures varies from unit cell to unit cell due to the rotation and may affect the phase of the generated light since nonlinear optical effects are susceptible to small changes. Another challenge is that the geometric phase principle requires circularly polarized light, but third-harmonic generation under circularly polarized light is prohibited in amorphous silicon, which is used as the material in this work. Therefore, it is necessary not only to take care of the (Mie) resonance to enhance the nonlinear third-harmonic generation but also to design the nanoresonator in view of nonlinear selection rules, crosstalk between the structures, and directionality of light.

On the other hand, concerning nonlinear optical conversion efficiency, two resonance mechanisms are of interest: magnetic Mie resonances [14, 18, 19] and so-called quasi-bound states in the continuum (QBIC) because it has been shown that both can amplify nonlinear effects. [14, 20] Therefore, it is interesting to study both resonances in terms of their capabilities for nonlinear phase manipulation. Compared to Mie resonance, QBIC resonances can provide much higher conversion efficiencies, almost reaching the efficiency of conventional nonlinear crystals (see Table 2. Comparison of the different nonlinear optical elements for THG. The values are taken from the publications and the table is recreated and extended from Ref [13]. The entry for the BBO crystal was calculated based on information provided by the manufacturer (EKSMA): Ti:Sa Super Spitfire Laser operating at 1 kHz, 130 fs pulse width, 100 μ J pulse energy at 800 nm, beam diameter 1 mm.). Further, Quasi-BIC resonances are derived from BIC modes, which are decoupled from the radiation spectrum. [21] A mode can be decoupled from the radiation spectrum through symmetry and the collective in-phase oscillation of many resonators. BIC has been shown to exist in many dielectric metasurfaces, for example, arrays of nanocylinders. These modes have exceptionally high quality factors ($Q > 10,000$) compared to Mie resonances ($Q \sim 50$) [14] and therefore provide a strong enhancement of nonlinear optical effects. However, since these modes are decoupled from the radiation spectrum, the coupling of light to these modes is complicated, and one must introduce asymmetry to match the symmetry of the modes to the symmetry of a plane wave. [22] This asymmetric design leads to QBIC resonances with high quality factors, which can be used to improve nonlinear conversion processes. For example, BIC exists in arrays of nanocylinders, but a nanocylinder is rotationally invariant. To convert the BIC mode into a QBIC resonance, one can introduce a small off-center hole. Therefore, an asymmetry makes a BIC mode accessible from free space and offers the possibility of introducing a geometric phase into the third harmonic generation process. [20] However, this advantage raises a question. The collective oscillation of resonators often plays a crucial role in forming symmetry-protected BIC modes and QBIC resonances. In contrast, the geometric phase will spatially change the phase of the oscillating nanoresonators that form the QBIC resonance, and it is worth investigating how the QBIC resonance behaves when a geometric phase is

introduced into the metasurface. Therefore, another part of this work is to study the geometric phase in dielectric resonators and the geometric phase in terms of Mie and QBIC resonances, which can be used to improve nonlinear processes.

Chapter 2 Scattering of light: From natural effect to nonlinear engineering

The scattering of light by small objects is one of the classical problems in optics, and it is responsible for many phenomena in nature, from the blue sky we see every day to the white appearance of clouds or smoke. [23] However, the interaction of light and matter is a complicated problem that generally depends on the shape of the scatterer and its material properties. It is convenient to distinguish between different domains to find meaningful explanations for the different effects resulting from scattering. In general, light scattering at spherical objects can be divided into two domains based on the diameter of the scatterer D versus the incident wavelength λ . When the particle is small compared to the wavelength, Rayleigh scattering dominates, which describes the process as an elastic scattering of an electromagnetic wave by a small scatterer, such as a molecule, as illustrated in Figure 1. [23–26] This effect causes, for example, the blue color of the sky during the day when molecules scatter sunlight in the Earth's atmosphere. Since the process itself is inversely proportional to the fourth power of the wavelength, shorter wavelengths are scattered stronger than the longer ones [23]. Therefore, the blue light is distributed throughout the sky, while the sun's red light is less affected. When the particles have a size comparable to the incident wavelength, Mie theory is used to describe the interaction of light and matter. Gustav Mie first derived Mie theory in 1908 to describe the color and optical behavior of colloidal gold particles in which the gold nanoparticles resonate with visible light. [26] In general, Mie scattering results in more uniform scattering, where the scattering does not depend strongly on wavelength and light of all colors/wavelength is scattered uniformly in all directions, as shown in Figure 1a. This effect is responsible for the white appearance of clouds or smoke, where all colors of sunlight are scattered evenly in all directions. In addition to explaining natural phenomena, Mie theory offers a variety of technical applications: in the industry for measuring the size of small particles below 50 μm [27] or in medicine for distinguishing and counting plasma proteins in blood samples [28]. However, the advent of modern nanotechnology has allowed researchers to control the shape and arrangement of scatterers at will, as sketched in Figure 1b. These so-called metasurfaces are a new application of scattering theory. Here, each scatterer's resonances, geometry, and spatial arrangements are designed numerically to achieve specific functions [29]. One example is the development of flat metalenses in which a spatial arrangement of nanoscaters focuses the light. [30] Moreover, by engineering the Mie resonances of nanoparticles, we can shape the interaction of light and matter and enhance physical effects that are inherently weak, such as nonlinear optical phenomena as third-harmonic generation, as explained later.

This chapter describes the basic concepts used to describe the interaction of light and matter in the linear regime in terms of Mie resonances as well as in the nonlinear regime. First, we introduce the concept of scattering and Mie resonances in nanostructures by outlining the

derivation of the Mie solution from the Helmholtz equation leading to magnetic or electric multipole resonances. Later, I will introduce the "material side" of the scattering problem and discuss the optical properties of amorphous silicon, the material we have chosen for this work, and its nonlinear response.

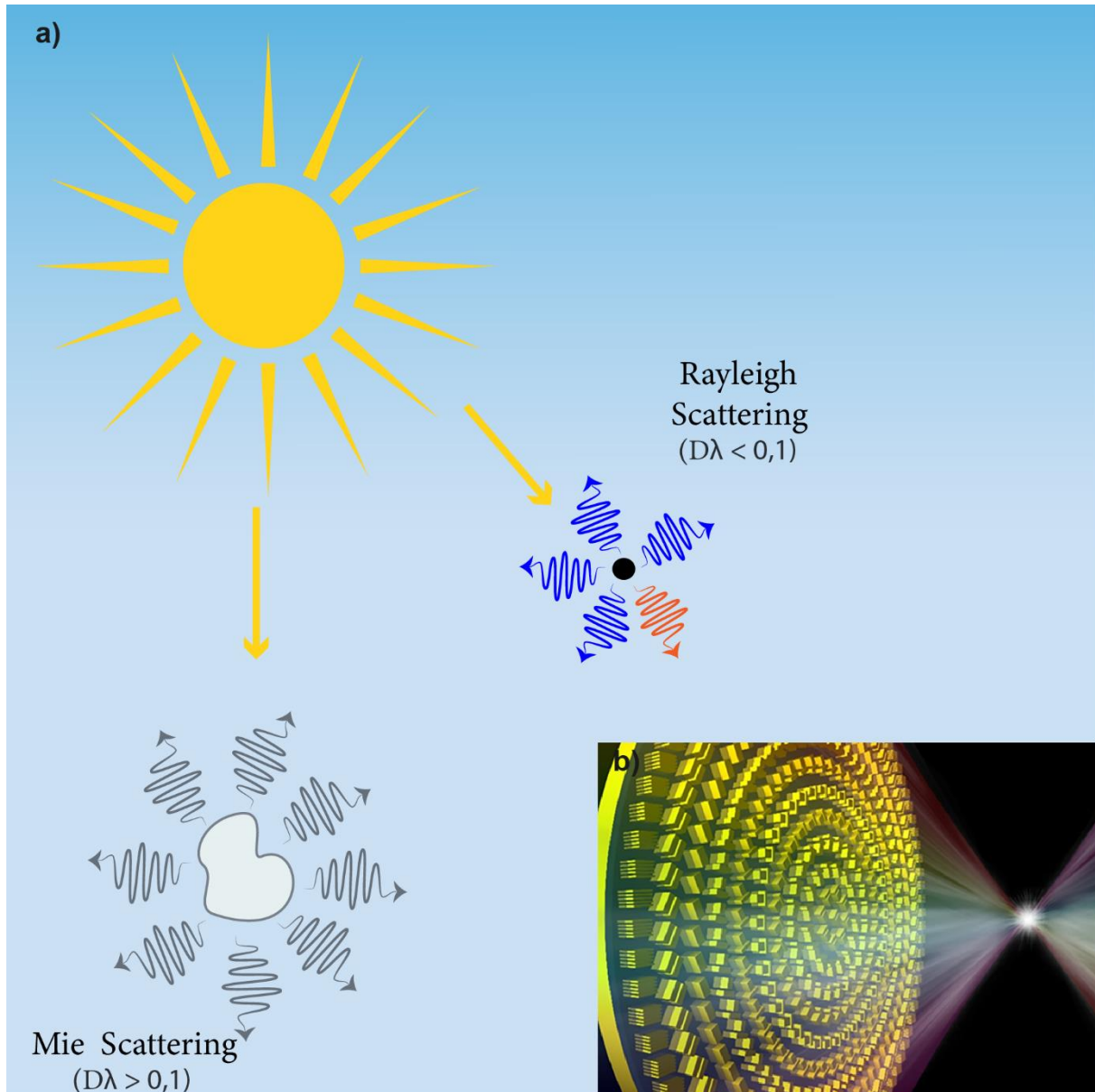


Figure 1. a) Illustration of Rayleigh and Mie scattering Sunlight is scattered by particles in the atmosphere. Depending on the size of the particles, Rayleigh or Mies scattering dominates. For small molecules, whose size is much smaller than the wavelength of the light, Rayleigh scattering predominates. Here, blue light is strongly scattered in all directions, while red light is less scattered. For larger particles, such as dust or small water droplets, which are comparable to the wavelength of light, Mie scattering predominates. Here, the light is

scattered uniformly in all directions. b) Illustration of a lens which utilizes Mie scattering to focus light. Taken from Ref. [30]

2.1 The flow of electromagnetic energy and the optical theorem

A scattering experiment is sketched in Figure 2. An external field described by $[E_{inc}, H_{inc}]$ is incident on an object in a homogeneous medium. A part of the energy of the incident field is transferred to the object. At the object, the energy is either dissipated through (thermal) losses or scattered away. Therefore, the total electromagnetic field can be decomposed into the background field $[E_b, H_b]$ and the scattered field $[E_s, H_s]$. The background field describes the propagation of the incident field without the presence of the scatterer, and the scattered field describes the field radiated by the nano-object due to excitation by $[E_b, H_b]$. The electromagnetic scattering problem between the incident light and the particle can be complicated and is generally solved only numerically.

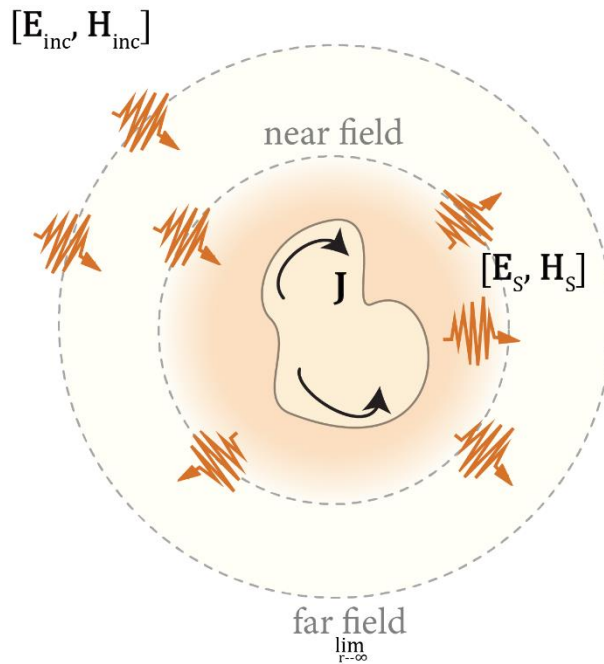


Figure 2. Light scattering by a nano-object. An external wave $[E_{inc}, H_{inc}]$ falls on a nanostructure and induces a current J in its volume. The scattered field $[E_s, H_s]$ is radiated into the far-field and superimposes with the incident field. Recreated from Ref. [31].

However, it is possible to derive some basic principles of scattering since a scattering process is subject to the law of conservation of energy, i.e., the total electromagnetic energy in a volume Ω with its corresponding interface Σ around a scatterer must be conserved. In

electromagnetics, the law of conservation of energy is called the Poynting theorem and is a scalar equation [32]:

$$-\frac{1}{2} \int_{\Omega} \vec{J}^* \cdot \vec{E} dr = 2i\omega \int_{\Omega} W dr + \oint_{\Sigma} \vec{S} \cdot \vec{n} d\sigma \quad 1$$

Where S is defined as the Poynting vector and W is the electromagnetic energy density in the volume:

$$\vec{S} = \frac{1}{2} \vec{E} \times \vec{H}^* \quad 2$$

$$W = \frac{1}{4} (\vec{E} \cdot \vec{D}^* + \vec{B} \cdot \vec{H}^*) \quad 3$$

\vec{J} is the induced current density in the scatterer due to the electromagnetic field. Also, E is the electric field, D is the electric displacement vector, B is the magnetic field vector, and H is the magnetizing field. The first term on the left-hand side of the equation 1 represents the interaction of the electromagnetic field with the scatterer and the dissipation of the electromagnetic energy into heat. In contrast, the second term on the right-hand side in equation 1 represents the total electromagnetic energy in the volume Ω . The last term on the right-hand side in equation 1 describes the electromagnetic energy flow into a given volume, flowing through the surfaces Σ of the volume, as shown in Figure 2. Furthermore, as outlined in the beginning, the electromagnetic field can be decomposed into its various contributions from the incident and scattered field and the absorbed energy. Therefore, the Poynting vector can be decomposed into the contributions from the incident field (\vec{S}_{inc}), the scattered field (\vec{S}_s) and the extinction (\vec{S}_{ext}) [32]:

$$\vec{S} = \vec{S}_{inc} + \vec{S}_s + \vec{S}_{ext} \quad 4$$

Where the \vec{S}_{inc} , \vec{S}_s and \vec{S}_{ext} are defined as follows:

$$\vec{S}_{inc} = \frac{1}{2} \vec{E}_b \times \vec{H}_b^*$$

5

$$\vec{S}_s = \frac{1}{2} \vec{E}_s \times \vec{H}_s^*$$

6

$$\vec{S}_{ext} = \frac{1}{2} (\vec{E}_b \times \vec{H}_s^* + \vec{E}_s \times \vec{H}_b^*)$$

7

By taking advantage of the above-defined Poynting vectors, the time average of the Poynting theorem can be written as follow:

$$W_{abs} + W_{sca} = W_{inc} + W_{ext}$$

8

Where the W terms are defined as:

$$W_{abs} = \int_{\Omega} Re(\vec{J}^* \cdot \vec{E}) d\vec{r}$$

9

$$W_{sca} = \oint_{\Sigma} \langle \vec{S}_{sca} \rangle \cdot \vec{n} d\sigma$$

10

$$W_{inc} = \oint_{\Sigma} \langle \vec{S}_{inc} \rangle \cdot \vec{n} d\sigma = 0$$

11

$$W_{ext} = \oint_{\Sigma} \langle \vec{S}_{ext} \rangle \cdot \vec{n} d\sigma$$

12

The terms correspond to the average powers of the electromagnetic field which are incident (W_{inc}), scattered away (W_{sca}), or dissipated (W_{abs}) on the particle. The extinction power W_{ext} can be interpreted as the total power that interacts with the nano-object, which may result in scattering or dissipation of energy: $W_{ext} = W_{abs} + W_{sca}$. This interpretation of W_{ext} follows from the fact that the incident electromagnetic field W_{inc} has an average power of 0. W_{inc} is zero, because W_{inc} represents the energy of the background field, that does not interact with the particle. This energy enters and leaves the volume in Figure 2. In addition, if the object is

excited by a plane wave, W_{ext} can be normalized to its intensity $I = \frac{1}{2} \sqrt{\frac{\epsilon_0}{\mu_0}} E_0^2$, which leads to the concept of the extinction cross-section: $\sigma_{ext} = \frac{W_{ext}}{I}$. As the extinction power is the sum of the scattered and dissipated power, the extinction cross-section can be written as the sum of the scattering cross-section $\sigma_{sca} = \frac{W_{sca}}{I}$ and the absorption cross-section $\sigma_{abs} = \frac{W_{abs}}{I}$:

$$\sigma_{ext} = \sigma_{abs} + \sigma_{sca}$$

13

Here, the cross-section is given in the unit of inverse square meter (m^2). Often the cross-section is normalized to the area of the object (in the direction of propagation of the wave), which is called the effective extinction cross-section. The effective extinction cross-section measures how large the object appears to a wave with a wavelength of λ . Typical values for the effective extinction cross section are between 1 and 10, i.e. an object can appear as large as the wavelength of the light or even larger if the incident wave is in resonance with the object. Note that experimentally, instead of the scattering cross section, the transmission is often evaluated because it is easier to measure and, in the context of resonant dielectric metasurfaces, it also provides similar information about the operation of the metasurfaces. For transmission one evaluates the energy W_T that a particle or an array of particles scatters in the forward direction and compares it with the incident energy W_{inc} in the same direction, so that $T = \frac{W_T}{W_{inc}}$. Compared to the effective scattering cross-section, the transmission is less than one.

However, considering only the conservation of energy, the extinction cross-section can be related to the incident and the scattered field with the same direction, i.e., with the same wave vector \vec{k}_0 .

$$\sigma_{ext} = \frac{4\pi}{kE_0^2} \text{Im} \left(\vec{E}_0^* \cdot \vec{E}_s(\vec{k}_0) \right)$$

14

The above relationship is called the optical theorem and states that the power transmitted to a scattering object depends only on the scattered field in the same direction as the incident electromagnetic wave. If an object does not scatter light in a particular direction, it cannot be excited from that direction.

2.2 Mie resonances

The optical theorem provides a way to understand scattering in terms of energy flow. However, it does not provide a detailed picture of the interaction of light with a particle whose size corresponds to the wavelength. Here, Mie theory provides a compelling picture to

understand the electromagnetic response of a nanoparticle in terms of radiating electric and magnetic multipoles, and it provides a lot of intuition to explain the scattering of an arbitrarily shaped particle in terms of its multipole resonances [25]. Although, only the scattering problem of a nanosphere with refractive index n_1 in a uniform medium with refractive index n_0 can be solved analytically. However, more complex geometries must be evaluated numerically. The eigenmodes of this system are called vector spherical wave functions (VSWF) and can be derived in spherical coordinates from the Helmholtz equation. The derivation of Mie scattering is complicated and would fill a separate chapter and can be found in Ref. [23] and [26]. Here the derivation and its most essential parts are outlined. The goal is to find the scattered electromagnetic fields $[E_s, H_s]$ outside of the sphere and internal (near) electromagnetic fields $[E_i, H_i]$ inside the sphere in terms of the VSWF. To derive the scattering of a spherical particle in a dielectric sphere, consider the scalar Helmholtz equation for the electric and magnetic field [23]:

$$\Delta \vec{E}(\vec{r}, \omega) + k^2 \vec{E}(\vec{r}, \omega) = 0 \quad 15$$

$$\Delta \vec{H}(\vec{r}, \omega) + k^2 \vec{H}(\vec{r}, \omega) = 0 \quad 16$$

Further, the solution for the electric and magnetic fields of the Helmholtz equation needs to satisfy the following conditions:

$$\nabla \cdot \vec{E} = \nabla \cdot \vec{H} = 0 \quad 17$$

$$\nabla \times \vec{E} = i\omega\mu\vec{H} \quad 18$$

$$\nabla \times \vec{H} = i\omega\mu\vec{E} \quad 19$$

reflecting the time-harmonic Maxwell equations, where the time dependence is given by $e^{i\omega t}$ without free electric charges $\rho = 0$ and currents ($\vec{j} = 0$). These conditions mathematically mirror the scattering scenario outlined in the last chapter.

A solution of the Helmholtz equation which satisfy the conditions 17 to 19 is given by:

$$\vec{M}_{mn}^{e/o} = \nabla \times (\vec{r} \psi_{mn}^{e/o}) \quad 20$$

$$\vec{N}_{mn}^{e/o} = \frac{1}{k} \nabla \times \vec{M}_{mn}^{e/o}$$

21

where $\vec{M}_{mn}^{e/o}$ denotes the vectorial magnetic field harmonics (TM) and $\vec{N}_{mn}^{e/o}$ the vectorial electric harmonics (TE). Therefore, the scattered electromagnetic fields $[E_s, H_s]$ and internal electromagnetic fields $[E_i, H_i]$ are given as an expansion series of the VSWF. The function $\psi_{mn}^{e/o}$ in equation 20 and 21 denotes the even (e) and odd (o) scalar spherical harmonics which generate the vector spherical harmonics:

$$\psi_{mn}^o = \sin(m\phi) P_n^m(\cos(\theta)) z_n(kr)$$

22

$$\psi_{mn}^e = \cos(m\phi) P_n^m(\cos(\theta)) z_n(kr)$$

23

Where $P_l^m(\cos(\theta))$ are the associated Legendre polynomials:

$$P_l^m(\cos(\theta)) = \sum_{k=0}^{\frac{n}{2}} (-1)^m (-1)^k (\sin(\theta))^m \frac{d^m}{d(\cos(\theta))^m} P_l(\cos(\theta))$$

24

with P_l are the Legendre Polynoms with $P_l = \frac{1}{2^n n!} \frac{d^n}{dx^n} ((x^2 - 1)^n)$.

$z_n(kr)$ denotes the radial part of the scalar spherical harmonics. In this case, the function $z_n(kr)$ may be given by a spherical Bessel, or Hankel function, depending on the boundary conditions which are imposed on the interfaces between the internal and external electromagnetic fields. An overview of the magnetic, electric spherical harmonics, and scalar spherical harmonics is given in Figure 3. Note that the magnetic, electric spherical harmonics are vectorial functions, and each point has an absolute value and a direction.

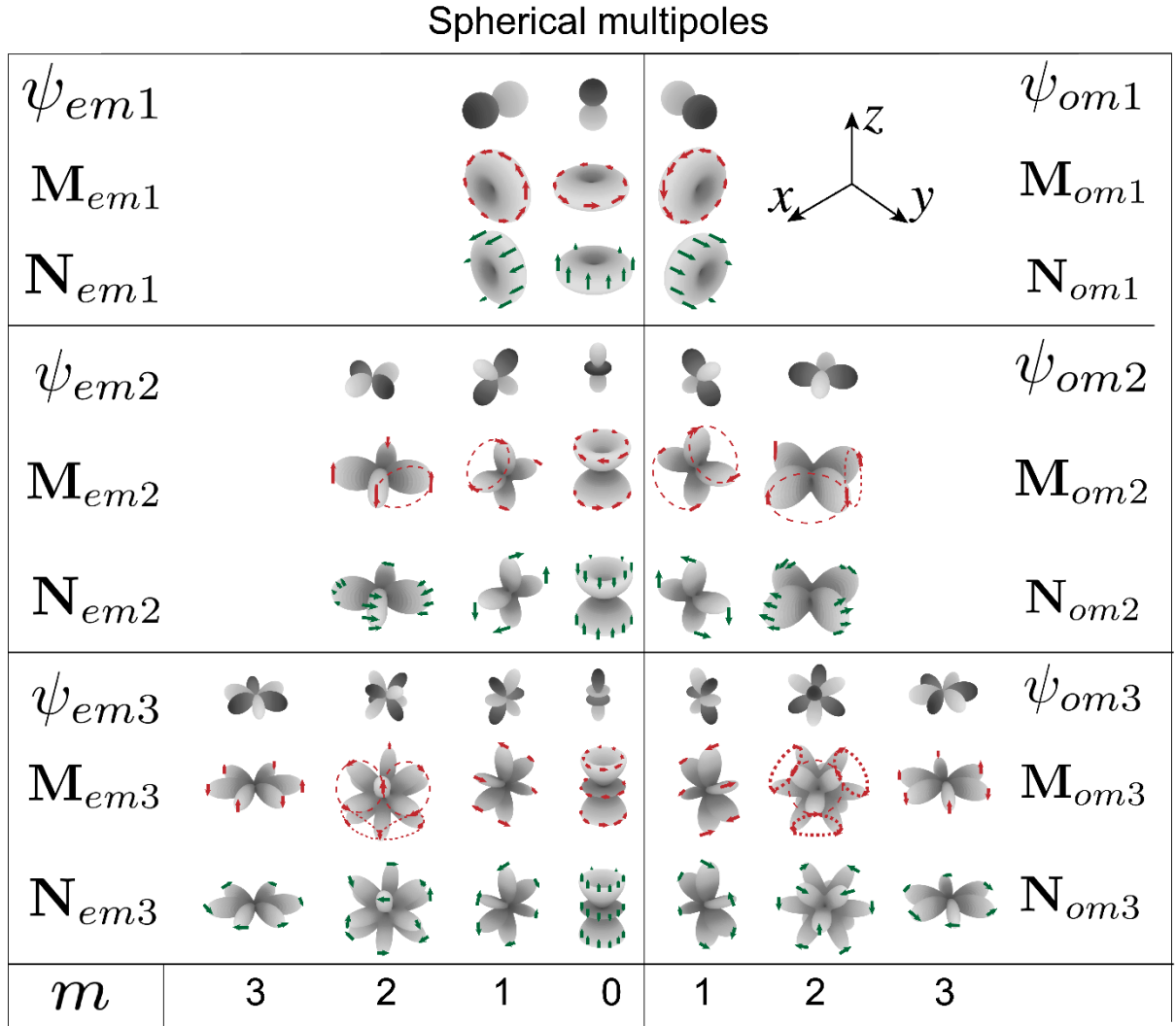


Figure 3. The angular part of the spherical harmonics of the magnetic and electric vector. Red and green arrows indicate the direction of the field. The figure also shows the generating scalar functions, where only the first three orders (dipoles, quadrupoles, octupoles) are shown [33].

The VSWF are the solution of the Helmholtz equation for the scattering problem of a plane wave and a sphere, but one needs to determine how strong each vector spherical harmonic contributes to a scattering process. Therefore, one needs to connect the incident plane wave with the scattered electromagnetic field $[E_S, H_S]$ and the internal field $[E_i, H_i]$ of the sphere, this is done in two steps: First, the incident plane wave is expanded in terms of the VSWF and in a second step one needs to determine the radial part $z_n(kr)$ of the scattered fields $[E_S, H_S]$ and internal fields $[E_i, H_i]$ of the sphere.

The first step is expanding the incident plane wave $E(r) = E_0 e^{i\vec{k}\vec{r}}$ into the basis of the VSWF:

$$\vec{E}_{inc} = \vec{E}_0 e^{i\vec{k}\vec{r}} = E_0 \sum_{n=1}^{\infty} \frac{i^n (2n+1)}{n(n+1)} \left(\vec{M}_{mn}^o(k, \vec{r}) - i\vec{N}_{mn}^e(k, \vec{r}) \right)$$

$$\vec{H}_{inc} = -\frac{k}{\omega\mu} E_0 \sum_{n=1}^{\infty} \frac{i^n (2n+1)}{n(n+1)} \left(\vec{M}_{mn}^e(k, \vec{r}) - i\vec{N}_{mn}^o(k, \vec{r}) \right)$$

25

The second step is to impose the following interface conditions on the electromagnetic fields which determine the radial part $z_n(kr)$ of the magnetic and electric spherical harmonics $\vec{N}_{mn}^{e/o}$ and $\vec{M}_{mn}^{e/o}$ of the scattered fields $[E_s, H_s]$ and internal fields $[E_i, H_i]$: Let us first consider the interface conditions at the boundary between the sphere and its surrounding environment. Since the sphere and the surrounding media are assumed to be perfect dielectrics, there are neither charges nor surface currents at the interface, so that the tangential component of \vec{H} and the normal component of \vec{D} are both continuous. The second interface condition is that the solution is bounded at the origin. Therefore, the radial part $z_n(kr)$ of the functions $\psi_{mn}^{e/o}$ of the internal field $[E_i, H_i]$ is given in terms of Bessel spherical functions. Third, the asymptote at infinity corresponds to a diverging spherical wave for the scattered field. Therefore, the radial part $z_n(kr)$ of $\psi_{mn}^{e/o}$ of the scattered electromagnetic field $[E_s, H_s]$ is given by spherical Hankel functions of the first kind. In total the scattered and internal fields are given by

$$\vec{E}_s = \sum_{n=1}^{\infty} E_n \left(ia_{mn} \vec{N}_{mn}^e(k, \vec{r}) - b_{mn} \vec{M}_{mn}^o(k, \vec{r}) \right)$$

$$\vec{H}_s = -\frac{k_1}{\omega\mu_1} \sum_{n=1}^{\infty} E_n \left(ia_{mn} \vec{N}_{mn}^e(k, \vec{r}) - b_{mn} \vec{M}_{mn}^o(k, \vec{r}) \right)$$

26

$$\vec{E}_i = \sum_{n=1}^{\infty} E_n \left(-id \vec{N}_{mn}^e(k_1, \vec{r}) + c_{mn} \vec{M}_{mn}^o(k_1, \vec{r}) \right)$$

$$\vec{H}_i = -\frac{k_1}{\omega\mu_1} \sum_{n=1}^{\infty} E_n \left(ic_{mn} \vec{N}_{mn}^o(k_1, \vec{r}) - d_{mn} \vec{M}_{mn}^e(k_1, \vec{r}) \right)$$

27

With $k = \frac{\omega}{c} n$ as the wave vector outside the particle and $k_1 = \frac{\omega}{c} n_1$ as the wave vector in the medium of the nanoparticle. E_n is the amplitude of the electromagnetic field.

The coefficients a_{mn} , b_{mn} , c_{mn} and d_{mn} determine the contribution of each VSWF and each coefficient results from the overlap integrals of the incident plane wave (equation 25), the scattered (equation 26) and the internal fields (equation 27) of the form:

$$\frac{\int_0^{2\pi} \int_0^\pi \vec{E}_{inc/i/sca} \vec{M}_{mn}^{e/o} \sin(\theta) d\theta d\phi}{\int_0^{2\pi} \int_0^\pi |\vec{M}_{mn}^{e/o}|^2 \sin(\theta) d\theta d\phi}$$

28

By substituting the expressions for the electromagnetic fields into equation 28, the coefficients a_{mn} , b_{mn} , c_{mn} , d_{mn} can be written as follows:

$$\begin{aligned} c_{nm} &= \frac{\mu_1[kah_n(ka)]'j_n(ka) - \mu_1[kaj_n(ka)]'h_n(ka)}{\mu_1[kah_n(ka)]'j_n(ka) - \mu[k_1aj_n(k_1a)]'h_n(ka)} \\ d_{nm} &= \frac{\mu_1n_1n[kah_n(ka)]'j_n(ka) - \mu_1n_1n[kaj_n(ka)]'h_n(ka)}{\mu n_1^2[kah_n(ka)]'j_n(k_1a) - \mu_1n^2[k_1aj_n(k_1a)]'h_n(ka)} \\ b_{nm} &= \frac{\mu_1[kaj_n(ka)]'j_n(k_1a) - \mu[k_1aj_n(k_1a)]'j_n(ka)}{\mu_1[kah_n(ka)]' - \mu[k_1aj_n(k_1a)]'h_n(ka)} \\ a_{nm} &= \frac{\mu n_1^2[kaj_n(ka)]j_n(k_1a) - \mu_1n_1^2[k_1aj_1(k_1a)]'j_n(ka)}{\mu n_1^2[kah_n(ka)]'j_n(k_1a) - \mu_1n_n^2[k_1aj_n(k_1a)]'h(ka)} \end{aligned}$$

29

Here, a is the radius of the sphere and j_n and h_n denote the spherical Bessel and Hankel functions of the first kind, respectively. As explained above, these functions result from the radial part of the generating function $\psi_{mn}^{e/o}$ of the VSWF for different boundary conditions.

The coefficients define how strongly a certain electric or magnetic VSWF contributes to the scattering process. Here, n denotes the multipole order, e.g., $n = 1$ denotes the dipole moment and $n = 2$ the quadrupole moment, and higher order. The number m indicates the spatial orientation of the multipole. The first multipole moments such as dipole and quadrupole moments have a dominant contribution to the scattering process and can approximate the scattered electric field in the far field at a given wavelength. The different modes form the scattered electric field: $E \approx E_{ep} + E_{mp} + E_{EQ} + E_{MQ}$. Here E_{ep} , E_{mp} , E_{EQ} , E_{MQ} are the electric fields generated by the electric dipole moment, the magnetic dipole, the electric quadrupole, and the magnetic quadrupole, respectively.

By calculating the power of each multipole contribution, the effective scattering and extinction cross-section can be derived as follows:

$$\sigma_{sca} = \frac{\pi}{k^2 a^2} \sum_{n=1}^{\infty} \sum_{m=-l}^n (2l+1) [|a_{mn}|^2 + |b_{mn}|^2]$$

30

$$\sigma_{Ext} = \frac{\pi}{k^2 a^2} \sum_{n=1}^{\infty} \sum_{m=-l}^n (2l+1) \text{Real}(a_{mn} + b_{mn})$$

31

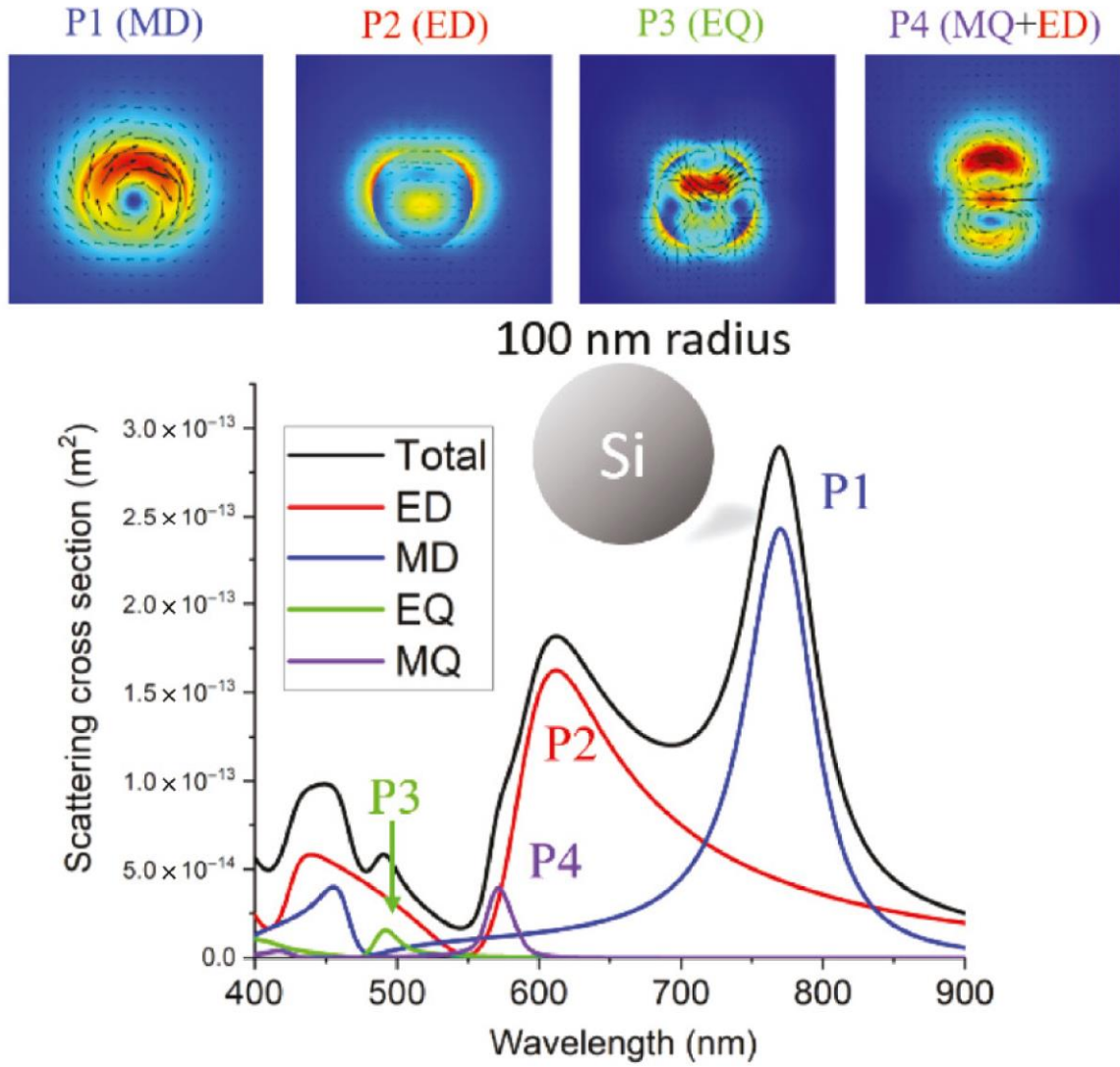


Figure 4. The multipole expansion of scattering spectra in a 100-nm-radius Si nanosphere. The contribution of dipole and quadrupole modes are given, E-field distributions at each peak of multipole modes are shown at the top, and black arrows denote the orientation of E-fields [15].

Figure 4 shows the scattering cross-section and the multipole expansion in the case of silicon nanoparticles with a size of 100 nm. From the figure, it is evident that at different wavelengths, different multipole moments dominate. For example, at a wavelength of 785 nm, the electric field plot shows a vortex nature which is typical for the magnetic dipole mode. At position P2, at around 620 nm, the electric field plot has an entirely different shape. Here, one can see a

horizontally aligned electric field, which resembles an electric dipole. P3 shows a spectral position where the electric quadrupole moment dominates. Here, the electric fields have a quadrupolar shape. Since all multipolar moments have some bandwidth, the electric field at a given position naturally contains magnetic and electric resonances with different orders, as seen at position P4. The electric field is composed of a magnetic quadrupolar mode and an electric dipole, resulting in a more complex electromagnetic field configuration. Note that mixing Mie resonances results in resonances that behave differently from the resonances that compose them. For example, an anapole mode is composed of toroidal and electric dipoles of similar amplitude but are out of phase and interfere destructively in the far-field. As a result, the anapole mode is a non-radiating mode, as illustrated in Figure 5. Note that toroidal modes appear in the above-mentioned multipole decomposition by a coordinate transformation. Here the multipole decomposition is performed in cartesian coordinates instead of spherical coordinates, and the toroidal dipole appears as an eigenmode in the multipole decomposition in the cartesian coordinate system [34].

The goal of this chapter was to introduce Mie resonances, since they play a crucial role in understanding the scattering from nanoparticles. Although, only the scattering problem of a nanosphere in a uniform medium can be solved analytically, the classification of electromagnetic fields in magnetic and electric multipole resonances also applies to more complex geometries and can be used to describe various optical effects, as the Kerker effect or anapole modes, as shown in Figure 5. In the following, we show that we can resonantly enhance and manipulate higher harmonic generation by using certain Mie resonances. Another example, where Mie theory provides a compelling picture for understanding an electromagnetic system are symmetry protected quasi-bound states in the continuum (QBICs), where the emission of a Mie mode can be suppressed by arranging the particles in a periodic array and due to the symmetry of the Mie resonance, as explained in Chapter 5.

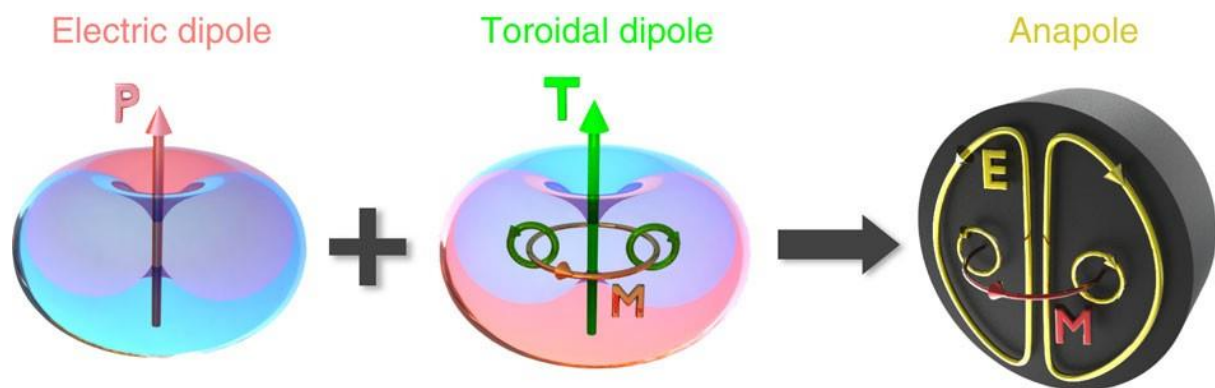


Figure 5. A toroidal dipole and an electric dipole overlap spectrally. Since the symmetry of the radiation patterns of the electric P-dipole and the toroidal T-dipole is similar, they can interfere destructively, resulting in total scattering cancellation in the far field with non-zero excitation from the near field. [34]

2.3 The “material side” of optical scattering and the optical properties of amorphous silicon

In the previous chapters, I explained how light is scattered by small dielectric particles, where the scattering depends on the size and geometry of the particle, and the material properties are represented by the refractive index. In this Chapter, I will explain the optical properties of amorphous silicon since the optical response of a scatterer depends not only on its shape but also on how the material itself responds to light. In this work, I use silicon as a material because silicon has advantages over other materials in view of nanostructures. First, silicon can be deposited on a variety of substrates. Second, resonant nanostructures made of silicon can be small compared to the resonant wavelength due to its high refractive index (the magnetic resonance is given approximately by $\lambda_r \sim D/n$ [35] where D is the diameter of the nanostructure). That is, a high refractive index leads to better light confinement. In addition, dissipative losses are negligible above a wavelength of 700 nm so that silicon nanostructures can exhibit Mie resonances in the infrared with low absorption. Therefore, silicon nanostructures can withstand higher pump powers without being damaged and have higher quality factors, which are advantageous for nonlinear processes.

In the first part of this chapter, I will explain the electronic band structure of silicon in view of its linear optical properties. Later, I will introduce its nonlinear optical properties by generally introducing the nonlinear optics and then explaining the nonlinear optical response of silicon nanostructures in terms of Mie resonances.

Solid silicon exists in three configurations: as a single crystal, as a polycrystalline form in which a lump of silicon consists of various micrometer-sized crystals, or as an amorphous form with very low crystallinity. Amorphous silicon is the disordered modification of crystalline silicon and has no long-range order because the bond lengths and angles are distorted or unsaturated (dangling bonds) due to the disordered placing of the silicon atoms in space, as shown in Figure 6a. [36]

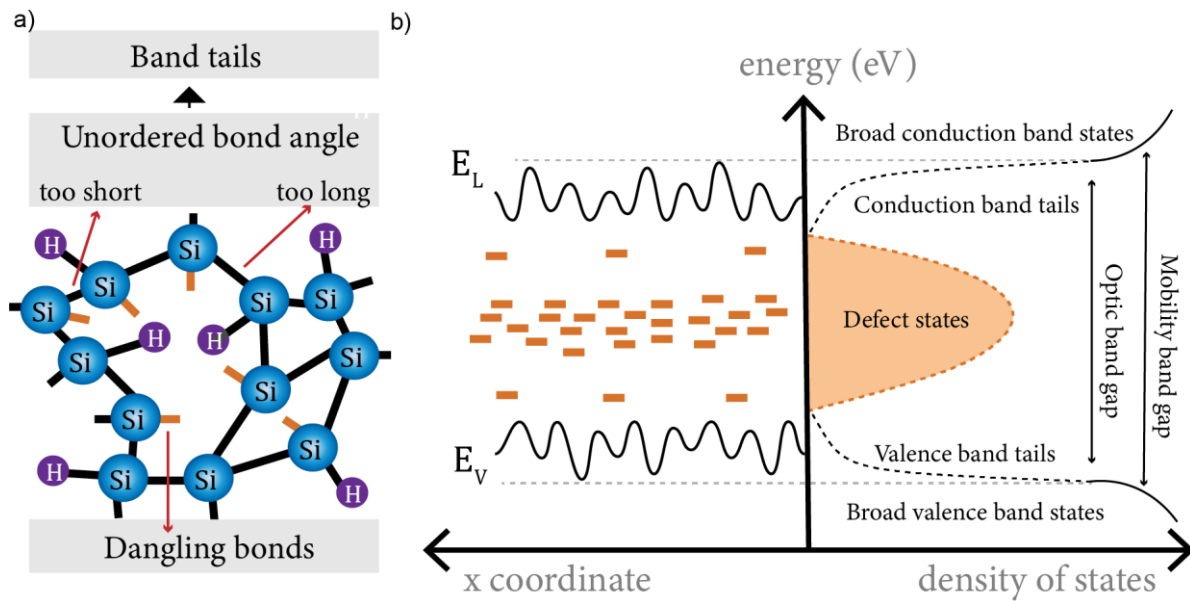


Figure 6. a) Exemplary spatial arrangement of amorphous silicon. The Si denotes the silicon atoms, the H denotes hydrogen, and the green bonds are unsaturated "dangling" bonds. b) The distorted bond angles of the Si atoms lead to energy fluctuations in the position space, resulting in band tails in the density of states. The energy levels of the unsaturated bonds lie in the middle of the band gap and form deep defect states. Recreated from Ref. [37].

Amorphous silicon is a semiconducting material but due to its disordered state the semiconductor properties like the wave functions of the charge carriers are hard to define. For example, the distortion in bond angle and length leads to charge carrier scattering, broadening of the density of states, and fuzziness in the wave vector of the electronic wavefunction and the electrical and optical properties of amorphous silicon differ significantly compared to electrical and optical properties of crystalline Si. In addition, amorphous silicon has poor semiconducting properties due to its high density of defects and dangling bonds. To reduce the defect density and improve the semiconducting properties, the dangling bonds can be saturated by hydrogen, which is called hydrogenated amorphous silicon (a-Si:H) [36]. An advantage of hydrogenated amorphous silicon is that it can be deposited directly onto a remote substrate using various methods. A well-known method for the deposition of amorphous silicon is plasma-enhanced chemical vapor deposition (PECVD), in which silane gas (SiH_4) is decomposed into a plasma of radicals and ions of the different combinations of silicon and hydrogen by an electromagnetic RF source.

Figure 6b shows the position space and the density of states in amorphous silicon. Here, due to the disorder, the density of states develops "band tails" near the valence and conduction band. In the band tails, the wavefunction of the electrons and holes is spatially localized and therefore does not participate directly in electronic transport. The dangling bonds create deep, highly localized electronic states in the middle of the bandgap, as shown in Figure 6b. These defects act as the main recombination centers in amorphous Si for electrons and holes

and can be neutral (D^0 , occupied by an electron) or positively (D^+ , unoccupied by an electron) and negatively (D^- , occupied by two electrons) charged. Since the amorphous Si is highly distorted, it is difficult to define the optical band gap. However, due to the nature of the band tails, it is possible to define a mobility gap, where the mobility of the charge carriers that can interact with light increases by several orders of magnitude. The mobility gap has a value of ~ 1.7 eV, which is significantly larger than the band gap of crystalline Si (~ 1.1 eV). Moreover, the uncertainty of the wave vector is of the same order as the wave vector itself, which means that the momentum of the charge carriers in amorphous Si is strongly broadened and therefore not well defined. As a result, photon absorption is unrestricted in terms of momentum and band structure, since there is always a wave vector that preserves the momentum of electrons and holes. Consequently, amorphous Si is a quasi-direct semiconductor with an increased absorption coefficient in the visible wavelength region compared to crystalline Si, where the optical absorption is phonon-assisted since crystalline Si is an indirect bandgap semiconductor. [36] Due to these effects, the refractive index and absorption of amorphous Si increase sharply in the visible region below 730 nm (~ 1.7 eV), as shown in Figure 7. The refractive index is almost constant in the infrared, and absorption is low away from the bandgap, where the optical response is mainly driven by bound charges. [36]

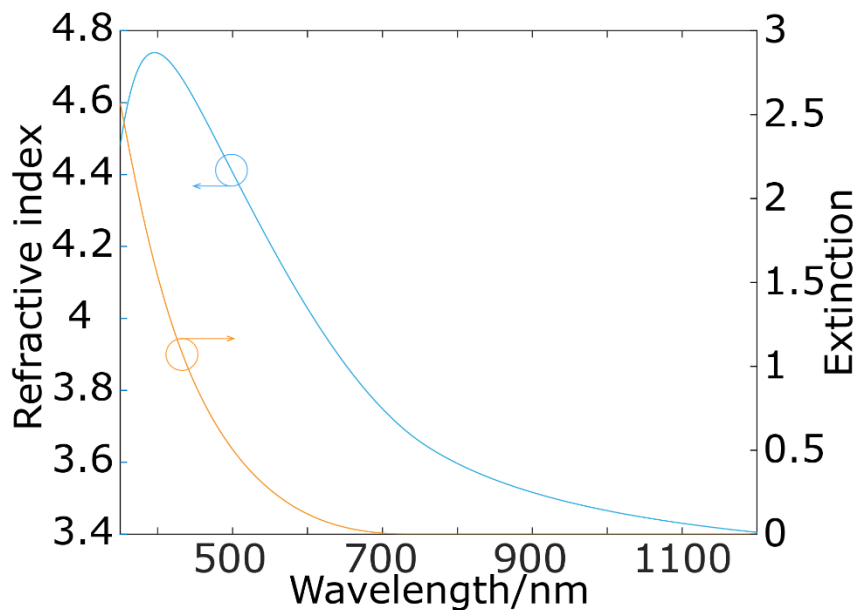


Figure 7. Refractive index and extinction of hydrogenated amorphous silicon from 350 nm to 1200 nm.

2.4 Nonlinear Optics

For non-magnetic materials, the material's electromagnetic response is given by the induced polarization vector $\vec{P}(\vec{r}, t)$. Typically, an external electric field induces collective displacement of electric charges. The displacement leads to a scattered field, which influences the propagation of the external electric field. Therefore, the dependence of the induced polarization to the electric field is given by [3]:

$$\vec{P}(\omega) = \epsilon_0 \chi^{(1)}(\omega) \vec{E}(\omega)$$

32

Where ϵ_0 is the dielectric constant of free space and $\chi^{(1)}(\omega)$ is the linear susceptibility, which relates the material properties to an electric field. Here, the induced polarization is linear proportional to an external electric field, and the light-matter interaction leads to well-known effects such as refraction of light on boundaries with different refractive indices and reflection of light on the surface of metals. However, with the advent of lasers that provide large electric field strength, the material's response deviates from equation 32, as the incident electric field can distort the electronic orbits of the atoms itself, changing the optical properties of the material.

Assuming a monochromatic wave and an instantaneous response of the material (see Ref. [3] for a detailed explanation), the nonlinear behavior of a material in response to an electric field can be captured by expanding the induced polarization (equation 32) with higher order terms:

$$\vec{P}(\omega) = \epsilon_0 [\chi^{(1)}(\omega) \vec{E}(\omega) + \chi^{(2)}(\omega) \vec{E}(\omega)^2 + \chi^{(3)}(\omega) \vec{E}(\omega)^3 + \dots]$$

33

With $\chi^{(2)}(\omega)$ and $\chi^{(3)}(\omega)$ represent the second-and third-order nonlinear susceptibility, respectively. While typical values for $\chi^{(1)}(\omega)$ are of the order of 1, typical values for second- and third-order susceptibility are $\chi^{(2)}(\omega) \sim 0.1 \frac{nm}{V}$ and $\chi^{(3)}(\omega) \sim 0.1 \frac{nm^2}{V^2}$.

This equation gives rise to the generation and propagation of light at new frequencies and other nonlinear phenomena, which can occur due to the nonlinear interaction of matter and light. For a better assessment of the effects which arise from the nonlinear interaction of light and matter one separates equation 33 into its linear part, as defined in equation 32 and the nonlinear part $P^{NL} = \epsilon_0 [\chi^{(2)}(\omega) \vec{E}(\omega)^2 + \chi^{(3)}(\omega) \vec{E}(\omega)^3 + \dots]$. P^{NL} is the source of nonlinear effects, and can be used to illustrate nonlinear optical phenomena.

If only third order effects under monochromatic illumination are considered, the nonlinear polarization can be simplified to:

$$P^{(3)}(\omega) = \epsilon_0 \chi^{(3)}(\omega) E^3(t)$$

34

To illustrate the possible nonlinear effects like wave mixing or higher harmonic generation, assume that illumination is with a monochromatic wave ($E(t) = E e^{-i\omega t} + c.c$) and the nonlinear polarization is as follows:

$$P^{(3)} = \epsilon_0 \chi^{(3)} [E^3 e^{-i3\omega t} + c.c] + 3\epsilon_0 \chi^{(3)} [E^2 E^* e^{-i\omega t} + c.c.]$$

35

The first term describes the generation of the third harmonic (THG) with $\omega_{THG} = 3\omega$, which is the main subject of this work, the principle is illustrated in Figure 8. The second term describes an electromagnetic field at ω , which changes the refractive index of the material during the propagation of the fundamental wave and, the phase of the fundamental wave depending on its intensity I : $n = n_0 + n_2 I$ Where n_0 is the linear refractive index, I is the field intensity and

$$n_2 = \frac{3}{2n_0^2 \epsilon_0 c} \chi^{(3)}$$

36

This modulation of the refractive index by a sufficiently strong electromagnetic wave results in self-phase modulation. If the propagating wave has a Gaussian or similar spatial intensity shape, the self-phase modulation is stronger in the center of the beam and becomes weaker toward the sides, and the self-phase modulation acts as a lens on itself. This effect is called self-focusing and is used in lasers to produce pulses of femtosecond duration. Note that, if the fundamental field is a superposition of three monochromatic waves at three different wavelengths ω_1, ω_2 and ω_3 : $E(t) = E_1 e^{-i\omega_1 t} + E_2 e^{-i\omega_2 t} + E_3 e^{-i\omega_3 t} + c.c.$. The third order response will lead to the generation of various new frequencies where one gets the sum or difference frequency of the three fundamental waves beside the THG at frequencies $3\omega_1, 3\omega_2$ and $3\omega_3$ as illustrated in Figure 8. Besides the illustrated effects, there exist more wave mixing processes, as explained in Ref. [3].

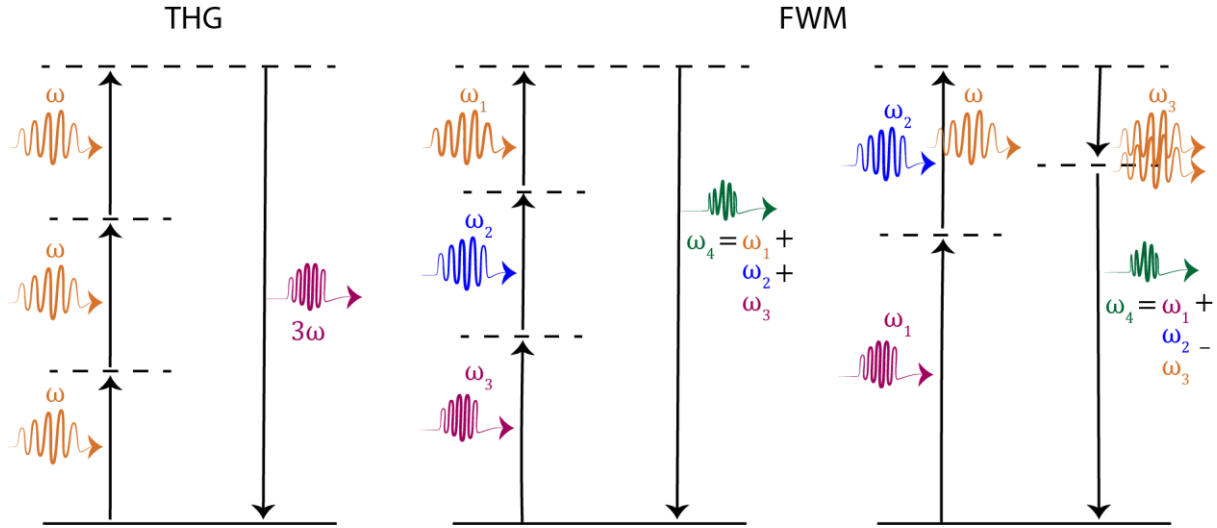


Figure 8. Schematic overview over different third order processes, where three photons interact to generate new photons. THG: three photons at a fundamental frequency interact to create one photon at three times the frequency of the fundamental photons. FWM: Three photons with different frequencies interact to create photons at $\omega_4 = \omega_1 + \omega_2 + \omega_3$ or $\omega_4 = \omega_1 + \omega_2 - \omega_3$. Recreated from Ref. [31].

2.5 The third-order response of amorphous silicon

In the above, the nonlinear susceptibility was introduced as a 1D coefficient to describe nonlinear phenomena such as THG. In most cases, the nonlinear susceptibility coefficients depend on the direction of the applied electric fields and the material symmetry plays an essential role in the nonlinear optical properties of the overall tensor following Neumann's principle. Therefore, the i^{th} component of the nonlinear polarization vector in cartesian coordinates can be written as [3]:

$$P_i^{NL} = \epsilon_0 \left[\sum_j \chi_{ij}^{(1)} E_j + \sum_{j,k} \chi_{ijk}^{(2)} E_j E_k + \sum_{j,k,l} \chi_{ijkl}^{(3)} E_j E_k E_l + \dots \right]$$

37

Where $\chi^{(3)}$ is a third rank tensor and $\chi_{ijk}^{(3)}$ denotes its tensor elements. $\chi^{(3)}$ is a fourth rank tensor and $\chi_{ijkl}^{(3)}$ denotes the tensor elements. Here, $\{i, j, k, l\} \in \{x, y, z\}$ denote the different directions of the electric field in cartesian coordinates. The subscript i determines the generated nonlinear induced polarization component at the higher harmonic resulting from a fundamental electric field with components in the j, k, l directions.

However, depending on the order of the tensor, the nonlinear susceptibility tensor can have a complex structure with many components, for example $\chi^{(3)}$ has 81 components. Nevertheless, the nonlinear susceptibility tensor can be drastically simplified by considering material and mathematical symmetries, such as spatial symmetry, permutation symmetry or Kleinman's symmetry (which states that the third-order susceptibility is frequency independent, and the material responds instantaneously to applied E-fields). Regarding the symmetry of an isotropic material, all coordinate axes are equivalent and the components of $\chi^{(3)}$ must follow the isotropic symmetry, following Neumann's principle [3]:

$$\begin{aligned}\chi_{xxxx}^{(3)} &= \chi_{yyyy}^{(3)} = \chi_{zzzz}^{(3)} \\ \chi_{xxyy}^{(3)} &= \chi_{xxzz}^{(3)} = \chi_{yyxx}^{(3)} = \chi_{yyzz}^{(3)} = \chi_{zzxx}^{(3)} = \chi_{zzyy}^{(3)} \\ \chi_{xyxy}^{(3)} &= \chi_{xzzx}^{(3)} = \chi_{yzyz}^{(3)} = \chi_{yxxy}^{(3)} = \chi_{zxzx}^{(3)} = \chi_{zyyz}^{(3)} \\ \chi_{xyyx}^{(3)} &= \chi_{xzzx}^{(3)} = \chi_{yxxxy}^{(3)} = \chi_{yzzzy}^{(3)} = \chi_{zxzx}^{(3)} = \chi_{zyyz}^{(3)}\end{aligned}$$

38

Furthermore, all other components of $\chi^{(3)}$ vanish because these are the only tensor elements where the cartesian coordinates x, y, and z occur in even numbers and an index cannot occur in odd number. The reason for this is illustrated in the following example: The element $\chi_{yxxx}^{(3)}$ would produce a THG field in the y-direction due to an electric field in the x-direction. This response must disappear in an isotropic material because there is no reason why an isotropic material would produce a field in the y-direction instead of in the -y-direction and therefore this element vanishes [3]. The equation 38 gives four groups of elements. However, these four groups are not independent, because isotropy requires that the TH response of the material is the same in each axis. Therefore, if we rotate the coordinate system around an arbitrary axis, e.g. 45° around the z axis, resulting in $\{x', y', z\}$, any tensor component can be written in terms of the tensor elements $\chi_{xxyy}^{(3)}$, $\chi_{xyxy}^{(3)}$ and $\chi_{xyyx}^{(3)}$:

$$\chi_{ijkl}^{(3)} = \chi_{xxyy}^{(3)} \delta_{ij} \delta_{kl} + \chi_{xyxy}^{(3)} \delta_{ik} \delta_{jl} + \chi_{xyyx}^{(3)} \delta_{il} \delta_{jk}$$

39

Where δ_{ij} is the Kronecker delta and is 1 if the coordinates $i = j$ and 0 otherwise. From the condition, that all axes are equivalent, and that the TH response should not change with coordinate rotation, one can see that only 3 tensor elements are independent. Moreover, for THG we can assume that the order of the indices j, k, and l do not matter, since the three photons are indistinguishable at the fundamental frequency ω . That is, $\chi_{ijkl}^{(3)}(-\omega_i, \omega_j, \omega_k, \omega_l)$ is invariant under 4! permutations of the pairs (i, ω_i) , (j, ω_j) , (k, ω_k) and (l, ω_l) . E.g., consider

the index combination for the fundamental electric fields of jkl for the tensor element $\chi_{yyxx}^{(3)}$, due to the permutation symmetry the tensor components $\chi_{yxx y}^{(3)}$ and $\chi_{yxyx}^{(3)}$ need to be equal. In the end it is possible to derive an effective matrix that captures the nonlinear response in a matrix formalism by using the inherent permutation symmetry again [38]. In total, there are 10 different combinations of j , k , and l , and the three indices can be contracted to a single index m :

jkl	xxx	yyy	zzz	yzz	yyz	xzz	xxz	xxy	xyx	xyz
m	1	2	3	4	5	6	7	8	9	0

Due to permutation symmetry, the order of the indices can be exchanged so that the polarization vector can be written as an effective susceptibility matrix:

$$P^{(3)} = \begin{bmatrix} \chi_{11} & 0 & 0 & 0 & 0 & \chi_{11} & 0 & \chi_{11} & 0 & 0 \\ 0 & \chi_{11} & 0 & \chi_{11} & 0 & 0 & 0 & 0 & \chi_{11} & 0 \\ 0 & 0 & \chi_{11} & 0 & \chi_{11} & 0 & \chi_{11} & 0 & 0 & 0 \end{bmatrix} \begin{bmatrix} E_x^3 \\ E_y^3 \\ E_z^3 \\ E_y E_z^2 \\ E_y^2 E_z \\ E_x E_z^2 \\ E_x^2 E_z \\ E_x E_y^2 \\ E_x^2 E_y \\ E_x E_y E_z \end{bmatrix}$$

40

Which describes the THG in amorphous materials, especially silicon: Here $\chi_{11} = 0.25 \frac{nm^2}{V^2}$. In view of nonlinear optics silicon has some advantages compared to other materials, since the third order nonlinear susceptibility is high compared to other materials. A comparison of commonly used high refractive index materials for nonlinear nanostructures can be found in Table 1. Note that a high refractive index suggests a high third harmonic nonlinear susceptibility following Miller's rule [3]. Interestingly, the tensor in equation 40 generates a third harmonic signal only for linearly polarized light. If we calculate $P^{(3)}$ for circularly polarized light $\sigma = \pm 1$ and an electric field strength E_0 propagating through silicon in the z -direction with a wave vector k_z :

$$\vec{E} = \begin{bmatrix} E_0 \\ \sigma i E_0 \\ 0 \end{bmatrix} e^{ik_z z}$$

41

$P^{(3)}$ becomes zero for each component of the vector. For example, substituting equation 41 into the effective susceptibility equation 40 for the component $P_x^{(3)}$ returns: $P_x^{(3)} = \chi_{11} e^{ik_z z} (E_0^3 + E_0 (\sigma i E_0)^2) = 0$. In general, it can be shown that circularly polarized light propagating through an isotropic medium does not produce THG due to the nonlinear selection rules [39].

Table 1. Linear and nonlinear optical properties of common high-index dielectrics for THG in the infrared and visible.

Material	Refractive Index	$\chi^{(3)}$ [nm^2/V^2]
c-silicon	3.77-3.46 (700-1800 nm) [40]	0.25 (1550 nm) [41]
c-Ge	4.33-4.13 (1090-1800 nm) [42]	0.4 (2000 nm) [41]
$\text{Al}_{0.22}\text{Ga}_{0.78}\text{As}$	3.60-3.28 (720-1800 nm) [43]	0.07[44]
ZnO	2.22-1.92 (400-1800 nm) [45]	0.03 (1500 nm) [46]
TiO_2	2.84-2.27[47]	0.02[48]

2.6 The nonlinear conversion efficiency

For THG, the intensity of the third harmonic light in dependence of the fundamental pump beam in the non-depleted pump approximation is given by [49]:

$$I_{3\omega} = \frac{3\omega^2}{4\pi^2 \epsilon_0^2 c^4 n_{3\omega} \omega_0^4} (\chi^{(3)})^2 |J|^2 I_\omega^3$$

42

Here, I_ω and ω_0 are the intensity and the beam waist of the fundamental beam at the pump wavelength. J denotes the phase-matching condition and is given by $|J|^2 = L^2 \text{sinc}\left(\frac{\Delta k L}{2}\right)$. In the equation $\Delta k = 3k_{3\omega} - k_\omega$ denotes the phase mismatch between the fundamental light and third harmonic, and L denotes the length of the nonlinear material. This equation gives the THG intensity for a pump beam propagating through a nonlinear optical crystal. For nanostructures, the THG intensity is different because different Mie modes and coupling conditions play a role in the nonlinear conversion process in nanostructures and it is difficult to establish a general equation. Note that due to the thickness of nanostructures in the subwavelength region, the phase matching conditions play a minor role. However, equation 42 gives an idea of the parameters that are important in a nonlinear conversion process, such as the third-order nonlinear susceptibility and the intensity of the pump beam. Note that the intensity at the third harmonic frequency scales with the cubic number of the pump intensity,

which is a crucial feature of THG. If the average pump intensity and the average intensity of the TH light are known, the efficiency of the THG process can be defined as follows:

$$\eta = \frac{I_{3\omega}}{I_{\omega}} \quad 43$$

The efficiency scales with the square of the mean pump power since the mean TH power $I_{3\omega}$ depends on the third power of the pump intensity, as can be seen from equation 43: $\eta \sim I_{\omega}^2$. However, when different metasurface designs in different optical setups with different pump intensities are measured and compared, such a definition is not sufficient, since theoretically any efficiency can be achieved by increasing the intensity of the fundamental pump beam. Therefore, the equation 43 does not distinguish between efficiency and effectiveness. To get around this, the average TH power can be divided by the cubic number of the average input power [50]:

$$\zeta_{THG} = \frac{I_{3\omega}}{I_{\omega}^3} \quad 44$$

This efficiency ζ_{THG} , which is independent of the pump power, is measured in $1/W^2$. A similar definition exists for other harmonic processes. The definitions above use average power to derive the nonlinear conversion efficiency. Although, many experimental setups use picosecond or femtosecond lasers because they provide much higher peak powers, and the metasurface generates TH light in a parametric response to the pulsed laser light. A metasurface pumped with a pulsed laser generates a TH signal only when a laser pulse interacts with the metasurface. For this reason, the crucial basis for the nonlinear conversion efficiency is the peak power \hat{P} of the pump beam and the THG light. However, it is often the average power rather than the peak power of a single laser pulse that is measured, and the average power and the peak power can be related as follows: $\hat{I} = \frac{I}{R\tau} = \frac{I}{duty\ cycle}$. Here, R is the repetition rate of the laser pulse. The duty cycle is the product of the pulse length and the repetition rate and indicates the proportion in which the laser is active. If we assume that the pulse length of the third harmonic light is equal to the pulse length of the laser $\tau_{THG} \approx \tau_{pump}$, the power independent peak power conversion efficiency can be written as follows [50]:

$$H_{THG} \approx \frac{\hat{I}_{3\omega}}{I_{\omega}^3 (R\tau)^2} \quad 45$$

Table 2. Comparison of the different nonlinear optical elements for THG. The values are taken from the publications and the table is recreated and extended from Ref [13]. The entry for the BBO crystal was calculated based on information provided by the manufacturer (EKSMA): Ti:Sa Super Spitfire Laser operating at 1 kHz, 130 fs pulse width, 100 μ J pulse energy at 800 nm, beam diameter 1 mm.

Dielectric material	Design	Operation mode	Pump wavelength [nm]	Peak pump intensity [GW/cm ²]	Efficiency η and (H_{THG})
Si [51]	Single nano cylinders on glass	Magnetic dipole resonance at fundamental wavelength (FW)	1260	4.5	8×10^{-8} $(10^{-10} \frac{1}{W^2})$
a-Ge [52]	Single nano cylinders on glass	Magnetic dipole resonance at FW	1650	0.8	5×10^{-6} $(5 \times 10^{-9} \frac{1}{W^2})$
a-Si [20]	Metasurface of nanodiscs	Q-BIC Resonance at FW	1345	1	10^{-5} $(10^{-7} \frac{1}{W^2})$
Si [53]	Metasurface with T shaped nano-objects	QBIC resonance at FW	1587	0.06	5×10^{-8} $(10^{-5} \frac{1}{W^2})$
Au [54]	Metasurface with metallic split-ring resonators	Magnetic dipole resonance at FW	1500		3×10^{-12}
Beta Barium Oxide (BBO) (Eksma FKE-800-100)[7]	BBO crystal with a thickness of 500 μ m	Phase matched THG crystal	800	39	8×10^{-2} $(1.2 \times 10^{-4} \frac{1}{W^2})$

This definition gives a nonlinear conversion efficiency that is independent of the laser system and can be used to compare different metasurface designs and resonant gain mechanisms against each other. However, much intuitive understanding is lost between equation 43 and 45. One could interpret equation 45 as follows: Equation 45 measures the nonlinear conversion efficiency of a system per “ontime of the laser” and per input power, normalized to the nonlinear power law $I_{3\omega} \sim I_{\omega}^3$. This definition is mostly used to describe the nonlinear conversion efficiency of metasurfaces or resonant nano-objects. There are several limitations of this equations: First, it is derived in the undepleted pump approximation and that we assume no back-conversion from the TH to the fundamental field. Second, we assume that the pulse length of the third harmonic light is equal to the pulse length of the fundamental field. For resonances with high quality factors, the interaction between the resonator and the light may alter the pulse length of both beams. Table 2 gives an overview of different THG conversion efficiencies in experimentally realized optical elements and metasurfaces. The table shows the different conversion efficiencies compared to their design, material, and resonance/operation mode. From the table, plasmonic metasurfaces have very low conversion efficiencies due to their high ohmic losses and low damage thresholds. Higher efficiencies can be achieved by Mie resonances in high refractive index dielectric materials due to the low absorption losses and high damage threshold away from the band gap of the material. For example, the extinction coefficient of crystalline silicon at 1200 nm is in the range of 10^{-7} [40, 55] and the extinction coefficient of gold is in the range of 6 to 8 at 1200 nm [56, 57]. Therefore, compared to dielectric nanostructures, plasmonic nanostructures absorb more electromagnetic energy and convert it into heat, and this energy is no longer available for third harmonic generation. As a result, plasmonic nanostructures have a lower damage threshold and lower nonlinear conversion efficiency. However, besides the high absorption losses, another reason for the lower conversion efficiency of plasmonic nanostructures compared to dielectric structures is the smaller mode volume of plasmonic nanostructures. First, plasmonic nanostructures are thinner in the direction of light propagation. Typical thicknesses are between 30 nm and 50 nm, while dielectric structures have a thickness of 300-700 nm. Second, the higher nonlinear conversion efficiency of dielectric metasurfaces compared to their plasmonic counterparts is due to the fact that plasmonic resonances are mainly confined to the surface of the metal particle due to the skin effect [14]. Even though, the nonlinear coefficients of metals and dielectrics are similar (silicon is in the range of $\chi_{Si}^{(3)} = 0.25 \text{ nm}^2/\text{V}^2$, gold $\chi_{Au}^{(3)} = 0.2 \text{ nm}^2/\text{V}^2$). Therefore, the main contribution of the metallic particle to the generation process stems from the surface of the particle and the bulk nonlinear susceptibility has a negligible contribution. As shown in the last chapter the Mie resonances of dielectric nanoparticles are located inside the particle and not only on the surface. Therefore, they can easily access the bulk nonlinearity of the material. In view of light-matter interaction, Mie resonances provide an enhanced light-matter interaction, that results in a low quality factor because the electromagnetic energy can be easily re-emitted. To increase the nonlinear conversion efficiency further, we can use resonances with higher quality factors

($Q > 150$) at the fundamental and third harmonic wavelengths, since the excitation coefficient α of the third harmonic depends on the quality factors Q_ω and $Q_{3\omega}$ of the involved resonances at the fundamental and third harmonic frequencies, and on the mode overlap between the involved resonances $\zeta_{\omega \rightarrow 3\omega}$ [58]:

$$\alpha \sim Q_{3\omega} Q_\omega^3 \zeta_{\omega \rightarrow 3\omega}$$

46

A physical explanation for this equation is that a quality factor leads to a long lifetime of an excitation at the resonance wavelength, which increases the interaction time of the electromagnetic wave with the material of the nanostructure, which in turn also increases the nonlinear interaction. To achieve higher conversion efficiencies, one can use the concept of quasi-Bound states in the continuum (QBIC), which have significantly higher quality factors, but the free-space coupling is restricted. We will explain QBIC and their challenges later in Chapter 5. However, metasurfaces with QBIC states have provided with the highest nonlinear conversion efficiency up to the date. Looking at the last entry in Table 2 which shows the efficiency of a commercially available THG kit, the QBIC metasurfaces almost reach the efficiency of conventional available nonlinear elements. At the same time, metasurfaces can reduce the thickness of nonlinear optical elements by several orders of magnitude, as a dielectric metasurface is typically 500 nm thick, compared to the 500 μm thickness for the nonlinear BBO crystal [7]. In addition, metasurfaces allow excellent design freedom in terms of spatial wavefront shaping and polarization control, which may enable new applications that require enhanced nonlinear interaction, along with simultaneous propagation control.

2.7 Third harmonic generation from a nano cylinder

In this section, I describe how Mie modes can be used to improve nonlinear conversion efficiency. Consider the case of THG from a nano-cylinder suspended in air. Here, the interaction of light and matter can be divided into two steps: First, the linear scattering, where an external wave $[E_{\text{inc}}, H_{\text{inc}}]$ excites the nanoresonator, results in a scattered electromagnetic field $[E_s, H_s]$ at a wavelength λ . Second, due to the nonlinear susceptibility, a nonlinear induced polarization builds up in the cylinder according to equation 40. This induced polarization is the driving source of a secondary wave at $\lambda/3$ with a total electromagnetic field of $[E_t^{(3)}, H_t^{(3)}]$. This physical picture is based on two approximations: First, the non-depleted pump approximation, assuming that the nonlinear interaction is weak, and that material absorption and scattering are the dominant loss channels. Second, other nonlinear processes are negligible: Light at the THG wavelength does not couple back to light at the fundamental wavelength, and the Kerr effect, as well as two photon absorption [3, 59] is negligible.

If the solution $[E_t^{(3)}, H_t^{(3)}]$ is known, the energy density $W_{sca}^{(3)}$ at the third harmonic frequency can be calculated, and the nonlinear scattering cross-section can be defined analog to Chapter 2.1 as follows:

$$\sigma_{sca}^{(2)} = \frac{W_{sca}^{(3)}}{S_0} = \oint_{\Sigma} \text{Re}(\vec{J}_t^{(3)*} \times \vec{E}_t^{(3)}) \cdot \vec{n} d\sigma$$

47

In addition, with the knowledge of $W_{sca}^{(3)}$, which can be extracted from a numerical simulation, the THG conversion efficiency can be calculated as:

$$H_{THG} = \frac{W_{sca}^{(3)}}{S_{in}^3}$$

48

Here, we simulated an amorphous silicon cylinder suspended in the air with a diameter of 365 nm and a height of 365 nm as shown in Figure 9a. As shown in the picture, the simulation domain is a sphere with the cylinder in the center. Around the sphere is a perfectly matched layer that absorbs the scattered light, so that back reflections from the domain boundary into the simulation space do not affect the scattering problem and the whole system behaves like a single cylinder in an infinite airspace. The refractive index of the cylinder is presented in Figure 7. In a first step, the scattering problem was solved numerically at fundamental wavelengths between 1000 nm and 1600 nm. An x-polarized incident plane wave with $\vec{E} = (E_0 e^{ik_z z}, 0, 0)$, was used as the background field. Then the scattered field $[E_s, H_s]$ in the whole simulation domain was numerically determined. The extinction cross-section is then calculated according to $\sigma_{ext} = \frac{W_{ext}}{I}$. In the second simulation step, the solution of the internal electromagnetic fields of the nanocylinder is used as the source for the nonlinear electromagnetic fields at a wavelength from 333 nm to 533 nm. To achieve this, we used equation 40 to calculate the induced nonlinear polarization using the Comsol module for polarization. The components of the electric field inside the nanocylinder at the fundamental wavelength were inserted into the effective tensor and the nonlinear induced polarization was calculated, which serves as the source for the nonlinear signal at the third harmonic wavelength.

In the linear scattering regime, the extinction cross section of the cylinder is shown in Figure 9b. Here, the effective extinction cross section shows a maximum originating from the magnetic dipole resonance at 1510 nm, as can be seen from the electric field plot (Figure 9d), which shows a vortex in the x-z plane which is characteristic for a magnetic Mie resonance. In addition, the magnetic field shows a strong alignment with the x-axis in the x-y plane since the

incident plane wave is polarized in the x-direction. The second peak in the extinction cross section at 1190 nm is lower compared to the magnetic dipole and comes from the electric dipole (Figure 9c). Here the roles are reversed. The magnetic field shows a vortex in the x-z plane and the electric field shows a strong alignment to the x-axis in the x-y plane. Compared to the electric dipole, the magnetic dipole shows a stronger field enhancement inside the cylinder, which is beneficial for nonlinear processes. Table 2 suggest that the magnetic dipole resonance shows the strongest enhancement in the nonlinear conversion efficiency. The maximum THG conversion efficiency is estimated as in the order of $10^{-3} \frac{1}{W^2}$. In comparison with Table 2, this value is higher. This is due to the fact that here, we look at an ideal system which is simplified and does not account for two photon absorption [51, 59] or fabrication induced defects. In addition, in the simulation, the light is collected in every direction, which is almost impossible in an experimental setup. These results show that a dielectric cylinder can already generate a strong nonlinear signal by utilizing Mie resonances.

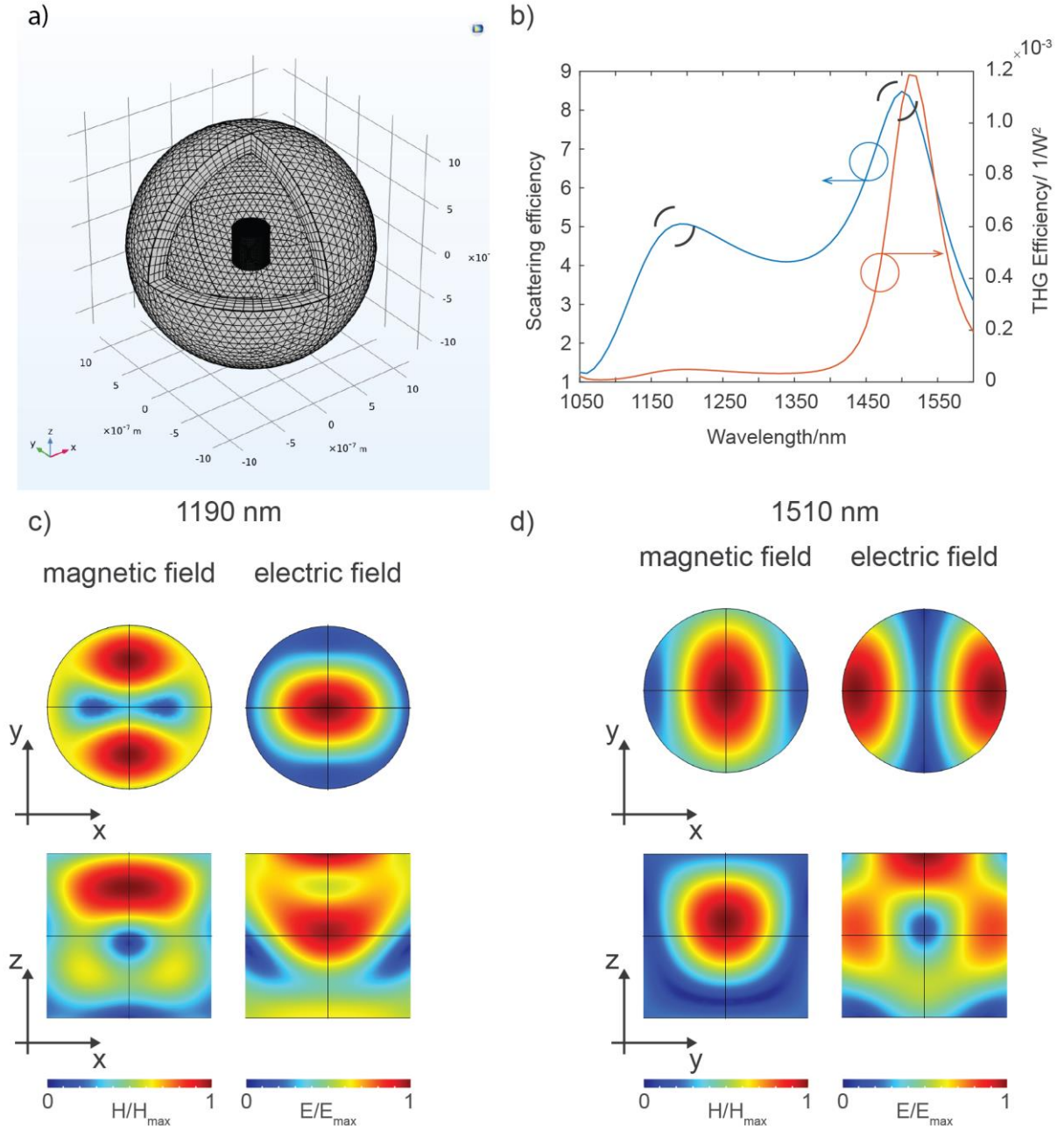


Figure 9. a) Overview of the simulation domain. The silicon cylinder is located in the center. The simulation area is surrounded by a perfectly matched layer. b) The scattering cross section of a silicon cylinder for different wavelength (blue). The nonlinear conversion efficiency at the third harmonic wavelength as a function of the fundamental wavelength. b) electric and magnetic field plots at different wavelength.

Chapter 3 Enabling nonlinear optical engineering: Fabrication technology

To control light at the nanoscale, we need fabrication techniques which can produce subwavelength resonators and arrays of dielectric nanostructures. A commonly used technology is electron beam lithography and dry etching to realize these nanoresonators. The nanofabrication of dielectric metasurfaces takes several steps, depicted in Figure 10a-d. At first, an amorphous silicon (a-Si) film is deposited on a glass substrate by plasma-enhanced chemical vapour deposition (PECVD). Afterward, a thin film of poly-methyl-methacrylate (PMMA) resist is spin-coated onto the a-Si film and baked on a hot plate. Since the prepared substrate is semi-insulator, a film of conductive polyaniline was spin-coated on top of the resist to reduce the charging of the sample during the electron beam lithography (EBL). Subsequently, the nanostructures are patterned by EBL. The sample is developed in a MIBK:IPA solution and then washed with IPA to develop the patterns. Then the developed sample is placed in an electron beam evaporator and coated with a Cr layer. The excess Cr is removed by dissolving the resist in acetone and subsequent cleaning within a dimethyl succinate solution followed by an ultrasonic treatment. Then, the Cr nanostructures are etched into the a-Si film by using inductively coupled plasma reactive ion etching (ICP-RIE) that results a-Si nanofins with almost vertical sidewalls. Finally, the Cr is removed in a Cr etching solution. The fabricated structures are illustrated in Figure 12.

Now we give a detailed overview of the different process steps.

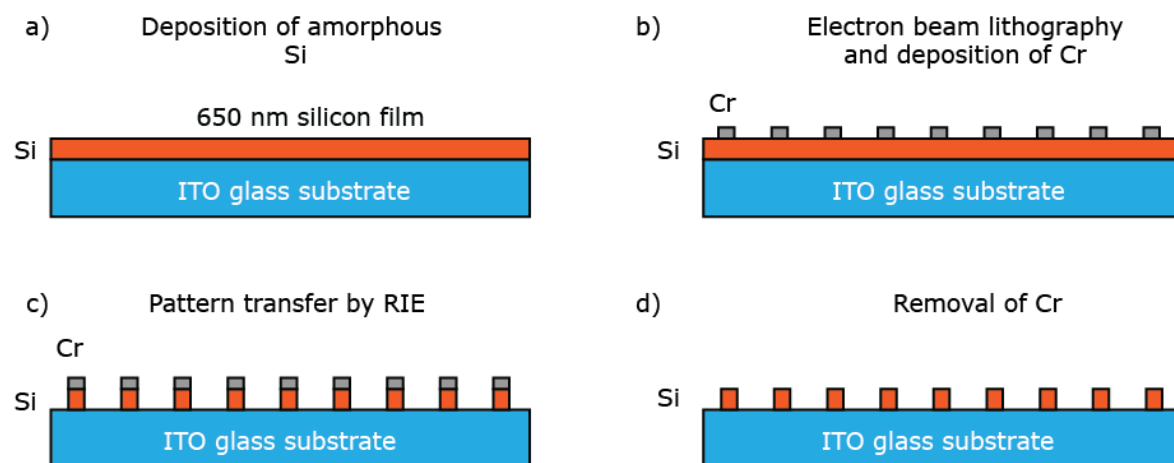


Figure 10. a) Deposition of amorphous silicon on a ITO Glass substrate. b) Pattern transfer to PMMA resist by EBL. c) Inductively coupled reactive ion etching (ICP-RIE) to transfer Cr mask into amorphous Si nanofins. d) Cr removal [60].

3.1 Plasma Enhanced Deposition of amorphous silicon

Before depositing the amorphous silicon thin film of desired thickness on top of a glass or indium tin oxide (ITO) coated substrate, the substrate was first treated with a standard cleaning procedure: 15 minutes ultrasonic bath at 50°C - 60°C in acetone followed by 5 minutes ultrasonic treatment in an isopropanol bath. The cleaning procedure with acetone removes organic contaminants from the sample, while the isopropanol can dissolve nonpolar residues left by the acetone. Subsequently, the hydrogenated amorphous silicon (a-Si:H) thin film is deposited by PECVD. In this process, a mixture of 2% SiH₄ diluted in Ar with a flow rate of 400 sccm at 1 Torr is decomposed by an RF (@13.56 MHz) source with a power of 10 W into various ions and radicals generated in the plasma. Depending on the reactivity and staying time in the plasma, a selected fraction of those are able to take part in the film growth process. After different gas- and solid-phase reactions a-Si thin film is deposited on the substrate at a specific deposition rate (here, 23 nm/min). The substrate holder was heated to 200°C. The film thicknesses for the samples used in this work are 650 nm and 365 nm.

3.2 Resist Spin-Coating

The next fabrication step is to coat the substrate with an electron beam sensitive resist for the lithography. Here, we summarize the process; the detail about the process parameters is shown in Table 1. The spin coating process requires several steps. First, a thin layer of an adhesion promoter (Allresist 300-80 new, diphenylsilanediol) is spun onto the sample and annealed on a hot plate. During annealing, a uniform and thin layer of the adhesion promoter forms on the substrate. After annealing, the sample is rinsed with acetone and isopropanol to remove an excess adhesion promoter. The adhesion promoter reacts with the substrate surface to form highly stable Si-O bonds, which improve the wettability of the surface and the adhesion of the resist to the substrate surface [61].

Second, the electron beam resist is spun onto the substrate. In this work, we used resists made of poly(meth)acrylates (PMMA) with a mass of 950k dissolved in ethyl lactate to serve as a positive tone resist. Depending on the spin coating speed and PMMA concentration in the ethyl lactate, the coating thickness varies between 120 nm and 160 nm [61]. After spin coating, the samples are baked on a hot plate at a temperature in between 130°C and 180°C to remove the solvent. If the baking temperature of the resist is high (in the range of 170°C to 180°C), subsequent annealing of the substrate on a second hot plate at 90°C for 2 minutes is required to reduce stresses in the layer, achieve better layer quality and prevent cracking. Cracks and surface defects lead to an uneven conductive layer, which has a considerable impact on the achievable resolution of electron beam lithography. Therefore, it is vital to get an even surface when you apply the conductive layer to the resist. Cracks and surface defects lead to an uneven conductive layer, which has a significant impact on the achievable resolution of

electron beam lithography. In a final step, a conducting polymer (Allresist, Elektra 92, SX AR-PC 5000/90.1) layer is spun onto the substrate to prevent substrate charging during electron beam lithography [61]. It is spin-coated at a speed of 5500 rpm, resulting in a thickness of 46nm. After spin-coating, the resist is baked at 90°C on a hot plate. After the conductive layer is deposited, the substrate can be patterned using electron beam lithography. Note that the conductive layer is water soluble, therefore, can be removed in a water bath: The conductive coating itself is a mixture of polythiophenes, polystyrene sulfonates, and surfactants in an organic solvent mixture with isopropanol as the main component. Details of the parameters of the entire spin coating can be found in table 1.

Table 3. Spin coating parameter for different coating materials.

Step	Spin speed [RPM]	Spin time [s]	Baking temperature [°C]	Baking time [min]	Thickness [nm]
Adhesion Promoter	4000	30	60	2	-
PMMA 950k Option 1	4000	30	Baking:180 Tempering: 90	Baking: 2 Tempering: 2	160
Option 2	5000	30	Baking:180 Tempering: 90	Baking: 2 Tempering: 2	120
Conductive Layer	5500	30	90	2	46

3.3 Electron beam lithography (EBL) and development

A combined EBL/SEM system (Pioneer Raith I) performs all lithographic processes. It provides an accelerating voltage up to 30 kV and a minimum aperture of 7.5 μm (usually 10 μm is used because the difference in resolution between 7.5 μm and 10 μm aperture is insignificant, but provides a larger beam current, resulting in a faster writing speed). In electron beam lithography, an electron beam scans the surface of the substrate, which is covered with an electron-sensitive layer (the resist). By scanning the electron beam in a specific pattern across the resist, individual shapes can be drawn into the resist, since the chemical structure of the resist is altered by the electron beam exposure. In the case of PMMA, a positive tone resist, electron beam lithography promotes cleavage of the PMMA polymer chain, as shown in Figure 11. This process produces small unsaturated molecular fragments, including carbon monoxide, carbon dioxide, and methyl radicals. The fragments can later be resolved with a

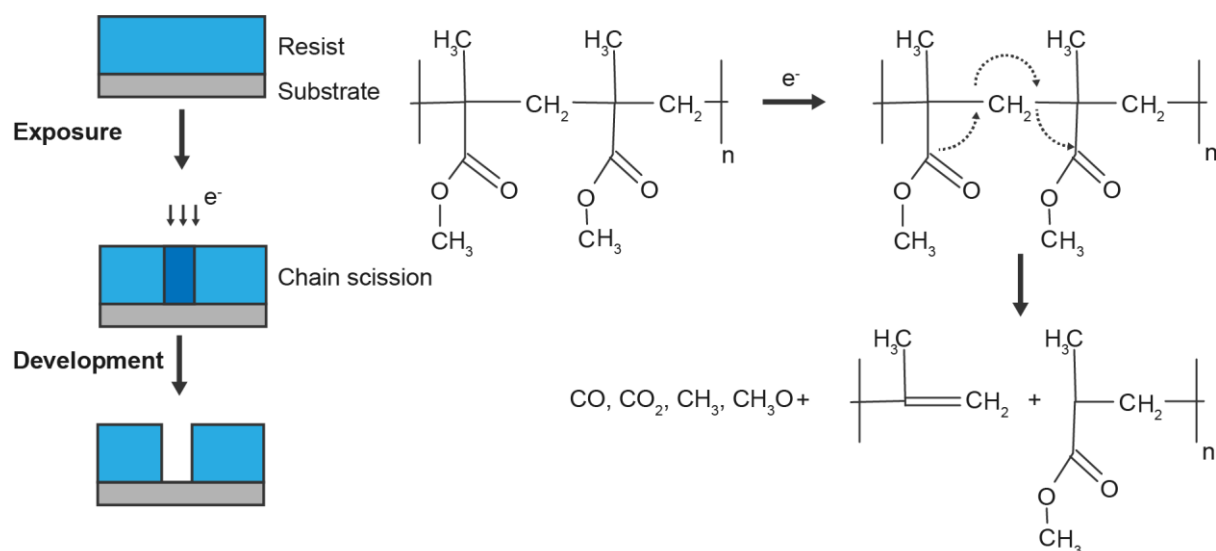


Figure 11. Irradiation of an electron beam resist with an electron beam leads to chain scission in the exposed regions of the PMMA resist. This process produces small unsaturated molecular fragments, including carbon monoxide, carbon dioxide, and methyl radicals. These fragments can later be removed with a methyl isobutyl ketone based developer. Recreated from Ref. [62].

methyl isobutyl ketone (MIBK)-based developer. However, a certain number of electrons per area (measured in charge per exposed area, C/cm^2) is required to effectively cleave a majority of the polymer chains, allowing MIBK to rid the exposed area of all PMMA. In general, a 150 nm thin film of PMMA 950k with a conductive coating on top requires doses between $160 \mu\text{C}/\text{cm}^2$ and $220 \mu\text{C}/\text{cm}^2$ for development. To ensure an excellent geometric quality of the nanostructures, dose tests with 0.8 to 2 times the nominal quantity are performed for each geometry to find the correct dose to clear the resist but not to overexpose it. The overexpose leads to a widening and modification of the developed geometry compared to the intended geometry, as shown in Figure 12a [62]. However, this so-called proximity effect is highly dependent on the geometry of the individual elements and the unit cell size of the metasurface, which makes it impossible to give a universal value for the nominal dose. In addition, applying a conductive coating often reduces the resolution of the resist because the scattering of electrons in the conductive coating increases and small details become blurred. Usually this effect cannot be compensated by adjusting the total dose across the Metasurface, and the geometry or dose of the individual nanostructures must be modified [62].

To understand possible compensation techniques to realize the desired nanostructure design, one needs to understand the proximity effect: An electron beam scans along a path specified by the desired geometry in electron beam lithography. However, the electron-electron interaction within the electron beam or the electron-atom interaction between the beam and the sample results in a broadening of the incident electron beam as it passes through the resist and the substrate (forward scattering) [62, 63]. Therefore, the resist is exposed in a larger area

than desired. Furthermore, the resist is additionally exposed when the electrons backscattered from the substrate bounce back into the resist. The strength of these scattering processes depends on the material and the angle of incidence of the electron beam. Consequently, the dose delivered by the electron beam is not confined to the geometry, which leads to an enlarging and blurring of geometrical features in a nanostructure. In the presence of a conductive top layer, the scattering is amplified since the electrons penetrate through the conductive layer into the resist and then into the substrate, resulting in an increased scattering [62]. (Note that the conductive coating results in a reduction of the nominal dose compared to other resist substrate systems too. For example, a 150 nm thin film of PMMA 950k on an indium tin oxide (ITO) coated substrate requires a dose of $220 \mu\text{C}/\text{cm}^2$ to $300 \mu\text{C}/\text{cm}^2$ for development.)

Two techniques can compensate for the electron scattering and proximity effect. First, the geometry, or second, the dose within the nanostructure, can be adjusted to reduce the exposure of some unwanted regions in the resist. Note that resolution can be improved by using thinner resists, but the resist thickness is limited if a subsequent lift-off is performed. In practice, the resist must be thicker than 120 nm (around three to five times the thickness of the deposited layer) to achieve good lift-off results [63].

For the first technique, the geometry of the nanostructure itself can be optimized to reduce overexposure. In the simplest case, the geometry can be made smaller to account for overexposure, but more complicated geometries require more sophisticated modification. We illustrate this technique using nanocrosses as an example, as shown in Figure 12a and b. As can be seen from the initial tests of a metasurface with nanocrosses, the edges of the fabricated nanostructures are slightly underexposed, resulting in convex rounding of the nanostructure. At the same time, the corners are overexposed, resulting in concave rounding. We added or subtracted small rectangles at each edge and corner to account for this geometry change, as shown in 3b. The size of these rectangles is about 10 nm, which is comparable to the minimum resolution of the PMMA resist [61]. Adding a rectangle to the edge of a nanostructure increases the dose in this area slightly, while subtracting a small rectangle from a corner decreases the dose in this area. The overall shape of the nanostructure is not heavily affected since the size of the added or subtracted rectangles is close to the minimum

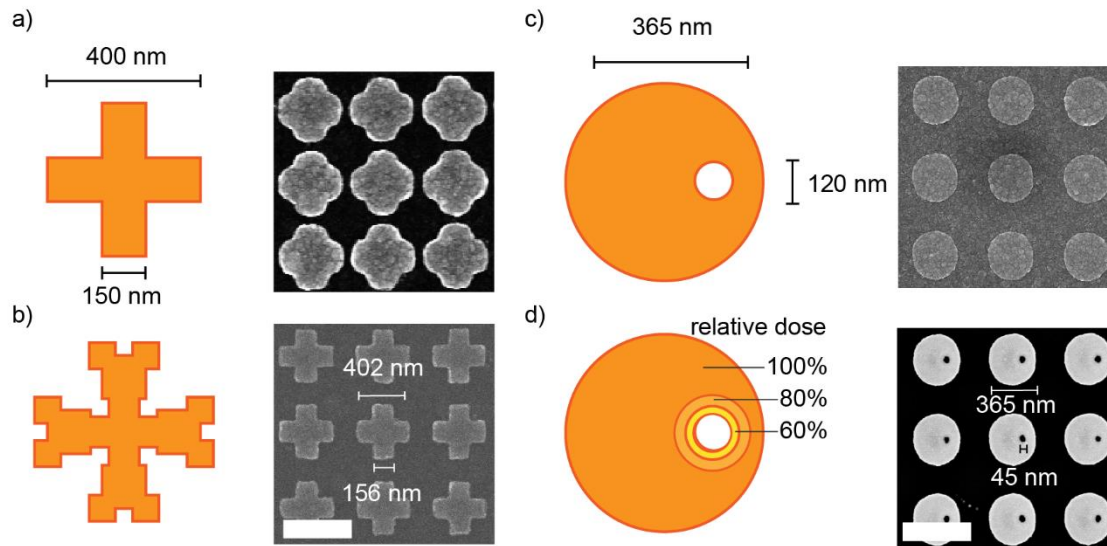


Figure 12. An unmodified a) and modified b) design of nanocrosses in metasurfaces as written with EBL and the physical realization after lifting off the Cr mask. An unmodified c) cylinder with hole and a dose modified cylinder d) with a hole as written and its physical realization. Scalebar 450 nm (a, b).

resolution of EBL system and the used resist. The drawback of this method is that some areas of a nanostructure may not be suitable for modification because they are too small, or the modification would obscure other features. Additionally, a particular feature's overall size/diameter can also be adjusted to compensate for the widening. 3a,b shows an example of a nanostructure before and after geometry modification. After the modification, the overall geometry written on the sample is greatly improved. The images show nanocrosses as an example; however, this optimization method can also be used for other geometries. In contrast to adjusting the geometry, the dose can also be adjusted across a single nanostructure. Here, the dose can be increased or decreased in some areas of a nanostructure so that the resist outside the desired area is exposed as little as possible. The disadvantage is that often the dose must be reduced to a value close to or below the critical dose of the resist to avoid overexposure. After developing the resist, PMMA residues may remain in the underexposed areas, causing problems during lift-off. Figure 12c,d shows an example of a structure where the dose is varied within the design to reduce the proximity effect. Here, the dose is reduced from 1 to 0.8 to 0.6 of the nominal dose in two concentric circles around the hole. In a final step, the nominal dose is varied to find the optimum value so that the hole is free of PMMA after development. Without correction, the off-center hole of the cylinder is no longer present in the nanostructure after lift-off. However, after correcting the dose around the hole, the feature is written correctly. Note that the structure shown in Figure 12c and d is an example of how it is not enough to correct the geometry sometimes, since increasing the size of the inner hole would cause the cylinder to intersect with the outside, resulting in

crescent-shaped structures. Note that geometry modification is highly used in optical lithography to improve the shape quality of written structures, since it is easy to change the geometry of a lithography mask. On the other hand, dose modification is mainly used in EBL because the dose can be easily controlled by the time the electron beam dwells on a point.

After writing the desired structures, the resist is developed. First, the conductive top-coating is removed in a water bath for 15 seconds. Then the sample is placed into a solution of 1:3 MIBK:IPA for 90 seconds (for 150 nm to 160 nm resist thickness), which is cooled to around 5°C before the development to increase the contrast of the resist. The sample is then placed in an IPA bath for 1 minute to stop the development. The sample is then rinsed with IPA.

3.4 Etch mask deposition and lift-off

The etch mask was deposited by an electron beam evaporator. In this process, an electron beam heats Cr granules to evaporate them in a vacuum (typically 10^{-6} mbar). The evaporated Cr is deposited on the sample at a rate of 0.1 nm/s, measured with a quartz crystal monitor. Typical film thicknesses range from 11 nm to 30 nm, depending on the thickness of the resist, since the thickness of the resist must be 3-5 times that of the Cr mask to achieve good lift-off results. On the other hand, the subsequent step of reactive ion etching also requires a certain thickness of the Cr mask since the mask erodes during etching. Then, the excess Cr is removed by dissolving the resist in acetone at a temperature of 70°C for 1 hour and subsequent cleaning in a dimethyl succinate solution at 85°C for another one hour, followed by ultrasonication to remove the residual Cr and to ensure a good lift-off result. At the end, only the nanostructures written by EBL remain on the silicon.

3.5 Reactive ion etching and Cr removal

The lithographically defined pattern is then transferred into the amorphous silicon using a reactive ion etching (RIE) process. The amorphous silicon is etched by an inductively coupled (ICP)-RIE process, commonly used in semiconductor manufacturing. In this step we want to achieve a good transfer of the Cr mask into the Si with vertical sidewalls. To achieve this anisotropic etching, the RF powers, gas flow rates of each chemical, and chamber pressure of the plasma system must first be optimized [64, 65]. Here, a 900 W ICP source creates a high-density plasma through a conductive coil (the inductive element). Another 41 W RF source in a parallel plate arrangement then accelerates the plasma onto the sample. Further to achieve anisotropic etching, the chamber pressure should be low to increase the mean free path of the ions and radicals in the plasma, here the pressure was 10 mTorr. The gas mixture inside the chamber was SF_6 and C_4F_8 with flow rates of 18 sccm and 45 sccm, respectively. In this process the radicals and fluorinated ions originating from the SF_6 etch the silicon. During the

etching process the silicon reacts with the fluorine to form SiF_4 , which is volatile under the chamber conditions and can be pumped out of the chamber. The C_4F_8 leads to passivation of the silicon surface, as the ring-shaped C_4F_8 molecule decomposes to CF_2 , which forms a protective polymer on the silicon surface. Here, the ratio of SF_6 and C_4F_8 is almost 1:3 which is advantageous for anisotropic etching [64, 65]. The combined effect of etching and passivation results in vertical sidewalls and good pattern transfer from the Cr into the silicon, as shown in Figure 13a. Another typical etching result can be seen in Figure 13b. Here one can see a cylinder with a hole after etching and after cutting the structure by focused ion beam. One can see that the hole is etched almost to the substrate. However, the etch rate for small holes is lower than the etch rate around the nanostructure due to the lower ion and radical concentration that can enter the hole. This effect is called aspect-ratio dependent etching (ARDE).

Nevertheless, good pattern transfer is achieved because the Cr mask is less affected by the etching process and erodes more slowly than the silicon during the etching process. Typically, at least 25 nm of Cr are needed to etch 1 μm of Si, resulting in an effective selectivity of around 40 between silicon and Cr during RIE. The erosion is mainly driven by physical etching by ion bombardment. For this reason, selectivity depends on the RF power used during etching. The area around the mask that is not protected by Cr is etched, while the silicon under the Cr mask is protected. After etching, the Cr mask is removed in a bath of Cr remover (Cr etch solution #1, containing perchloric acid and ammonium nitrate) diluted with water at a concentration of 80/20. Due to the dilution, the solution has a lower etch rate of 20 nm/min compared to the undiluted solution, which has an etch rate of 60 nm/min but makes it easier to control the etching process. The sample is then placed in a 90°C water bath to remove the etching solution. In the final step, the water is evaporated from the sample placed on a hot plate at 90°C, as dry blowing tends to remove the etched nanostructures.

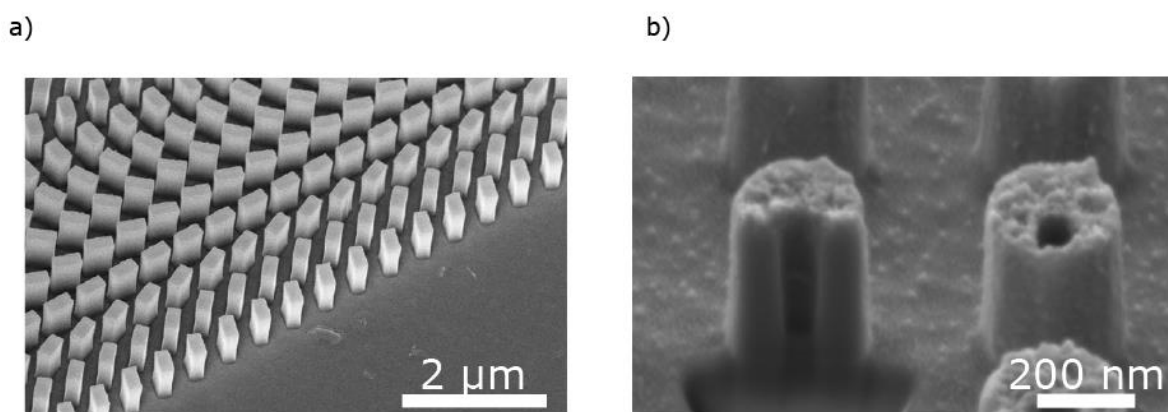


Figure 13. a) SEM image of amorphous Si nanostructures in metasurface after etching and b) magnified image of a Si nanostructure after cutting it by a focused ion beam (FIB) milling process.

Chapter 4 The propagation of light and nonlinear beam shaping with dielectric metasurfaces

Chapter 2 dealt with the linear and nonlinear responses of silicon resonators. Here it is shown that THG can be drastically improved by exploiting the natural magnetic resonances which occur in these systems. However, many applications require not only the efficient generation of light at the higher harmonic, but also the shaping of the wavefront of the generated light to realize certain operations or functionalities. For example, to direct the generated light at an angle to another optical element or to focus it. These functionalities can be realized with metasurfaces that generate a specific field $E_M(x, y, z_M)$ at the metasurface at the third harmonic such that after propagation through an optical system, the generated light behaves in a specific way that reflects the desired functionality. However, there are three possibilities on how one can construct an optical field $E_M(x, y, z_M)$ for beam shaping. In general $E_M(x, y, z_M)$ is a complex number and it has two parameters that can be spatially controlled: The amplitude $A(x, y, z_M)$ and phase $\phi(x, y, z_M)$ [66, 67]:

$$E_M(x, y, z_M) = A(x, y, z_M)e^{i\phi(x, y, z_M)}$$

49

Therefore, one can use a metasurface and spatially change the intensity, phase, or both of the generated light to affect propagation in a particular way. However, in many cases, a desired functionality can be encoded only by the spatial phase profile $\phi(x, y, z_M)$, and we only need to spatially vary the phase of the generated light. Note that this approach also works for linear metasurfaces and in classical optics: For example, a lens is an optical element that does not spatially change the amplitude of light passing through it, but introduces a spatially dependent phase delay caused by the propagation of light through glass of different thicknesses [67].

The next step in encoding a particular functionality in a dielectric metasurface is to find a set of nanostructures that will produce the desired phase delay when arranged in an array. Note that there are several ways to introduce a phase delay through a metasurface, as explained later. These nanostructures are then arranged in a metasurface according to the desired phase profile, as illustrated in Figure 14. Here one can see a simple example of a phase profile and how it could be encoded in a metasurface with a specific period p . First, the wavefront needs to be folded in the interval of 0 to 2π . Afterwards, the phase profile is sampled in steps of the period p to encode it into a metasurface. For the physical implementation, one needs to find a scheme or set of nanostructures that allow the required phase shift in each unit cell. However, to realize efficient wavefront shaping, we have three requirements for the elements of the metasurface [68]: First, one needs to cover the entire phase range (at least 2π), and the desired phase delay of a given structure should not be changed by the surrounding elements,

i.e., the nanostructures should be considered as independent scatterers. Second, the intensity of the generated third harmonic field should not change from element to element since one wants to encode only the phase. Third, the amplitude of the scattered or generated light should not change from element to element to achieve substantial interference. Fourth, since a metasurface can only sample a continuous phase profile in discrete steps, as indicated in Figure 14b, the unit cell size should be small enough to allow the best possible sampling rate of the phase profile. The unit cell size should be smaller than the operating wavelength in the

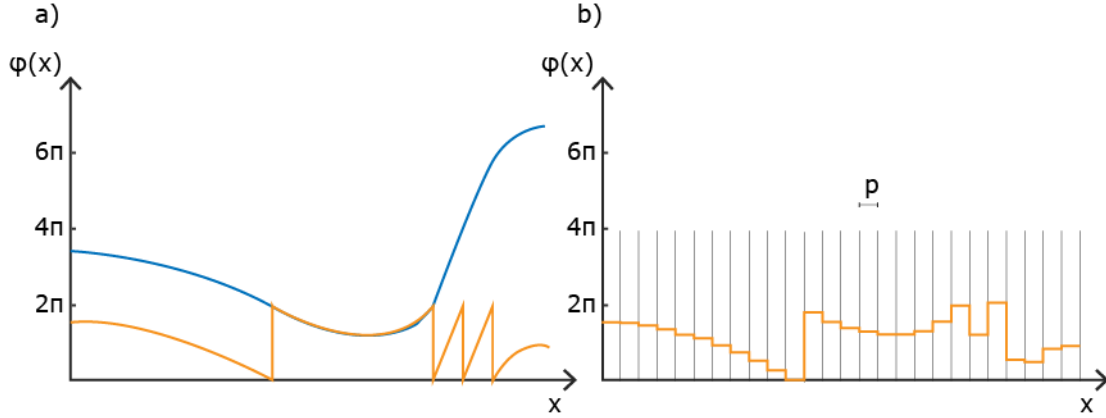


Figure 14. a) The blue curve represents an intended spatial phase profile. The orange curve represents the phase profile of the blue curve folded into the phase range from 0 to 2π b) A metasurface with a period p which encodes the spatial phase profile. Due to the discrete sampling the phase profile can be different to the original one.

best case. However, the first and last requirements are in conflict. One would prefer fine sampling of the spatial phase profile, but fine sampling reduces the unit cell size of the metasurface and leads to coupling effects between nearby elements that change the phase delay of the elements. This effect has already been studied in the linear regime (see Ref. [69]), but becomes even stronger in the nonlinear regime, since nonlinear optical systems are susceptible to small changes in geometry that negatively affect the diffraction efficiency of the metasurface. Therefore, finding a good trade-off between these constraints is the main task of metasurface design. In addition, dielectric resonators have a size issue in view of nonlinear optics, where magnetic Mie resonances are often used to enhance the nonlinear conversion process. However, in the case of a magnetic dipole resonance, the size D of a nanoparticle and the resonance wavelength λ_{res} are related by $D \approx \frac{\lambda_{res}}{n}$ [70], where n denotes the refractive index of the nanoparticle. Therefore, the unit cell size of a metasurface is often larger than the TH wavelength itself, which can lead to diffraction and scattering of the generated light by the lattice. For these reasons, it is always challenging to realize an efficient wavefront-shaping metasurfaces in the nonlinear domain.

4.1 Resonant wavefront shaping: The Huygens Principle

In principle, two physical mechanisms can be used in nanostructures to achieve phase delay to shape light in the nonlinear domain and to design elements with the desired phase delay—the resonant (Huygens approach) and the geometric phase approach [71]. The first approach involves a resonant nanostructure in which the generated field at the higher harmonic frequency has a phase delay to the incident field. This approach can be understood if the nanostructure is viewed as a driven oscillator. Here, by slightly changing the geometry of the nanostructure, the resonance wavelength can be tuned. However, since the design wavelength is fixed, the resonator has a fixed phase relation at the design wavelength with respect to the resonance frequency. Consequently, the higher harmonic light is also generated with a particular phase delay with respect to the design wavelength. Therefore, by tuning a resonance around a specific wavelength, it is possible to create a range of nanostructures covering the whole phase range. Note that the resonant approach only allows a phase range of 0 to π , to reach the complete phase range of 0 to 2π the geometry of each nanostructure is to be rotated by 90° . This approach was first introduced by Pfeiffer and Grbic [72] for resonant beamforming in the linear domain. The development of a set of nanostructures usually requires a full-wave simulation due to the complexity of the problem. The simulation process is similar to the one described in Chapter 2. However, the structure geometries are optimized numerically with respect to the desired phase and amplitude at the desired wavelength of the higher harmonics, which are specified as optimization objectives. An example of such a nonlinear Huygens metasurface was realized by Wang et al. [17]. Here, an amorphous silicon metasurface was used for resonant wavefront shaping at the third harmonic by exploiting the magnetic and electric resonances of elliptical nanostructures. The geometry of each silicon pillar was modified to achieve a specific phase response due to the resonance shift, as can be seen in Figure 15a.

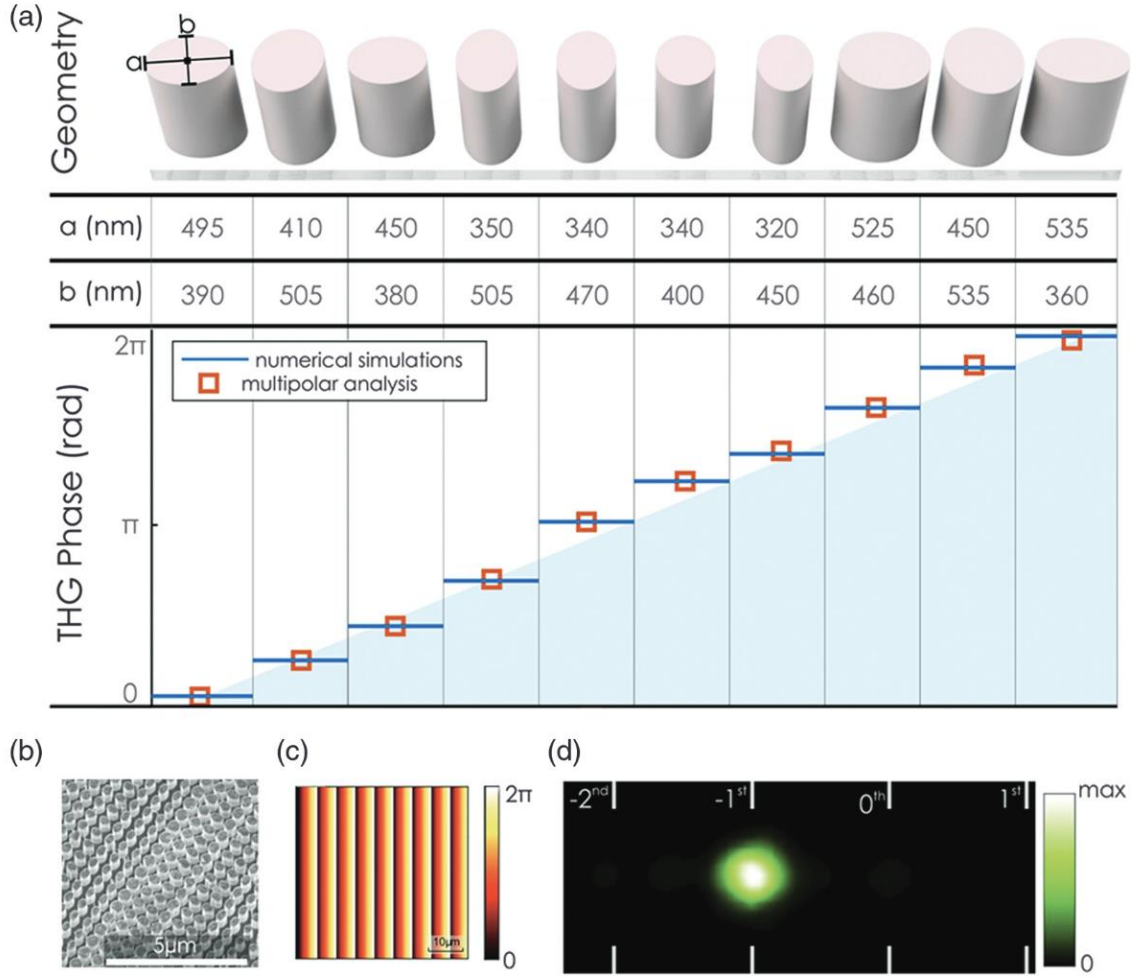


Figure 15. a) Geometries and nonlinear phases of Si nanostructures. The geometric parameters of the nanopillars and the corresponding analytical and numerical results for the phase of the third-harmonic field at a pump wavelength of 1615 nm (538 nm TH wavelength) and linear polarization of the pump along the x-axis. B) SEM image of the silicon metasurface. C) Phase profile to reconstruct a blazed grating at the third harmonic wavelength encoded into the metasurface shown in b). d) Fourier space image of the THG signal in forward direction. The diffraction efficiencies is 92%, that is 92% of the THG is directed into the designed diffraction angle of 5.6° [17].

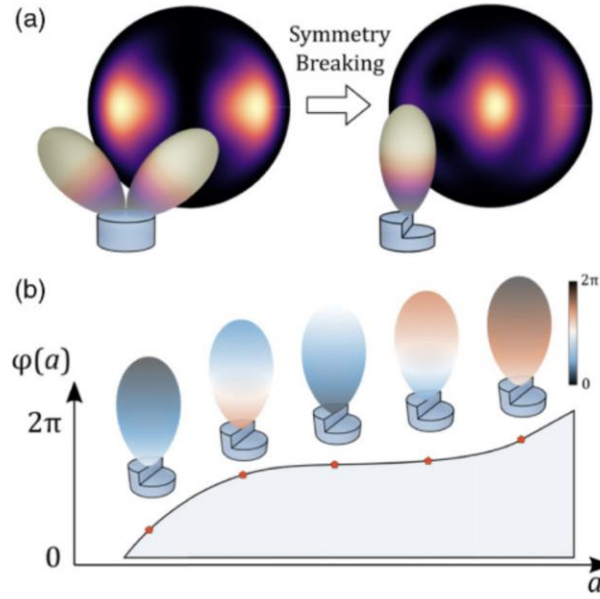


Figure 16. a) Evolution of the second harmonic directionality from the case of a nanocylinder (two lobes, left) to a nanochair (one vertical lobe, right): schematic representation and numerically calculated patterns in the Fourier plane. B) Selection of a set of nanochairs based on the relationship between a given geometric parameter a and the far-field SHG phase $\varphi(a)$ [58].

At the same time, the amplitude of the THG signal was kept constant as a constraint for the design. With this approach, it is possible to encode different wavefront phase profiles into the harmonic generation process by arranging the different elliptic cylinders in a Metasurface, as illustrated in Figure 15b. For example, one can realize a sawtooth phase profile, which deflects the generated light under an angle of 5.6° (Figure 15c,d). With this approach, they achieved high nonlinear conversion efficiencies due to exploiting a resonant system as well as high diffraction efficiencies of over 90%. Further, this approach allows for more complex applications like nonlinear imaging, where an object is illuminated with the fundamental wavelength and is then imaged at the third harmonic light [73]. Another work with a similar approach for nonlinear holography with silicon metasurfaces can be found by Gao et al. [16].

Further, wavefront shaping can be achieved for second harmonic generation (SHG) in [100]-AlGaAs. However, due to the zinc-blende crystal structure of AlGaAs, the second harmonic (SH) generation is directed at an angle of about 45° [74] [58, 75] for [100]-AlGaAs, as illustrated in Figure 16a. Note that by changing the crystal orientation of AlGaAs from [100] to [111] SHG can be generated parallel to the pump beam [74]. Therefore, AlGaAs nanostructures for wavefront shaping must be designed not only with respect to the phase and amplitude of the SHG but also to the direction of the SH light [58]. To achieve this, the design utilizes a complex three-dimensional structure to shape the directionality of the SH light, as illustrated in Figure 16b. By changing the geometry to the nanochair, one can adjust the phase of the generated

light at the second harmonic. However, the diffraction efficiency remains low due to the difficult constraints on directionality mentioned above. Here, the diffraction efficiency is around 45% for the SH beam at the SH wavelength of 775 nm (fundamental wavelength of 1550 nm), which is due to the large period of the unit cell ($p = 900$ nm) [58]. Overall, the resonant approach to wavefront shaping enables phase design in the generation of higher harmonics and subsequent encoding of an arbitrary wavefront with a set of nanostructures with high nonlinear conversion efficiency since the nanostructures can be resonant and since dielectrics have significant nonlinear coefficients. As the optical coupling between nanostructures is implicitly controlled in the simulations (if the geometric parameters of the metasurface do not change drastically from unit cell to unit cell), the diffraction efficiency can also be high. However, the drawback of this approach is the large computational effort required to create a library of nanostructures for fine-grained phase control with constant amplitude in the nonlinear domain.

4.2 Geometric Phase Principle

The second approach to phase engineering with metasurfaces is the so-called Pancharatnam-Berry or geometric phase approach. Here, the phase change in the nonlinear generation process can be controlled by the rotation of a single nanostructure in an array when the metasurface is pumped by circularly polarized light. It is known from plasmonics that rotating a nanostructure by an angle θ can cause a phase shift between the circularly polarized light incident on the nanostructure and the higher harmonic generated light. In this case, the order n of the nonlinear process influences the nonlinear phase delay, and the phase changes with it [8]:

$$P(\sigma, \theta) \propto e^{i(n \pm 1)\sigma\theta}$$

50

Where $\sigma = \pm 1$ denotes the circular polarization state of the fundamental pump light, incident on the nanostructures. The exponent $i(n \pm 1)\sigma\theta$ represents the nonlinear Pancharatnam Berry phase factor accumulated during the nonlinear conversion process. The phase factor depends only on the rotation angle of the nanostructure with a specific (m -fold) rotational symmetry. In addition, ± 1 indicates whether the phase is accumulated in the same polarization (+1) compared to the fundamental beam (called co-polarization) or in the opposite polarization state (-1, called cross-polarization). For example, a structure with twofold rotational symmetry leads to phase factors of $\pm 2\theta$ for co-polarization and $\pm 4\theta$ for cross-polarization. The first part of this work addresses the question of whether such a nonlinear geometric phase metasurface design is feasible for purely dielectric metasurfaces. Considering the phase control requirements discussed at the beginning of this chapter, the

geometric phase approach allows fine-grained phase control since the phase can be continuously adjusted by rotating the nanostructure. In addition, the amplitude of the nonlinearly generated light remains constant by design since only a single nanostructure design is required. Compared to the nonlinear extension of the Huygens principle, the computational cost is low because only a single nanostructure needs to be optimized for high nonlinear conversion and diffraction efficiency. Thus, two of the three requirements are fulfilled in a simple way. However, in view of nonlinear phase manipulation, several questions remain: First, does the tensorial nature of amorphous silicon lead to similar problems as in the SHG from [100] AlGaAs? Second, cell-to-cell rotation strongly modifies the coupling between nanostructures due to the larger three-dimensional extent compared to plasmonic nanostructures. Compared to plasmonic resonators, dielectric resonators are larger. Therefore, the density of dielectric nanoresonators is higher and the distance between them is smaller compared to their plasmonic counterparts. This can have a more negative effect on nonlinear phase control than in the plasmonic case, since the distance between adjacent dielectric nanostructures must be smaller than that of plasmonic nanostructures. This in turn, leads to near-field coupling effects on the phase and amplitude of the emitted TH light. For these reasons, we have investigated TH phase control in amorphous silicon metasurfaces governed by the geometric phase principle. We show experimental evidence that the nonlinear PB phase principle can be extended to all-dielectric metasurfaces under circularly polarized light and can be used in holography or beam steering. Moreover, magnetic Mie resonances are often used to enhance the nonlinear conversion process.

In the first part of this chapter, we explain the geometric phase principle using nanostructures with C2 rotational symmetry as an example, as shown in Figure 17. We derive the geometric phase principle and show the experimental implementation and different outcomes with nonlinear generation and phase manipulation. We also show that it is possible to encode holograms in nonlinear generation using the geometric phase principle. Later, we explain the geometric phase principle for different rotational symmetries.

4.3 Derivation of the PB phase for THG

Consider an electromagnetic wave traveling along the z-axis through a metasurface extending in the x-y plane, as illustrated in Figure 17 with the example of a nanofin. The nanostructures are rotated along the z-axis by an angle θ , as shown in the figure. In the case of plasmonic

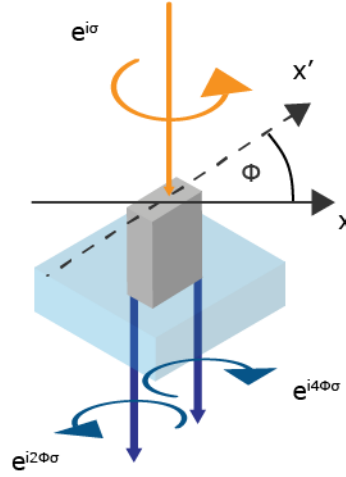


Figure 17. Schematic illustration of the generation of third harmonic light with antenna's rotation. Upon rotation the generated nonlinear signal gains phases of $\vartheta_{co} = 2\sigma\phi$ and $\vartheta_{cross} = 4\sigma\phi$ in co- and cross-polarization states, respectively [60].

particles, the rotation introduces a geometric phase in the harmonic generation process according to equation 50. However, the nanostructures are assumed to be approximated as 2D objects in a plane due to the short propagation distances. In contrast, dielectric resonators are up to 10 to 20 times thicker than their plasmonic counterparts, and the nonlinearly generated signal builds up through the total radiation of the induced nonlinear polarization in the volume, making wave coupling and propagation effects striking. Therefore, instead of approximating the electromagnetic response of the system in the 2d plane of the surface, we need to calculate an effective third-order susceptibility $\chi_{ijkl}^{(3)eff}$, which describes the nonlinear susceptibility of the whole nanostructure. To calculate the effective susceptibility, one must resort to numerical investigations, since one has to calculate the spatial overlap integral between the electromagnetic near fields present in the nanostructure at ω and 3ω in response to the incident fields and the outgoing field at the TH frequency [76–79]. Usually this is done by simulating the nanostructure at the fundamental and third harmonic wavelength with an excitation $\vec{E}_{i,inc}^\omega$ and $\vec{E}_{i,inc}^{3\omega}$:

$$\chi_{ijkl}^{(3)eff} = \sum_{a,b,c,d \in \{x,y,z\}} \chi_{abcd,si}^{(3)} \frac{\int (\vec{E}_{a,i}^{3\omega})^* \vec{E}_{b,j}^\omega \vec{E}_{c,k}^\omega \vec{E}_{d,l}^\omega dV}{\vec{E}_{j,inc}^\omega \vec{E}_{k,inc}^\omega \vec{E}_{l,inc}^\omega \vec{E}_{i,inc}^{3\omega} V_{unit}}$$

51

Here $\vec{E}_{a,i}^{3\omega}$ denotes the local electrical field component of the electric near field in Cartesian coordinates at frequency 3ω and when the structure is excited with an electromagnetic field at the third harmonic frequency. The local electric fields of the electric near field at frequency ω are denoted by $\vec{E}_{b,j}^\omega$, $\vec{E}_{c,k}^\omega$ and $\vec{E}_{d,l}^\omega$ when excited with an pump field at the fundamental

frequency. The star indicates the complex conjugate because the electric field at the third harmonic is radiated, but in numerical simulations the structure is often excited by a wave which leads to a time reversal in the equation. The indices a, b, c, d, i, j, k, and l refer to the Cartesian coordinates x, y, and z, respectively, and describe the polarization of the incident light at both frequencies. Moreover, $\chi_{abcd, Si}^{(3)}$ is the intrinsic third order nonlinear response of silicon and V_{unit} is the volume of the resonator. This effective third-order susceptibility $\chi^{(3)eff}$ with its components $\chi_{ijkl}^{(3)eff}$ relates the third-order response of a dielectric nanostructure to the fundamental light field and contemplates the symmetry of the structure. Therefore, it can be used to describe the nonlinear geometric phase response of a dielectric nanostructure. To study the geometric phase in response to the rotation of a nanostructure, it is helpful to switch from a Cartesian to a circular polarization basis in the x-y-plane $\{\vec{e}_L, \vec{e}_R, \vec{e}'_z\}$. In the circular basis, the unit vectors are given in terms of the Cartesian Basis $\{\vec{e}_x, \vec{e}_y, \vec{e}_z\}$ as follows [79]:

$$\vec{e}_L = \frac{1}{\sqrt{2}}(\vec{e}_x + i\vec{e}_y)$$

$$\vec{e}_R = \frac{1}{\sqrt{2}}(\vec{e}_x - i\vec{e}_y)$$

$$\vec{e}'_z = \vec{e}_z$$

52

Moreover, the transformation matrix of the unit vectors is therefore as follows:

$$\begin{pmatrix} \vec{e}_L \\ \vec{e}_R \\ \vec{e}_z \end{pmatrix} = \frac{1}{\sqrt{2}} \begin{pmatrix} 1 & i & 0 \\ 1 & -i & 0 \\ 0 & 0 & \sqrt{2} \end{pmatrix} \begin{pmatrix} \vec{e}_x \\ \vec{e}_y \\ \vec{e}_z \end{pmatrix}$$

$$\begin{pmatrix} \vec{e}_x \\ \vec{e}_y \\ \vec{e}_z \end{pmatrix} = \frac{1}{\sqrt{2}} \begin{pmatrix} 1 & 1 & 0 \\ i & -i & 0 \\ 0 & 0 & \sqrt{2} \end{pmatrix} \begin{pmatrix} \vec{e}_L \\ \vec{e}_R \\ \vec{e}_z \end{pmatrix}$$

53

Note that the z-axis remains unchanged since we are interested in the phase response in the x-y plane, and rotation about the x- or y-axis instead of the z-axis is not possible. Therefore, the effective third-order susceptibility in circular coordinates is given by a coordinate transformation [79]:

$$\chi_{\alpha\beta\gamma\delta}^{(3)eff} = \sum_{i,j,k,l} \chi_{ijkl}^{(3)eff} \Lambda_i^\alpha \Lambda_j^\beta \Lambda_k^\gamma \Lambda_l^\delta$$

54

55

Here, α, β, γ and δ refer to the circular coordinates R, L, and z. Λ_i^α is the element of the transformation matrix between the respective circular and cartesian basis vector in equation 53. When a nanostructure is rotated in the x-y plane of the metasurface, the nonlinear polarization differs from the unrotated nonlinear polarization in the laboratory frame by a phase factor that gives rise to the nonlinear geometric phase. In the case of counterclockwise rotation of the nano resonator by an angle θ , the effective nonlinear polarization is described as follows:

$$\chi_{\alpha'\beta'\gamma'\delta'}^{(3)eff} = \sum_{\alpha,\beta,\gamma,\delta} \chi_{\alpha\beta\gamma\delta}^{(3)eff} R_{\alpha}^{\alpha'} R_{\beta}^{\beta'} R_{\gamma}^{\gamma'} R_{\delta}^{\delta'} \quad 55$$

Here, the indices $\{\alpha', \beta', \gamma', \delta'\}$ refer to the rotated coordinate system and $R_{\alpha}^{\alpha'}$ are the elements of the rotation matrix for the rotation from α to α' . The total rotation matrices $R_{\alpha}^{\alpha'}$ and $R_{\alpha'}^{\alpha}$ in a circular basis is as follows:

$$R_{\alpha}^{\alpha'} = \begin{pmatrix} e^{i\theta} & 0 & 0 \\ 0 & e^{-i\theta} & 0 \\ 0 & 0 & 1 \end{pmatrix} \quad R_{\alpha'}^{\alpha} = \begin{pmatrix} e^{-i\theta} & 0 & 0 \\ 0 & e^{i\theta} & 0 \\ 0 & 0 & 1 \end{pmatrix} \quad 56$$

Together with the rotation matrix 56, the third-order nonlinear polarization, can be written as follows:

$$\begin{aligned} \vec{P}_{\alpha'}^{(3)eff}(\vec{r}) &= \sum_{\alpha} R_{\alpha}^{\alpha'} \vec{P}_{\alpha}(\vec{r}) = \epsilon_0 \sum_{\alpha,\beta,\gamma,\delta} R_{\alpha}^{\alpha'} \chi_{\alpha\beta\gamma\delta}^{(3)eff} \vec{E}^{\beta} \vec{E}^{\gamma} \vec{E}^{\delta} \\ &= \epsilon_0 \sum_{\beta',\gamma',\delta'} \sum_{\alpha,\beta,\gamma,\delta} R_{\alpha}^{\alpha'} \chi_{\alpha\beta\gamma\delta}^{(3)eff} R_{\beta}^{\beta'} R_{\gamma}^{\gamma'} R_{\delta}^{\delta'} \vec{E}^{\beta} \vec{E}^{\gamma} \vec{E}^{\delta} \end{aligned} \quad 57$$

The rotation matrix shown in equation 56 is a diagonal matrix, and therefore, the effective nonlinear susceptibility can be written as: $\chi_{\alpha'\beta'\gamma'\delta'}^{(3)eff} = \chi_{\alpha\beta\gamma\delta}^{(3)eff} R_{\alpha}^{\alpha'} R_{\beta}^{\beta'} R_{\gamma}^{\gamma'} R_{\delta}^{\delta'}$ and for a purely circular polarized fundamental excitation, one obtains:

$$\begin{aligned} P_L^{(3)eff} &= \epsilon_0 \left[\chi_{LLLL}^{(3)eff} (E^L)^3 e^{2i\theta} + \chi_{LRRR}^{(3)eff} (E^R)^3 e^{-4i\theta} \right] \\ P_R^{(3)eff} &= \epsilon_0 \left[\chi_{RRRR}^{(3)eff} (E^R)^3 e^{-2i\theta} + \chi_{RLLL}^{(3)eff} (E^L)^3 e^{4i\theta} \right] \end{aligned}$$

Here, $P_L^{(3)eff}$ and $P_R^{(3)eff}$ are the effective volume polarizations for left (L) and right (E) circularly polarized light and the rotation angle θ of the nanostructure. Note that the index combination LLLL and RRRR refer to polarization states, where fundamental electromagnetic wave and the THG wave have the same polarization (co-pol.), and the index combination LRRR and RLLL refers to the case where the fundamental wave and the THG wave have opposite handedness (cross-pol.). Equation 58 shows that the nonlinear generation process can carry the geometric phase of $e^{\pm 2i\theta}$ in co-polarization and $e^{\pm 4i\theta}$ in cross-polarization. The intensity of TH waves contributed by each nonlinear polarization term is determined by the magnitude of the effective nonlinear susceptibility and the field intensity of the fundamental electromagnetic fields.

4.4 Gradient design

Considering a periodic array of dielectric resonators where each resonator has a different rotation, each resonator emits TH light with a different phase, and depending on the rotation, we obtain constructive and destructive interference in the far-field. Figure 18 shows the spatial phase profile to encode a blazed grating and its physical realization as a metasurface

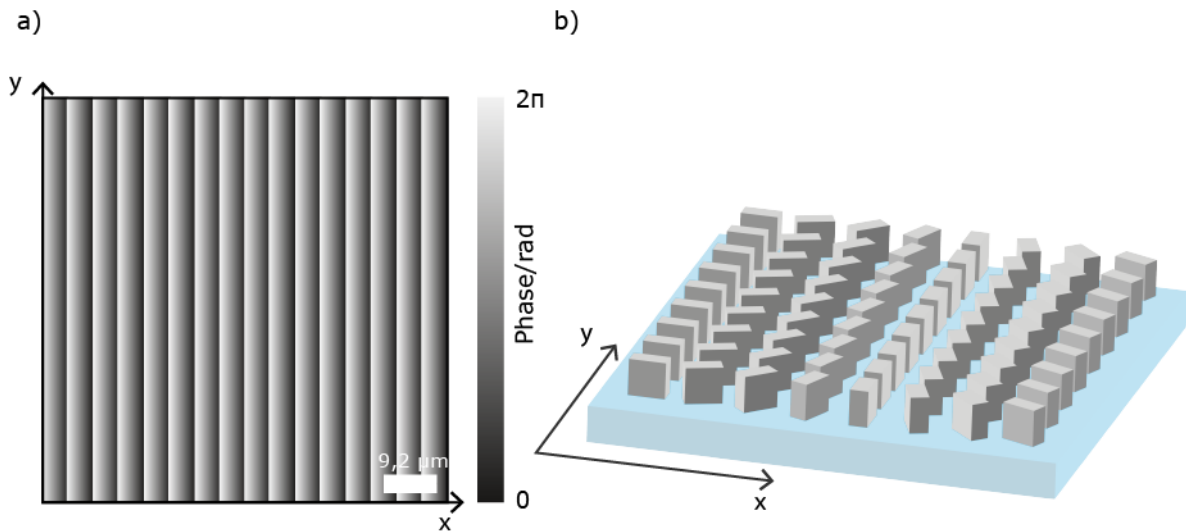


Figure 18. a) Sawtooth phase profile to realize a blazed grating (scale bar: $9.2 \mu\text{m}$) and b) realization of a gradient PB phase metasurface with the rotation of nanostructures.

where the nanostructures are rotated in the x-direction to encode the grating. Note that due to the discrete nature of the nanostructures, one can only sample the phase profile at discrete points, resulting in a step phase profile. Due to the phase accumulation across the blazed grating, the generated TH beam is deflected by an angle α_t . The relationship between the

accumulated phase and the deflection angle is given by the generalized law of anomalous refraction [80]:

$$\sin(\alpha_t) n_t - \sin(\theta_i) n_i = \frac{\lambda_{TH}}{2\pi} \frac{d\theta}{dx} + m \frac{\lambda_{TH}}{s}$$

59

Where α_t and α_i are the angles of the refracted and incident beams, respectively. n_t and n_i are the refractive indices of the material on the refracted beam side and on the incident beam side, respectively. λ_{TH} is the third harmonic wavelength and $d\theta/dx$ is the change in phase from one unit cell to the next unit cell per unit cell period. The last term $m \lambda_{TH}/s$ describes the grating equation and considers the diffraction at the unit cell itself, where m stands for the diffraction order and s for the period of the unit cell. This term is necessary because the unit cell in dielectric nanoresonators for THG is often larger than the third harmonic wavelength. However, in our case, we assume that the third harmonic is normally incident, refracted in air, and we consider the zero-diffraction order ($m = 0$) only. Therefore, the equation reduces to:

$$\sin(\alpha_t) = \frac{\lambda_{TH}}{2\pi} \frac{d\theta}{dx}$$

60

From this equation, it is possible to connect the phase change due to the rotation of the nanostructures to the deflection angle α_t of the TH beam.

4.5 The geometry of the unit cell and optical characterization

The nanoresonators in Figure 17 were designed to have a size of $400 \times 200 \times 650 \text{ nm}^3$ (LxWxH) with a unit cell size of $575 \times 575 \text{ nm}^2$ and were made of amorphous silicon fabricated as explained in the last chapter. The resonance of the nanoresonators is designed to be around 1215 nm (Figure 19a). The measured transmittance values (Figure 19b) in the near-infrared region show that the silicon resonators are in resonance at 1290 nm and has a linewidth of 100 nm , much broader compared to the simulations. We attribute the redshift and broadening compared to the simulation firstly to the imperfection of the nanofabrication and secondly to defects created by the RIE process. Reactive ion etching (RIE) can introduce defects into the

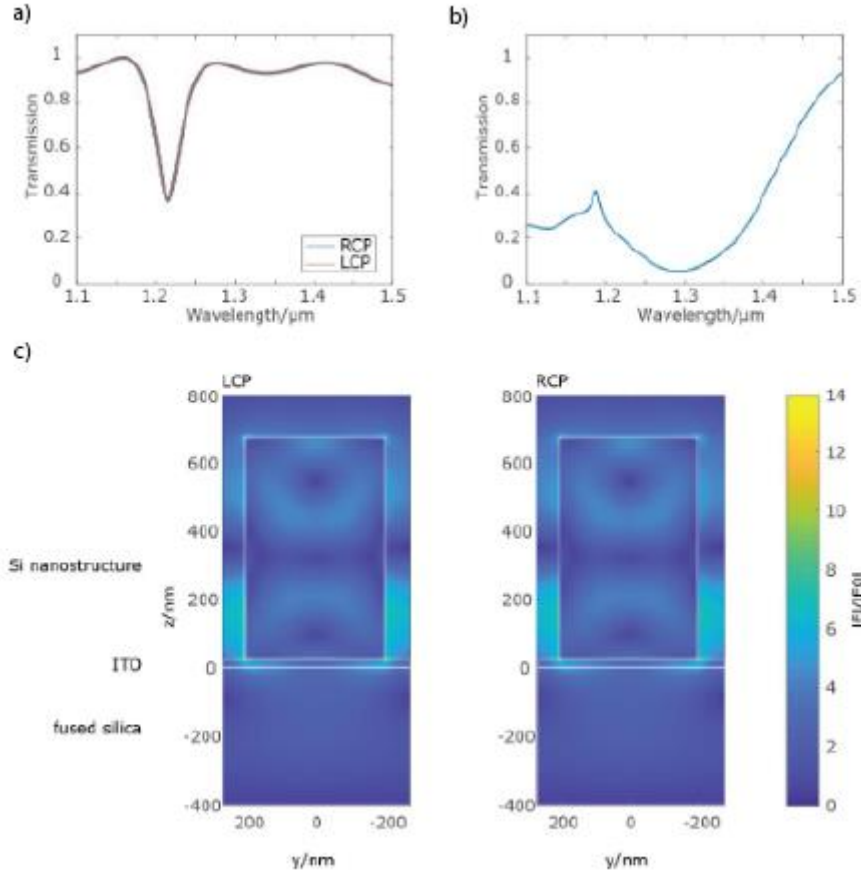


Figure 19. a) The transmission spectrum of the metasurface measured with an FTIR spectrometer. b) Calculated transmission spectra for left and right circular polarized light simulated with CST Microwave Studio. The nanostructures show a resonance at 1215 nm for both polarization states. c) Electrical near field plots inside the nanostructure at $x = 0$ nm [60].

nanostructures caused by high-energy ions and radicals. It is known that RIE leads to surface defects, forming surface states in Si nanofins that increase absorption [81]. Therefore, the refractive index of the nanostructures may differ from the refractive index of an unstructured film, which shifts the resonance wavelength. The electric near-field diagrams (Figure 19c) at the resonance frequency of 1215 nm show that the field within the structures is enhanced by a factor of 8. Moreover, the electric near-field diagrams and the transmittance values for left and right circularly polarized light show no differences since the structure itself and the electromagnetic field exhibit a mirror symmetry. Additionally, the electric field distribution shows a vortex in the electric field which is typical for a magnetic Mie resonance.

4.6 Nonlinear optical characterization by Fourier plane imaging

To investigate the nonlinear wavefront shaping properties of dielectric metasurfaces experimentally, we use a setup that can efficiently collect the generated light with a microscope objective and transmit it to a camera or spectrometer. However, to assess the wavefront shaping properties of this metasurface, it is convenient to image the back focal plane of the microscope objective than the image of the metasurface itself because the

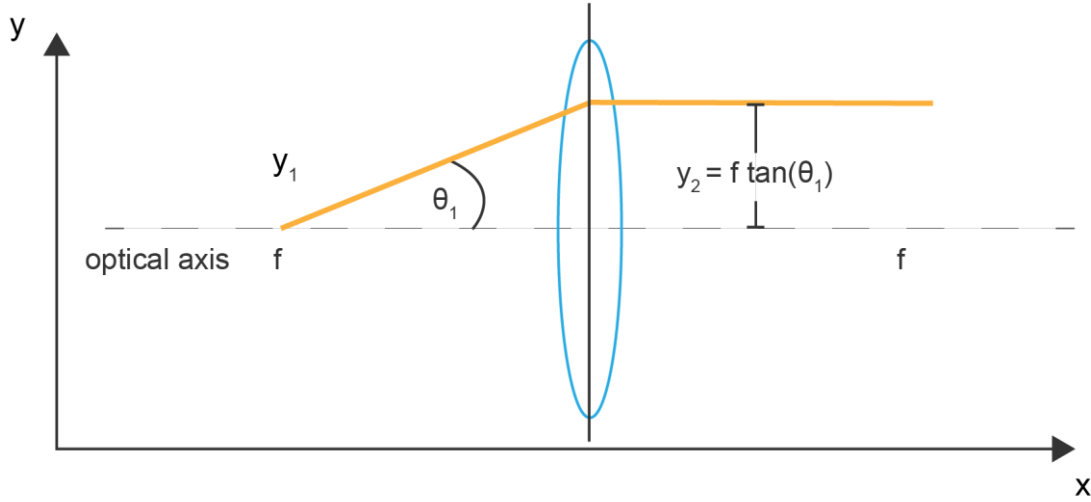


Figure 20. Scheme of Fourier imaging with a thin lens. The sample is placed at the focal point of the lens. Here, the light distribution in the rear focal plane of the lens is proportional to the angular spectrum of the light emitted by the sample.

Fourier plane contains direct information about the direction of the light. For example, consider a beam that starts at the focal point of a thin lens on the optical axis ($y_1 = 0$) at an angle θ_1 to the optical axis and propagates through the lens and then to the back focal plane of the lens, as shown in Figure 20. The lateral distance of the beam to the optical axis Δy after passing through the lens can be calculated by trigonometry. Figure 20 shows that the beam height at the back focal plane is $\Delta y = f \tan(\theta_1)$ and that the beam height is proportional to the angle of the beam in front of the lens. However, in terms of the experimental implementation, microscope objectives are often used for Fourier imaging setups. Here, the focal length of a microscope objective is often not specified and only the distance between the specimen and the first optical surface of the objective, the working distance W_{OB} , is known. In this case, the relationship between the lateral distance of a beam in the back focal plane and the deflection angle α is approximately given by [60]:

$$\alpha \approx \frac{\Delta x}{W_{OB}}$$

61

This equation can be used to measure the angle of deflection of a beam in the paraxial approximation if the beam height at the back focal plane and the working distance between the specimen and the objective are known. Note that the measurable angular range is limited by the numerical aperture (NA) that can be detected by the objective, since the numerical aperture and the maximum deflection angle α of the light are connected by [80]:

$$NA = n \sin (\alpha)$$

62

Where n is the refractive index of the medium in which the beam propagates. Further, note that converging lenses can perform a spatial Fourier transform as light propagates through them from the front $z = -f$ to the back focal plane $z = +f$. Therefore, the distribution of light in the Fourier plane is proportional to the spatial frequencies of the light which propagates through the lens. The pure scaled Fourier transform due to a lens can be written as follows [67, 68, 80]:

$$\Theta(x, y, -f) = \frac{i\lambda}{f} \int_{-\infty}^{\infty} \int_{-\infty}^{\infty} \exp \left(\frac{i2\pi}{\lambda f} (xx' + yy') \right) \Theta(x', y', +f) d\frac{x'}{\lambda} d\frac{y'}{\lambda}$$

63

Where $\Theta(x, y, z)$ is the optical field, which propagates through the lens. The Fourier transform property of lenses is extremely useful in both theory and application, as we will see in Chapter 4.9.

The complete setup to characterize the nonlinear signal of a metasurface is shown in Figure 21a. The metasurface is illuminated by a slightly focused circularly polarized laser beam at fundamental wavelengths between 1200 nm and 1350 nm. The laser source used in the experiments is an optical parametric oscillator (OPO) with a typical pulse length of 200 fs and 80 MHz repetition rate, synchronously pumped by a TiSa femtosecond laser (Coherent Chameleon). An infinity-corrected microscope objective with a numerical aperture of 0.6 (Nikon ELWD) collects the third harmonic light from the metasurface. To measure the angle of deflection of the frequency-converted light from the metasurface, we imaged the back focal plane of the microscope objective onto an sCMOS camera, since it contains information of the deflection angle as discussed above. Since both lenses behind the objective lens in the setup have the same focal length ($f=150$ mm), the imaging system must apply no additional magnification correction. Note that short pass filters block the fundamental beam. Using a

combination of a quarter-wave plate and a linear polarizer makes it possible to distinguish between generated light with the same (co-polarization) or opposite polarization (cross-polarization) compared to the incident fundamental pump light.

4.7 Nonlinear measurements

Figure 21b and c show the THG measurement results for the different co- and cross-polarization combinations for metasurfaces with and without a phase gradient at a fundamental wavelength of 1240 nm, respectively. Here, the resonators were rotated to resemble a blazed grating encoding a phase shift of 0 to 2π (co-polarization) and 0 to 4π (cross-polarization) in $4.6 \mu\text{m}$ with eight nanostructures. Therefore, the phase difference $d\theta$

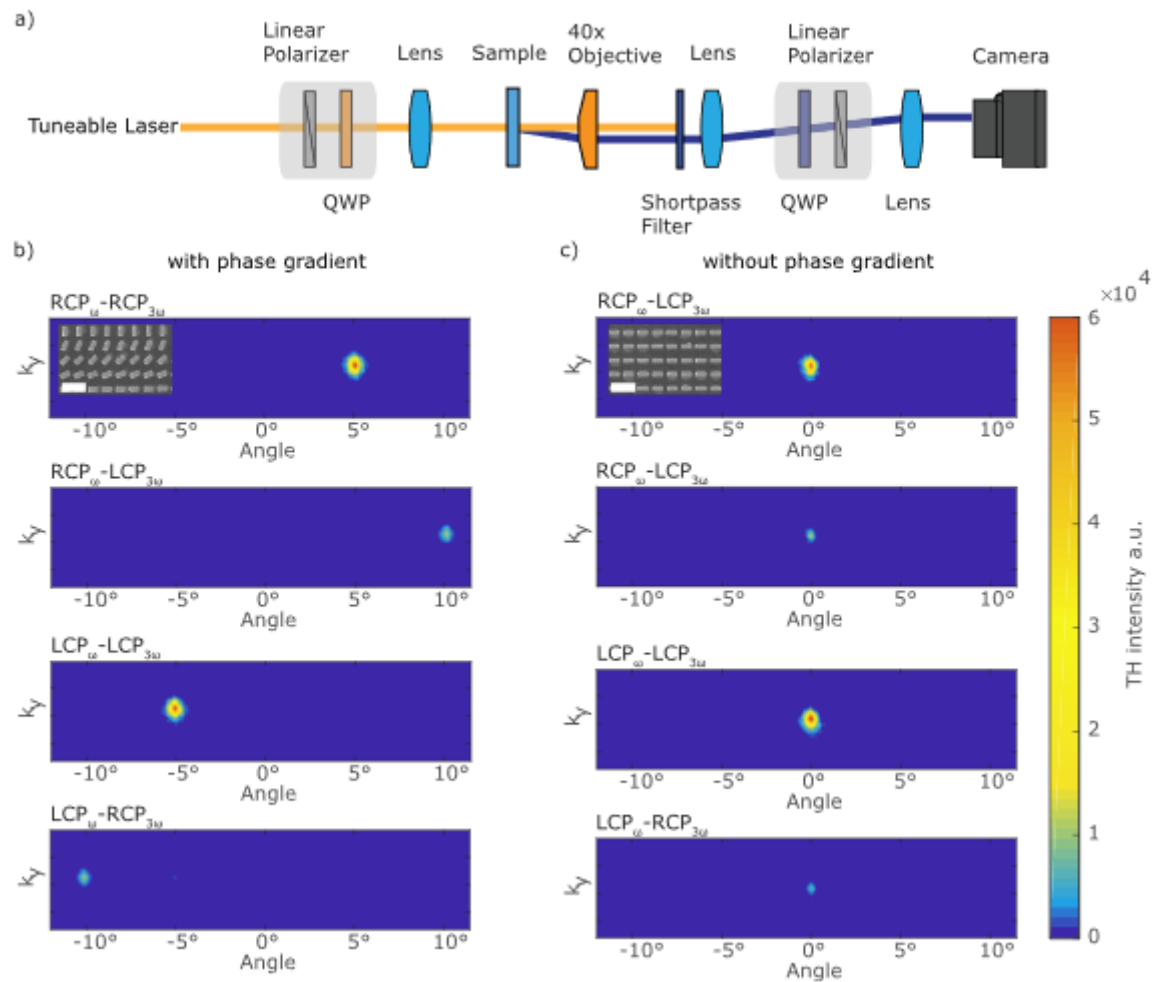


Figure 21. a) Schematic representation of the optical setup for the measurement of third harmonic (TH) light. The first combination of a linear polarizer and a quarter-wave plate (QWP) processes the circularly polarized fundamental input beam onto the metasurface. The second combination analyzes the THG output light. The lens in front of the sample focuses the light

onto the sample, while the lenses behind the objective lens image the back focal plane of the objective onto the CMOS camera. The THG light is collected by a 40×/NA 0.6 microscope objective. b) Third harmonic diffraction spots generated by the blazed grating metasurface. The THG signals are measured with different combinations of circularly polarized input and output light. The inset shows the top view of the corresponding metasurface. The scale is 1 μm (c) Third harmonic diffraction points for the metasurface without phase gradient for different combinations of circularly polarized input and output light. The inset shows the top view of the metasurface [60].

is $\pi/4$ in co-polarization and $\pi/2$ in cross-polarization. In total, this leads to a deflection angle of 5.15° in co-polarization and 10.30° in cross-polarization, according to equation 58, where $m = 0$. However, since the unit cell period is 575 nm and the THG wavelength is smaller than 450 nm, higher diffraction orders ($m = 1$) occur at higher deflection angles of 53.91° (co-pol.) and 63.87° (cross-pol.), which are due to diffraction of the TH light at the unit cell. However, the qualitative behavior is the same, which is shown in Figure 21b and c. The figure shows the back focal plane (the Fourier space) of the microscope objective lens as imaged onto the sCMOS chip. We observe a beam deflection of the frequency tripled light of $\pm (5.36 \pm 0.01)^\circ$ for the co-polarization states. The value is close to the design value of $\pm 5.15^\circ$. In the cross-polarization, the TH diffraction spots from the gradient metasurface appear at a deflection angle of $\pm (10.10 \pm 0.01)^\circ$, which is close to the desired deflection angle of $\pm 10.30^\circ$. The diffraction angles for the co- and cross-polarized TH light result from the different accumulated PB-phase at the metasurface. In contrast, a metasurface without gradient, where all nanostructures have the same orientation, shows a deflection angle of 0° , since all resonators radiate with the same geometric phase and constructively interfere under an angle of 0° , parallel to the optical axis of the setup. Furthermore, the brightness of the TH light is different for co- and cross-polarization. This is because the beam is generally elliptically polarized due to the selection rules described in Section 4.11. In this experimental setup, we project the generated TH light onto a circular polarization basis, but in a circular polarization basis, one would expect different intensities for co- and cross-polarized THG when decomposing the elliptically polarized light into a circular basis. Figure 22 shows the experimental results from the wavelength sweep between 1200 nm and 1350 nm for fields with and without gradient metasurfaces and for an unstructured silicon film of the same thickness as the nanofins (650 nm) for both co- and cross-polarization. Due to the gradient, the diffraction angle changes from 5.02° to 5.63° (co-pol.) and from 9.97° to 11.11° (cross-pol) if the fundamental wavelength is swept from 1200 nm to 1350 nm. Figure 22 shows the integrated intensity of each diffraction spot for co- and cross-polarization for the corresponding diffraction angles of the nonlinear metasurface without gradient. We observe that the THG intensity stays nearly constant over the whole fundamental wavelength range for co-and cross polarization. Further, it is evident that the co-polarised TH light is 2-3 times more intense than the TH light in the cross-polarization. The same trends are evident from the

metasurface without gradient. Note that the integrated TH intensity is always obtained from the zeroth-order. The TH intensity shows a broadband response over the whole spectral range of the magnetic resonance, which is typical for THG from dielectric metasurfaces from magnetic resonances. We also find that the THG signal from the metasurface is enhanced by a factor of ~ 40 (Figure 13c) for the co-polarization state compared to a 650 nm thick amorphous silicon film. The silicon film itself shows a negligible amount of THG in the co-polarization state, close to our detection limit. Note that the low THG signal from the silicon film is expected because amorphous silicon is an isotropic medium and does not generate TH light since THG is forbidden under circularly polarized excitation due to dipole selection rules. This leads to the assumption that the observed THG signal is due to the nanostructured amorphous silicon nanostructures since they break the isotropy of the film [39, 82]. In this context, it is worth noting that the bare ITO-coated glass substrate used as the substrate for the silicon metasurface also exhibits negligible nonlinear response for the same reason.

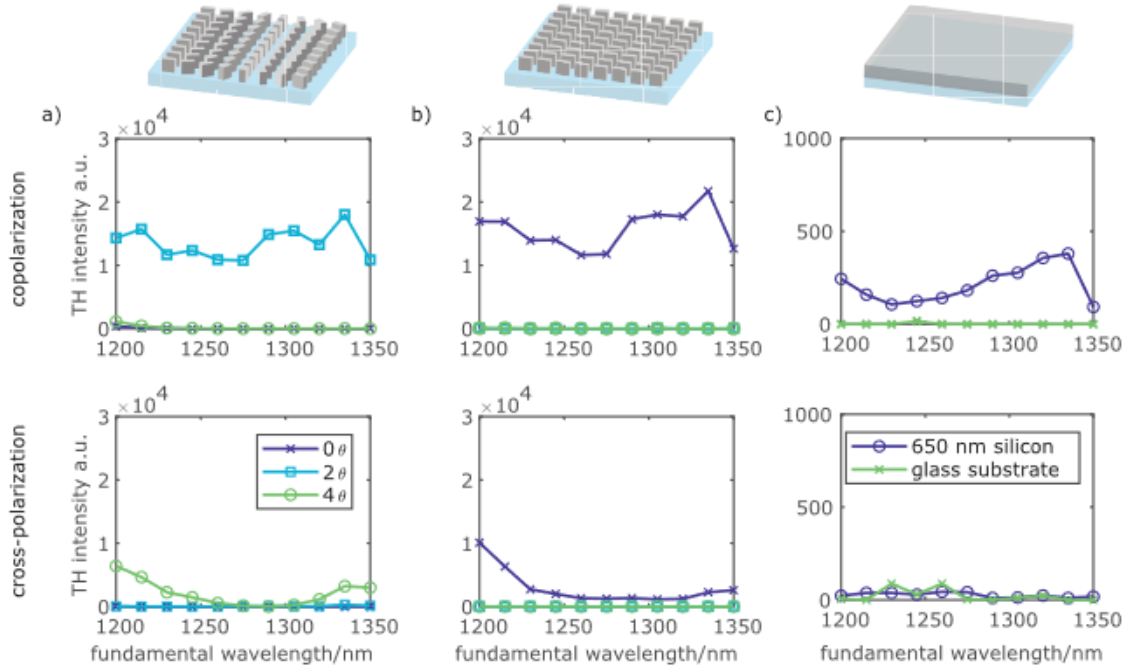


Figure 22. Measured THG intensity as a function of wavelength for the different combinations of input and output polarizations. a) The results for the metasurface with phase gradient show a nearly constant THG signal. b) The results for the metasurface without phase gradient. Here, only the zero order is analyzed, since each nanofin has the same rotation and thus the same phase. c) THG intensities of a 650 nm thick amorphous silicon layer and an ITO-coated glass substrate without silicon. The silicon layer shows only a weak THG in the co-polarization and a negligible signal in the cross-polarization. In comparison, the ITO-coated glass substrate shows a negligible THG signal in both polarization states [60].

4.8 Power dependence of the third harmonic signal and conversion efficiency

Next, we confirm the signature of the TH generation since the sCMOS camera used in this setup cannot distinguish between different wavelengths. Therefore, we verified the origin of the detected photons by measuring the intensity of the detected light as a function of the intensity of the pump laser at a fundamental wavelength of 1240 nm, as shown in Figure 23. Here we can see a nonlinear dependence of the detected light intensity on the input intensity. As described in Chapter 2.6 the generated light at TH frequency shows a cubic dependence on the pump intensity: therefore, we fitted a cubic function of the form $f(I_p) = aI_{pump}^b$ to the recorded values. Here, I_p represents the input intensity and a is a proportionality constant. The coefficient b contains information about the order. Here, $b=2.95$ for the co-polarization case and $b=3.49$ for the cross-polarization case, close to the theoretical factor $b=3$. The fit values and the goodness of fit are listed in Table 2. A comparison of the fit with the average THG intensity compared to the average fundamental input power can be seen in Figure 23.

Table 4. Fit values of the nonlinear fit function $f(I_p) = aI_{pump}^b$ to the pump power dependent measurement and goodness of fit.

	Coefficients (95% confidence bounds):		Goodness of fit			
	a	b	SSE	R ²	Adjusted R ²	RMSE
Co-polarization	0.01384 (0.009518, 0.01817)	2.953 (2.89, 3.016)	1.539e+06	0.9995	0.9995	320.3
Cross polarization	0.0001644 (-1.565e-05, 0.0003444)	3.49 (3.27, 3.71)	4.111e+05	0.9959	0.9995	320.3

In order to determine the THG efficiency, the integrated counts displayed in Figure 22 can be converted to an average TH power P_{THG} incident on the detector. However, the setup can significantly impact the conversion efficiency since only a fraction of the TH light generated

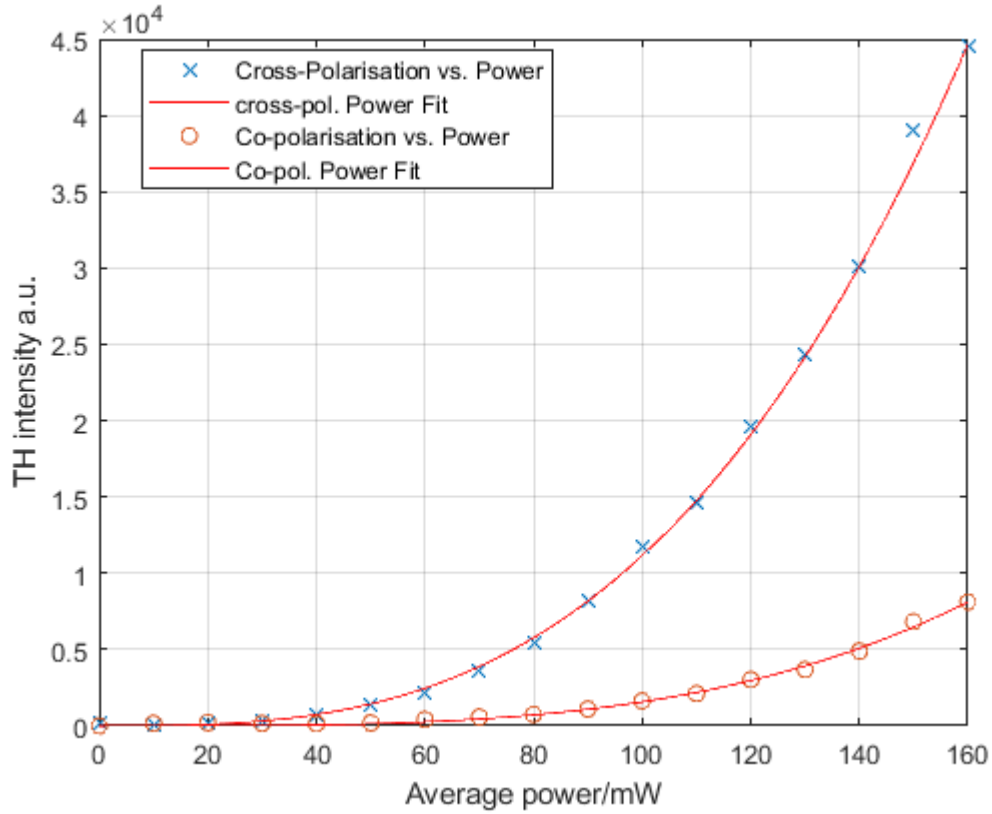


Figure 23. Average input power compared to the average third harmonic intensity. Measured values compared to the fit function $f(x) = ax^b$.

can reach the detector. Therefore, we need a factor $\eta_{corr}(\lambda)$ to correct for the transmission efficiencies of all optical components used in the setup and the detector's quantum efficiency. (For the setup depicted in Figure 21a, $\eta_{corr}(\lambda) \approx 0.5$.)

Furthermore, the used detector does not show intensity in SI derived units but in counts C_{THG} . Count is a measure of how many electrons are detected by the readout circuit of the detector. The gain of the camera depends on its operating mode and physical properties; here, one count corresponds to an amount of detected electrons. Finally, by considering the conversion factor from counts to electrons and the correction factor $\eta_{corr}(\lambda)$, we can calculate the average THG power P_{THG} as:

$$P_{THG} = \frac{C_{THG}}{\eta_{corr}(\lambda)t_{int}} \frac{hc}{\lambda_{THG}}$$

64

Where t_{int} denotes the integration time of the detector, h the Planck constant, c the speed of light and λ_{THG} the third harmonic wavelength.

By applying equation 64 to the wavelength sweep shown in Figure 22, the average power of the TH light is estimated as 5 pW. We estimate a conversion efficiency of $\frac{\hat{P}_{THG}}{\hat{P}_\omega^3} \approx 10^{-18} \frac{1}{W^2}$. Here, the average pump laser power is 50 mW. Literature values for the nonlinear conversion efficiency using magnetic Mie modes are in the range of $\frac{\hat{P}_{THG}}{\hat{P}_\omega^3} \approx 10^{-15} \frac{1}{W^2}$. Differences with the literature may result from the broadening of the resonance, results reduction in the quality factor and weaker THG, since the nonlinear TH intensity I_{THG} is proportional to the quality factors at the fundamental and third harmonic wavelength [58, 59]:

$$I_{THG} \sim Q_{3\omega} Q_\omega^3$$

65

Of course, α_{THG} also depends on the overlap integral of the mode at the fundamental and third harmonic wavelength. Here, the quality factor of the targeted resonance is around $Q_\omega = 13$ as can be seen from Figure 19a. Literature value for other Mie resonances in silicon are in the range of $Q = 50$ (see Table 2). Consequently, increasing the quality factor from 13 to 50 would increase the THG by a factor of 125, which would increase the nonlinear conversion efficiency by orders of magnitude. Since a high quality factor leads to a longer interaction time of the light with the material and therefore boosting the nonlinearity. Other reason for the low conversion efficiency can be a mismatch in the mode overlap integral at both the wavelengths [59].

4.9 Holography and the Gerchberg Saxton Algorithm

Since the geometric phase principle allows us to store optical information in a metasurface, we apply the principle to more complex beamforming applications such as holography. Holography allows us to store a wavefront in a medium and reconstruct it later. It is one of the best-known techniques for creating three-dimensional images from a two-dimensional medium, but it is also used in many other areas, for example, as a security marker on banknotes and ID cards, or in holographic interferometry, which enables us to measure the displacement of objects with optical interferometric precision [83]. A simple way of encoding a hologram is shown in Figure 24a. Here, monochromatic light with high coherence is used to illuminate an object, and the light scattered from the object is transmitted to a photosensitive plate. Another part of the original laser light is used as a reference and is also transmitted to the plate. On the photosensitive plate, both beams interfere, and the interference pattern of the reference beam and the scattered beam is recorded on the plate. This plate is called the hologram and contains the complete phase and amplitude information of the light scattered by the object. When the interference pattern is adequately illuminated, the light is diffracted, and the image is reconstructed by interference, as shown in Figure 24b.

However, Figure 24 shows the way to encode a hologram as a completely analog principle. First, a physical object is recorded in an optical system and then physically reconstructed with

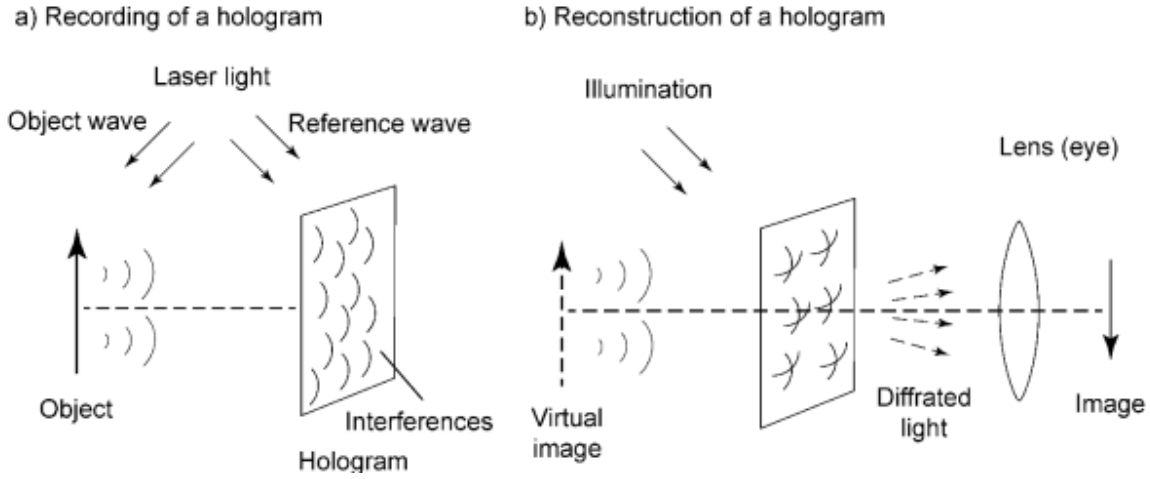


Figure 24. Recording and reconstruction of a hologram. a) To record the hologram, the scattered laser light of an object is superimposed with a reference beam on a light-sensitive Film. b) To reconstruct the hologram from the film, the hologram is illuminated with the same light source in the same direction as during recording. The hologram diffracts the light so that an observer can see a virtual image of the recorded object [83].

light. With the advancement of the modern technology, it has become possible to bypass the analog recording of a hologram and generate the interference pattern of an object directly in digital form. Subsequently, this interference pattern can be encoded in a physical medium, for example by applying the geometric phase principle in the nonlinear domain. In the last section, this process was used to generate a phase gradient to deflect light at an arbitrary angle. However, the geometric phase can be used to create more complex wavefronts that can be encoded in a metasurface, such as a phase-only hologram. In the case of a phase-only hologram, the transmission amplitude is constant for all nanoresonators across the metasurface, but the phase $\phi(x, y)$ changes spatially. That is, the complex transmission of the holographic metasurface is given by:

$$E(x, y) = u_0 e^{i\phi(x, y)}$$

66

Here, u_0 is the constant amplitude of the generated electromagnetic field. In order to encode any hologram into the metasurface, one must determine the spatial phase profile $\phi(x, y)$. In this work, the spatial phase profiles for encoding holograms are determined by a computer-generated holography algorithm, the Gerchberg-Saxton algorithm, developed by W.O. Saxton

and R.W. Gerchberg in 1972 [84]. The Gerchberg Saxton Algorithm belongs to the class of Adaptive-Additive algorithms, which compute the unknown part (Phase or Amplitude) of a propagating wave iteratively by Fourier Transform [85]. The basic idea of the algorithm is to propagate a wave from the hologram plane, where the pure-phase hologram is defined to the

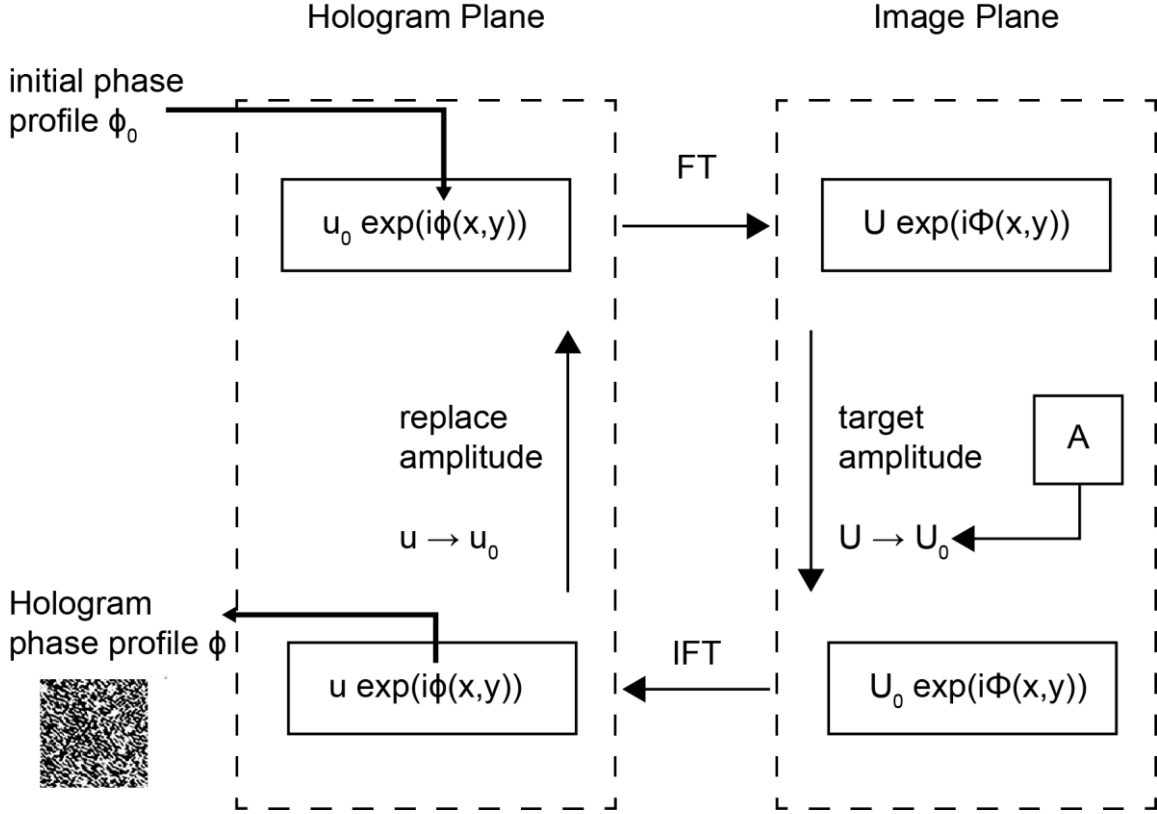


Figure 25. illustration of the Gerchberg-Saxton algorithm. First, a target image and a random phase are used for initialization in the image plane. The amplitude and phase are inverse Fourier transformed into the diffraction plane. Within the diffraction plane, the amplitude is replaced by a plane wave while the phase is maintained. After the Fourier transform of the diffraction plane into the image plane, the amplitude is replaced by the target image and the phase is retained for the next iteration.

image plane, where the holographic image is to appear and back, and compare and replace the result with the desired image to be encoded. A flowchart of the algorithm is shown in Figure 25. In the first step, the algorithm is initialized with a random phase distribution $\phi_0(x, y)$ and a uniform amplitude of the field $u_0 = 1$ to mimic a plane wave illumination. The total field is then given by $E_H = u_0 \exp(i\phi_0(x, y))$. Then, the field E_H is propagated from the hologram plane to the image plane by Fourier transformation, resulting in a field $E_I = U(x, y) \exp(i\Phi(x, y))$ in the image plane. Here, $U(x, y)$ is the amplitude of the field in the image plane which reflects the desired target image and $\Phi(x, y)$ is its phase distribution. At

this point of the algorithm, the amplitude $U(x, y)$ is replaced by the amplitude $U_0(x, y)$ of the target image while the phase distribution is retained so that the complex field is now given by $E'_I = U_0(x, y) \exp(i\Phi(x, y))$. Note that

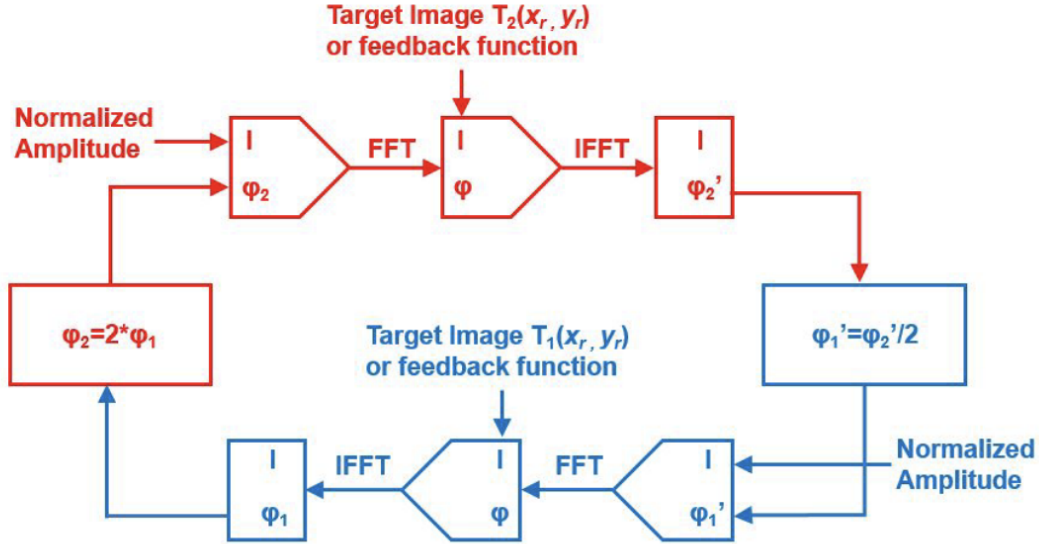


Figure 26. The flowchart of the modified Gerchberg-Saxton algorithm for generating the desired holograms. The red and blue parts of the diagram represent the processes involved in the original images 1 and 2, which are related to the phase profile of ϕ_1 and ϕ_2 . FFT and IFFT stand for Fourier transform and inverse Fourier transform, respectively. [60]

the target image is often given in terms of intensity $I_0(x, y)$, so that $U_0(x, y) = \sqrt{I_0(x, y)}$. An inverse Fourier transform of the field E'_I is then performed to propagate back into the hologram plane, where the complex field is then given by $E'_H = u(x, y) \exp(i\phi(x, y))$, where, $u(x, y)$ is the amplitude of the field in the hologram plane and $\phi(x, y)$ its phase distribution. In the last step of the algorithm, $u(x, y)$ is set to a uniform amplitude $u_0(x, y) = 1$. However, the phase distribution $\phi(x, y)$ is maintained, and the algorithm repeats the loop N times. By repeating the loop, the image quality of the reconstructed image is improved, and eventually, the reconstructed image converges to the target image [84]. There are several modifications to the algorithm described above to improve image quality. For example, instead of plane wave illumination, a different $u_0(x, y)$ can be chosen that more closely represents the illumination conditions to the experimental conditions. Note that to improve image quality and the converging speed of the algorithm, weighting functions can be introduced in several steps of the algorithm [83].

In this example of the Gerchberg-Saxton algorithm, only one phase distribution was considered. However, the phase response of nanoresonators in the nonlinear domain allows the encoding of more than one phase distribution. This results from the fact that two different phase responses in co- and cross-polarization are possible for THG from a nanoresonator with C_1 or C_2 symmetry. In this case, the Gerchberg-Saxton algorithm needs to be modified to account for two phase distributions [60], but the rotation angle need to be fixed for one value so that the relationship $\varphi_2 = 2\varphi_1 = 4\sigma\theta$ is satisfied. The Flowchart of the modified Gerchberg-Saxton algorithm is shown in Figure 26. A feedback function replaces the amplitude in the object plane to increase the convergence speed and improve the quality of the reconstructed images. Here, the phase relation of $\varphi_2 = 2\varphi_1$ is used in the iterations to combine two independent holograms, since the geometric phase differs by a factor of two in co- and cross-polarization. Then, we obtain the optimized pure phase holograms $\phi_1(x, y)$ and $\phi_2(x, y)$, which can reconstruct two completely different holographic images at the image plane. To realize metasurface holograms, we encode either $\phi_1(x, y)$ or $\phi_2(x, y)$ into the orientation angle of the nanofin according to the nonlinear PB phase principle. Then this metasurface can be excited by a laser beam to reconstruct the hologram at the third harmonic frequency. Interestingly, the Gerchberg-Saxton algorithm includes a Fourier transform to propagate from the holographic plane to the image plane. This step in the algorithm is similar to the Fourier transform performed by a microscope objective. Therefore, a holographic image placed in the front focal plane of a microscope objective would be Fourier transformed according to equation 63 and the holographic image would be reconstructed at the Fourier plane of the microscope objective. This opens the way to measure holograms in the same experimental set-up as explained in the Chapter 4.6.

4.10 Nonlinear Metasurface Holography

We encoded different holographic images: an image of the letter X and further a multiplexed hologram, which shows the image of a sun and a cloud in co- and cross-polarization, respectively. The obtained reconstructed images at the TH frequency are shown in Figure 27. The X hologram shown in Figure 27a is designed to be reconstructed in co-polarization within an angular range of $\pm 20^\circ$. The cross polarizations are not intended to carry any holographic information and therefore do not show a pattern in Fourier space. The digitally reconstructed hologram is shown in Figure 27b. In the case of the multiplex hologram (as shown in Figure 27c), the holographic images are reconstructed in both the co-polarization and the cross-polarization. In co-polarization, the reconstructed image of the sun appears, while in the cross-polarization, the image of the cloud appears. The bright spot in the center of the images is due to the residual THG signal, which does not carry any phase. The images show a slight speckle pattern, which is typical for reconstructing holographic images with laser radiation. Speckle patterns can be enhanced by imperfections and variations in the nanofins,

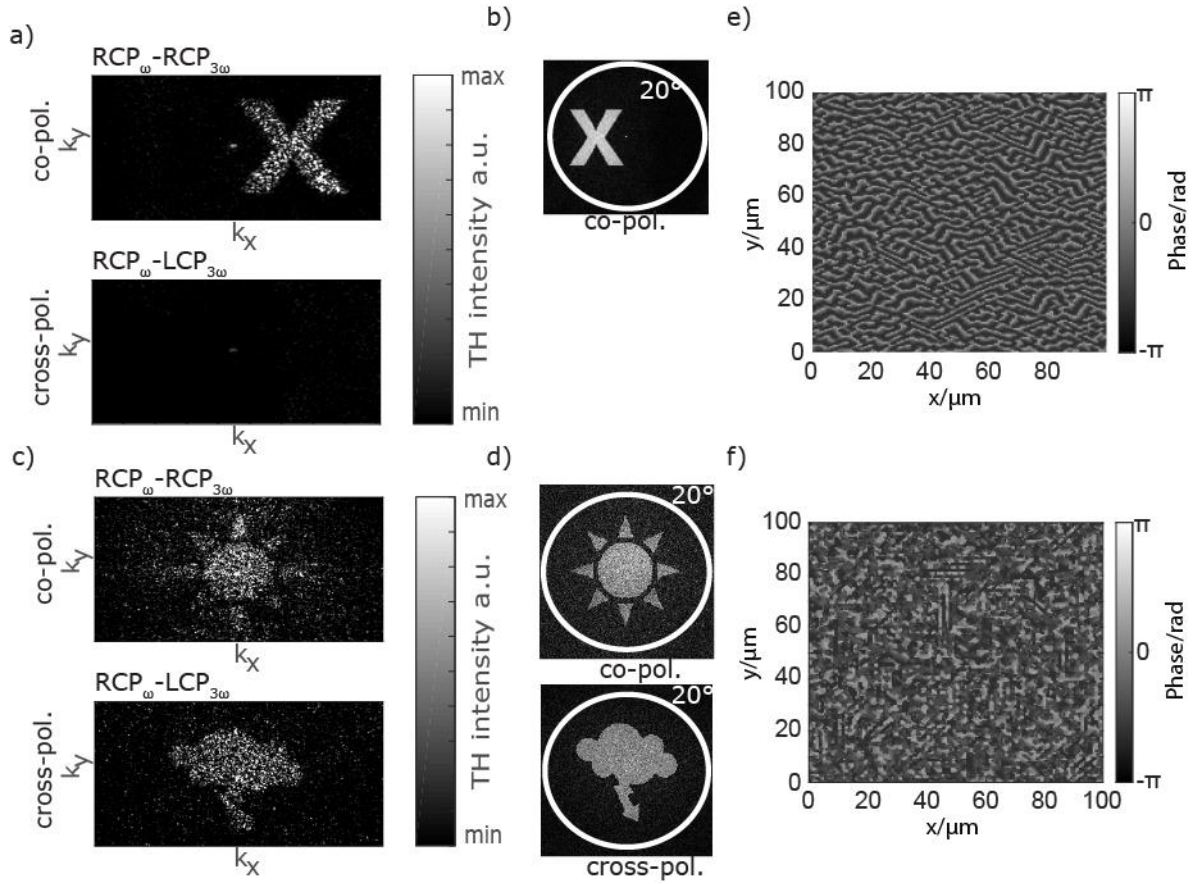


Figure 27. a) Measured holographic image of the letter X for different combinations of input and output polarizations. The image appears only in the state of co-polarization of the THG signal, while no image is seen in the state of cross-polarization. (b) The simulated holographic image of the letter X. The image is designed to appear within an angle of 20° in Fourier space. (c) Measured multiplexed holographic image for different combinations of input and output. (d) The corresponding simulated holographic image of the sun and the cloud for both polarization states. Spatial phase profile of the X Hologram (e) and the multiplexed hologram (f) [60].

glass substrate, and experimental illumination conditions. By reversing the polarization state of the fundamental beam, the hologram produces the conjugate image due to the change in the sign of σ in the phase factor. However, the reconstructed images in Figure 27a have higher fidelity than the reconstructed images in Figure 27c, the same trend is also observable in the digitally reconstructed hologram (Figure 27b,d). This is because, first, we use different images with a more complex shape for the multiplexing scheme and, second, the multiplexed phase distribution contains two images in two polarization channels. Therefore, the multiplexed hologram contains more information to be accommodated in the same space. This is also reflected in the phase distribution encoded in the metasurface, as can be seen in Figure 27e and f. Here the phase for the X (Figure 27e) and for the multiplexed hologram (Figure 27f) is

shown and for the multiplexed hologram, the phase changes more rapidly as a function of the coordinate on the metasurface than in the case of the X hologram. Furthermore, for experimental reconstruction, the metasurface of the multiplexed hologram must allow a larger phase change from unit cell to unit cell than the metasurface of the X hologram, which further reduces the phase resolution and thus the experimentally achieved fidelity, since both holographic metasurfaces have the same unit-cell size.

4.11 Nonlinear generation and geometric phase in view of rotational symmetries

In the last part, we saw that the geometric phase can be encoded in a nonlinear metasurface for THG. Now we want to discuss the geometric phase in relation with the rotational symmetry of the nanostructures. From plasmonic systems it is known that depending on the rotational symmetry in propagation direction only certain symmetries allow for THG. The universal concept of spin-rotation coupling for phase modulation in the nonlinear domain was presented by Li et al. [8, 82] and can be applied to dielectric nanoresonators, too. The symmetry of a nanostructure and its geometric phase response are related: For example, consider a structure with fourfold rotational symmetry (in short written as C_4). For example a cross, as shown in Table 5. The C_4 structure can be seen as a combination of two nanofins (in short called C_2 structures) which are rotated 90° against each other. One bar C^a has a rotation angle of zero and the other C^b has a rotation angle of 90° . As a result, the geometric phase response in co- and cross-polarization for both structures is given by $\phi_{Co,C^a} = \phi_{Cross,C^a} = 0$ and $\phi_{Co,C^b} = \pi$ and $\phi_{Cross,C^b} = 2\pi$. Therefore, the generated light will destructively interfere in co-polarization and constructively interfere in the cross-polarization channel, resulting in negligible THG in the co-polarization channel and stronger signal in the cross-polarization. This short example shows that a discussion of the nonlinear geometric phase is not complete without understanding the nonlinear selection rules that link the rotational symmetry of a nanostructure in the direction of light propagation to the third harmonic generation in a circularly polarized basis.

Consider a nanostructure with m -fold rotational symmetry (in short written as C_m) perpendicular to the propagation direction, for example Figure 28 shows a nanostructure with a twofold rotational symmetry. Again, the effective nonlinear susceptibility $\chi^{(n)eff}$ is used to derive the response of a nanostructure in relation to its rotational symmetry, as introduced in

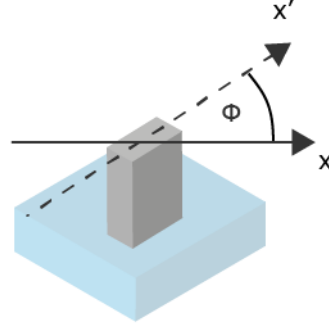


Figure 28. Nanostructure with C_2 rotational symmetry and a rotation at an angle ϕ .

Chapter 4.3. Here n is the order of the harmonic generation process. As already shown before, the nanostructures reacts with a nonlinear induced effective nonlinear polarization $P^{(n),eff}$ if pumped with a circularly polarized electromagnetic field E_σ at the fundamental frequency ω . Moreover, the induced effective nonlinear polarization has components in both the co- (σ) and the cross- ($-\sigma$) polarization, leading to:

$$P^{(n),eff} = P_\sigma^{(n),eff} + P_{-\sigma}^{(n),eff} \sim \chi^{(n),eff} (E_\sigma)^n$$

67

Where $P_\sigma^{(n),eff}$ is the nonlinearly induced effective polarization for circular polarized light with the same circularly polarization state and $P_{-\sigma}^{(n),eff}$ is the same with opposite circular polarization state. Now if we rotate the nanostructure in the laboratory frame by an angle of θ , the electromagnetic field in the nanostructures follows the rotation, but if we assume an m -fold rotational symmetry, the rotation would lead to the same geometrical and electromagnetic configuration after a rotation of $\theta = \frac{2\pi}{m}$, according to Neumann's principle. As a result the rotated electric field E' of the nanostructure would take the following form:

$$E' = E_\sigma e^{i\sigma \frac{2\pi}{m}}$$

68

The same must be valid for the nonlinearly induced effective polarization in the co- and cross-polarization states, where the rotated nonlinearly induced effective polarizations $P_\sigma'^{(n),eff}$ and $P_{-\sigma}'^{(n),eff}$ transform to:

$$P_{\sigma}^{(n),eff} = P_{\sigma}^{(n),eff} e^{i\sigma\frac{2\pi}{m}}$$

$$P_{-\sigma}^{(n),eff} = P_{-\sigma}^{(n),eff} e^{-i\sigma\frac{2\pi}{m}}$$

69

Applying equation 68 to the rotated frame defined above (equations 69) leads to:

$$P_{\sigma}^{(n),eff} e^{i\sigma\frac{2\pi}{m}} + P_{-\sigma}^{(n),eff} e^{-i\sigma\frac{2\pi}{m}} \sim \chi^{(n),eff}(E_{\sigma})^n e^{i\sigma\frac{2\pi n}{m}}$$

70




Due to the m-fold rotational symmetry of the nanostructure, a rotation of $\theta = \frac{2\pi}{m}$ would map the nanostructure and its electromagnetic fields on itself. Therefore equations 68 and 69 can be compared, which indicates that the exponential factors must follow certain conditions for co- and cross-polarization, since the term $\exp(i\sigma 2\pi n/m)$ needs to be equal to 1:

$$n = ml \pm 1$$

71

Where l is an arbitrary integer if n is positive and ± 1 indicates the Co(+)- and Cross(-)-polarization. This condition links the rotational symmetry m of the nanostructure to the harmonic generation process in a circular basis. If equation 71 cannot be satisfied, harmonic generation is not possible. For example, consider the nanostructure in Figure 28 and the

Table 5. Different rotational symmetries of nanostructures and the selection rules for third harmonic generation.

	C ₁ 	C ₂ 	C ₄ 
Third harmonic generation	Allowed in co - and cross -polarization	Allowed in co - and cross -polarization	Allowed in cross -polarization

generation of the third harmonic ($n=3$). The nanostructure would map onto itself if rotated 180° and therefore the rotational symmetry is $m=2$ (C₂). Under this condition Equation 71 can be satisfied for co-polarization and cross-polarization with an integer of $l = 1$ (co-pol.) and $l = 2$ (cross-pol.).

Table 5 shows the allowed third-order processes for nanostructures with different symmetries.

A mildly interesting consequence of these selection rules is that the beam is generally elliptically polarized when THG is allowed in co- and cross-polarization. Consider the third-order nonlinear polarization which was derived in Chapter 4.3:

$$P_L^{(3)eff} = \epsilon_0 \left[\chi_{LLLL}^{(3)eff} (E^L)^3 e^{2i\theta} + \chi_{LRRR}^{(3)eff} (E^R)^3 e^{-4i\theta} \right] \quad 72$$

$$P_R^{(3)eff} = \epsilon_0 \left[\chi_{RRRR}^{(3)eff} (E^R)^3 e^{-2i\theta} + \chi_{RLLL}^{(3)eff} (E^L)^3 e^{4i\theta} \right] \quad 73$$

For simplicity, let us assume that the fundamental beam has a left circular polarization and the nanostructures have C_1 or C_2 symmetry. In this case, the left circularly polarized pump light would be converted into left and right circularly polarized TH light and the brightness of the TH-light depends on the induced nonlinear polarization $P_L^{(3)eff} \sim \chi_{LLLL}^{(3)eff} (E^L)^3 e^{2i\theta}$ in co-polarization and $P_R^{(3)eff} \sim \chi_{RLLL}^{(3)eff} (E^L)^3 e^{4i\theta}$ in cross-polarization. In general, however, the effective third-order nonlinear tensor elements $\chi_{LLLL}^{(3)eff}$ and $\chi_{RLLL}^{(3)eff}$ need not be equal. Therefore, the brightness of the generated right and left circularly polarized light is different and the light is generally elliptically polarized. This is a reason for the difference in brightness for co- and cross-polarized THG, which is evident throughout this work, as mentioned in Chapter 4.7 and will become clear in the following chapters. Note that this effect is also observed in circularly polarized higher harmonic generation in crystals [39] and in plasmonic systems [82]. Note that it is generally not possible to determine analytically whether the THG is stronger for co-polarization than for cross-polarization and that one must rely on numerical simulations to calculate the brightness of the THG in Co- and Cross-polarization.

4.12 Geometric Phase for C_2 Rotational Symmetry

Figure 29a shows the schematic of the unit cell of a nonlinear metasurface made of nanostructure with C_2 rotational symmetry. The structures are made of amorphous silicon and are placed on a glass substrate with a low refractive index (SiO_2). The medium surrounding the nanostructures is air. The nanostructures' width, height and length are set to $w = 150$ nm, $h = 620$ nm, and $l = 300$ nm, respectively. The period is $p = 380$ nm, which is shorter than the TH wavelength to suppress the higher order diffraction of the TH signal and increase the uniformity of the nonlinearly generated wavefront. In addition, the wavefront is

illuminated with a left-circular polarized fundamental excitation at 1300 nm, resulting in a THG at 433.33 nm. Figure 29b shows the LCP and RCP components of the electromagnetic field within the nanostructure at the fundamental and third harmonic wavelengths, respectively. Due to the small size of the nanostructures, there is no resonant excitation with strong field enhancement in the nanostructure. Figure 29c shows the LCP, RCP, and total forward THG conversion efficiencies for nanostructures with different rotation angles, the plot indicates a coupling between the unit cells, since the conversion efficiency is strongly modulated in a rotation of 90° which is similar to the rotational symmetry of the square lattice. Further the change in peak-to-valley efficiency due to rotation is a factor of 2, indicating coupling in which the strength of the coupling changes with the distance between nanostructures. Figure 29d shows the THG conversion efficiency as a function of the fundamental wavelength from 1150 nm to 1500 nm. It can be seen that the THG conversion efficiency reaches a maximum at 1275 nm but increases towards shorter fundamental wavelengths as the electromagnetic field is better confined within the nanostructures. In addition, the efficiency of the RCP and LCP components also varies, especially for the cross-polarized component (RCP in this case), which is nearly zero at fundamental wavelengths above 1450 nm. As discussed in Chapter 4.11, the intensity of the TH light in co- and cross polarization is different since the light is elliptically polarized in the case of a C_2 symmetric structure. However, based on the above discussion, we numerically investigated the nonlinear geometric phase change for nanostructures with C_2 rotational symmetry by rotating the nanostructures gradually along one direction and investigating the nonlinear diffraction at the TH wavelength. Figure 29e and f show the simulated phase change of the LCP and RCP TH signals as a function of the rotation angle. It can be seen from the figure that the phase changes from π to $-\pi$ when the structures are rotated from 0 to 180° . However, for co-polarization, the phase changes at about two times the angle of rotation, while for cross-polarization, it changes at about four times the angle of rotation. This closely follows the nonlinear polarization in equation 58, indicating that the nanostructures exhibit a nonlinear geometric phase change as a function of rotation according to $e^{\pm 2i\theta}$ and $e^{\pm 4i\theta}$. Figure 29g and h show the obtained electric field at the third harmonic in co- and cross-polarization in the x-z plane of an array of nanostructures for the case where the angle of rotation changes by 10° ($1/18\pi$) from unit cell to unit cell. From the electric field it can be seen that the rotation results in the refraction of the generated TH light at angles of 1.78° (Co-pol.) and 3.67° (Cross-pol.), which are close to the angles of 1.82° (Co-pol.) and 3.63° (Cross-pol.) as calculated using equation 59 in both polarization combinations, which is following the nonlinear selection rules for THG and the nonlinear geometric phase principle. However, the wavefronts in co- and cross-polarizations exhibit slight modifications. The wavefront is not perfectly straight but is slightly curved, and a small modulation of the amplitude is also apparent. This indicates a change in the coupling among neighboring cells if the neighboring structures are rotated, which leads to the deviations between the phase response from a geometric phase gradient metasurface as depicted in Figure 29g and h and the phase response according to $e^{\pm 2i\theta}$ and $e^{\pm 4i\theta}$.

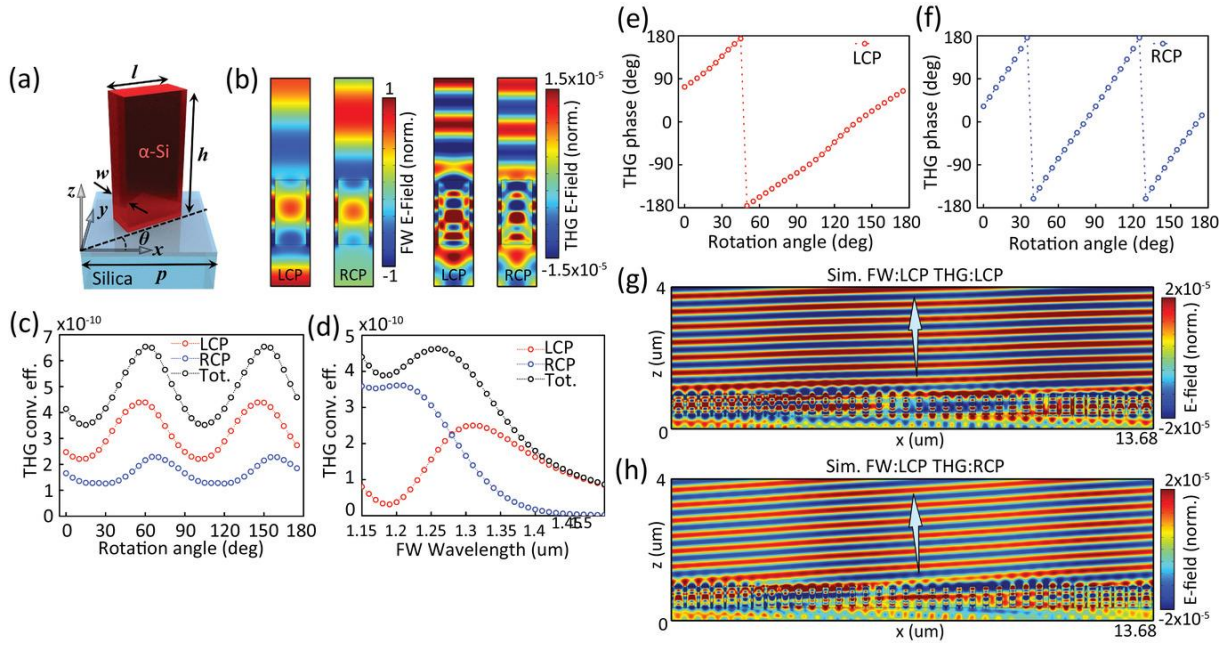


Figure 29. Nonlinear response of the locally rotated silicon nanofin array. a) Schematic representation of the silicon nanofin with in-plane C_2 rotational symmetry and its geometric parameters. b) The LCP and RCP components of the FW field at 1300 nm and the corresponding TH field of the silicon nanofin array, where the rotation angle is 0° . All fields are normalized by the amplitude of the FW input electric field. c) The LCP (red), RCP (blue) and total (black) forward THG conversion efficiencies of the rotated silicon nanofin array in the range of 0° to 180° with a rotation angle step of 5° . d) The LCP (red), RCP (blue) and total (black) forward THG conversion efficiencies of the rotated silicon nanofin array by sweeping the FW wavelength from 1150 to 1500 nm. Numerical calculation of the spin-dependent anomalous refractions of the TH signals generated by the nonlinear gradient phase metasurface. The simulated nonlinear geometric phase associated with the (e) LCP and (f) RCP TH signals when the LCP FW of wavelength 1300 nm is incident while rotating the silicon nanofins from 0° to 180° with a rotation angle step of 5° . The simulated free space field distribution of the g) LCP and h) RCP TH signal. All fields are normalized with the intensity of the FW input electric field [79].

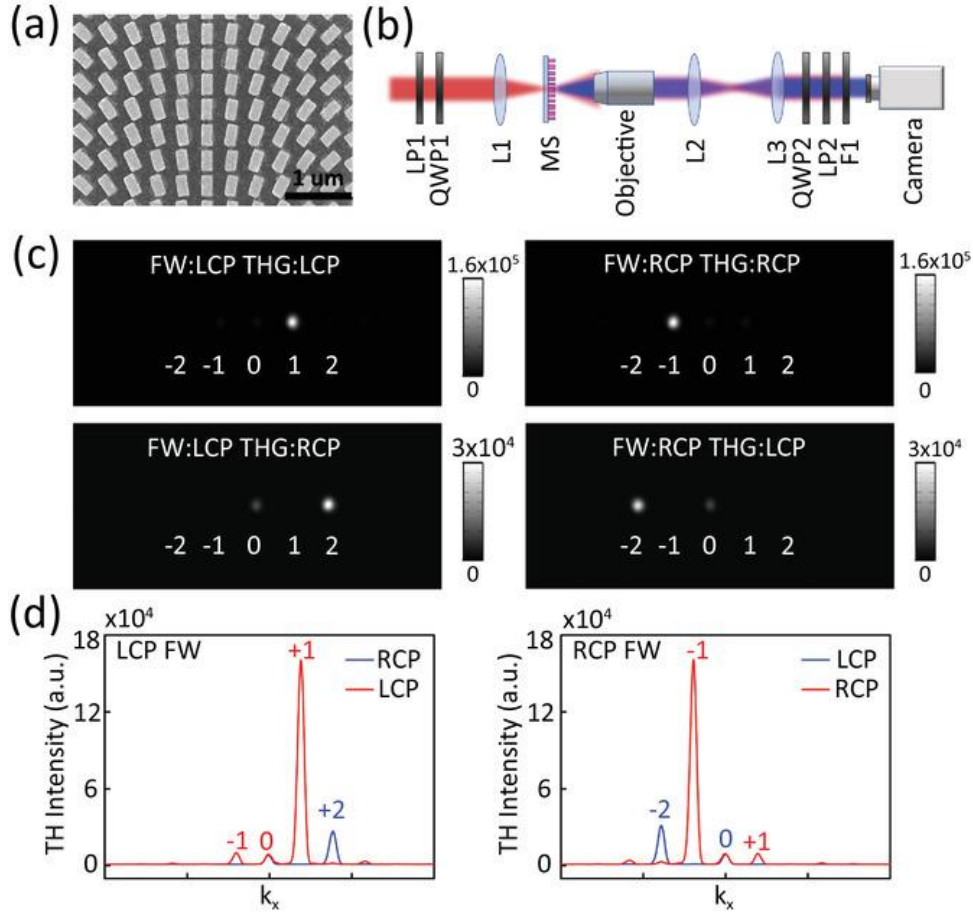


Figure 30. Experimental verification of the TH signals generated by an all-dielectric silicon geometric-phase metasurface with a spin-dependent surface phase gradient. a) Top view SEM image of the metasurface. The silicon nanofin with C_2 rotational symmetry is rotated by 9° . The scale is $1 \mu\text{m}$. b) Schematic of the experimental setup. F1 refers to the short pass filter; LP1 and LP2 refer to the linear polarizer; QWP1 and QWP2 refer to the quarter wave plate; L1, L2 and L3 refer to the focusing lens. c) The measured TH diffraction patterns under the illumination of the circularly polarized FW of wavelength 1200 nm . d) Intensity profile of the intersection line of the measured TH diffraction pattern [79].

For the experimental validation, we fabricated the metasurface on glass substrate. An SEM image of the fabricated structure is shown in Figure 30a and for experimental characterization of the nonlinear behavior of the structures, we used the same setup (Figure 30b) as explained in the chapter 4.5. Figure 30c shows the measured nonlinear diffraction of the LCP and RCP TH signals when the phase gradient metasurface sample is illuminated with left and right circularly polarized light of 1200 nm wavelength and 50 mW average power. The measured TH light is obtained at an angle $3.05^\circ \pm 0.01^\circ$ in co-polarization (LCP \rightarrow LCP) and at $6.09^\circ \pm 0.01^\circ$ for cross-polarization (LCP \rightarrow RCP), which is close to the design values of 3.01° (co-pol.) and 6.01° (cross-pol.), following the nonlinear geometric phase principle. In addition, the images show a small contribution from the conjugate (-1) diffraction order. However, there is also a

zero-diffraction order in the experiment that carries no phase. This can be explained by the coupling of neighboring cells which changes with the rotational angle, as explained earlier. Besides the coupling effect, fabrication defects and imperfections in the circular polarization state also reduce the diffraction efficiency and can contribute to the undesired diffraction in the zeroth and conjugate diffraction order.

4.13 Additional discussion about coupling effects in C_2 symmetry

To verify whether the coupling between the nanostructures causes the fluctuation of the nonlinear geometric phase shown in Figure 29, we simulate the geometric phase carried by the TH signals emitted from the metasurface. Here, the silicon nanostructure have different local orientations (see Figure 31a) and b) by fixing the long axis of the nanostructure along the x-axis (see Figure 31c) and rotating the unit cell itself instead of the structures. Figure 32a and b show the deviation between the simulated and the ideal linear geometric phase carried by cross-polarized FW output signals and nonlinear geometric phases carried by co- or cross-polarized TH signals. In this case, we assume the metasurface is fixed like shown in Figure 31a. From the simulation results, we find that the deviation also varies periodically when the local orientation changes, reflecting the square lattice's rotational geometry. Figure 32c and d shows the linear and nonlinear phase carried by the cross-polarized FW, co-, and cross-polarized TH signals radiated from the metasurface sample, where the nanostructures long axis is always collinear with the x-axis. The results show that the nonlinear geometric phase deviation is up to three times stronger than the linear phase deviation. This indicates a coupling between the unit cells which alters the phase response in this particular system. According to Ref. [69], in the linear domain, possible reasons for the deviation are given in terms of propagating waves in the plane of the metasurface and the excitation of Mie resonances, which are parallel to the direction of propagation but can be excited in the case of a rotational gradient. Further, the results show that the phase deviation is stronger in the nonlinear than in the linear regime.

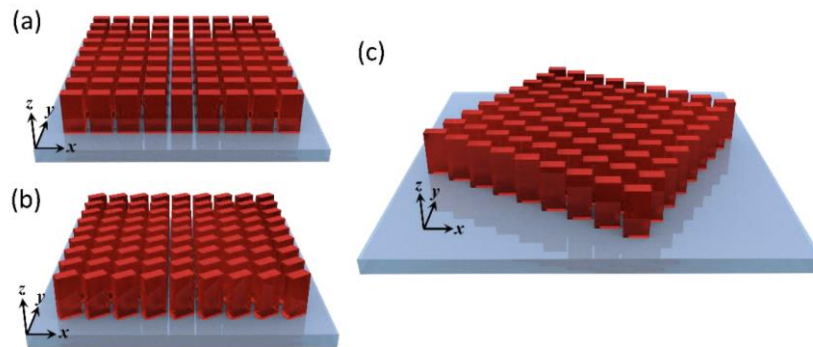


Figure 31. Illustration of a nanostructure array where the local orientation is (a) 0° and (b) 30° . (c) For the nanostructure whose local orientation is 0° , the array is rotated as a whole, but the long axis of the nanostructures is fixed along the x-axis.

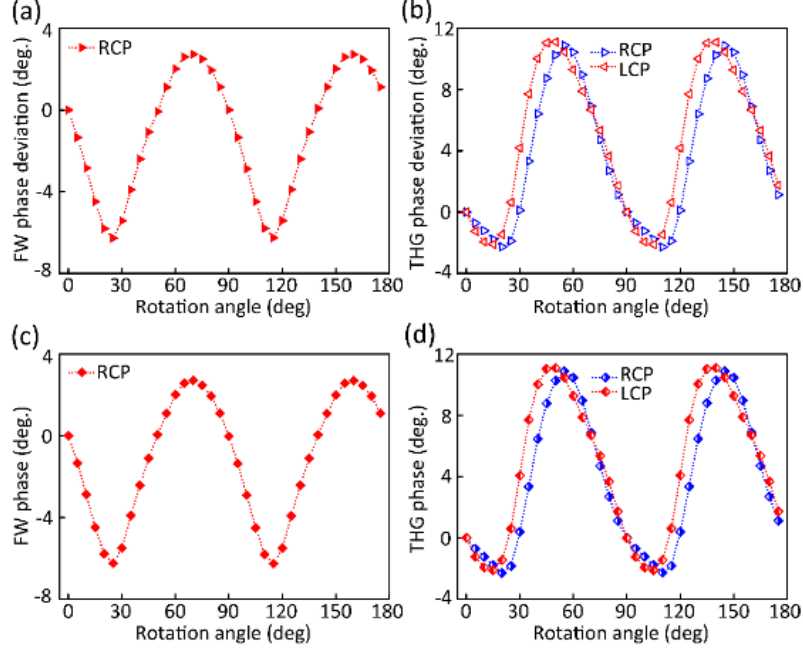


Figure 32. Influence of the coupling between adjacent unit cells on the geometric phase. When the metasurface sample is illuminated by a LCP FW with a wavelength of 1300 nm, the phase deviation between the simulated and ideal for linear (a) and nonlinear (b) geometric phase is shown with gradual variation of the local orientation. The linear (c) and nonlinear (d) phase for a silicon nanofin array with different local orientation, where the long axis of the silicon nanofin is always fixed along the x-axis [79].

To further investigate the phase distortion, we study the nonlinear geometric phase response for the co-polarized and cross-polarized TH waves when the metasurface sample is illuminated with LCP FW of different wavelengths as shown in Figure 33. Here, we choose a wavelength of about 1200 nm because we observed only weak co-polarized TH conversion efficiency, as shown in Figure 29d. In addition, the cross-polarized TH signal is nearly zero at pump wavelengths longer than 1450 nm. Here, the nonlinear geometric phase of the cross-polarized TH deviates from the expected relationship with the rotation angle when the FW wavelength is set to 1500 nm. It indicates that the coupling becomes stronger at longer wavelength for this particular system.

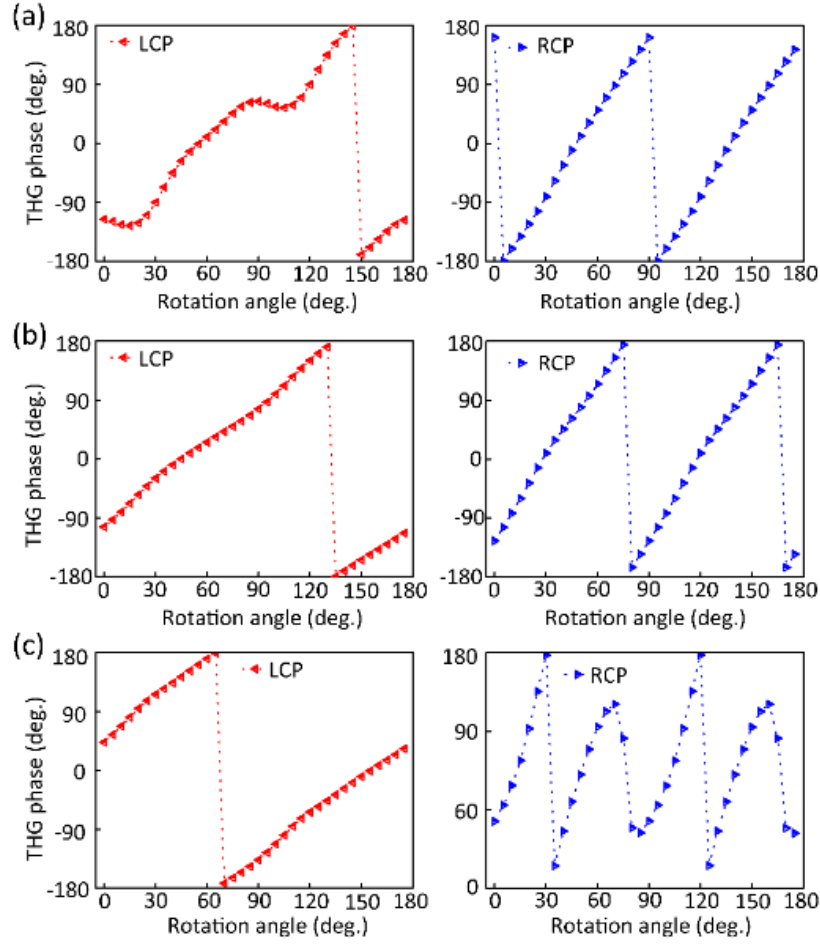


Figure 33. Numerically investigated nonlinear geometric phase when the metasurface is illuminated with LCP fundamental plane wave whose wavelength is (a) 1200 nm, (b) 1400 nm, and (c) 1500 nm, respectively [79].

4.14 C_1 rotational symmetry

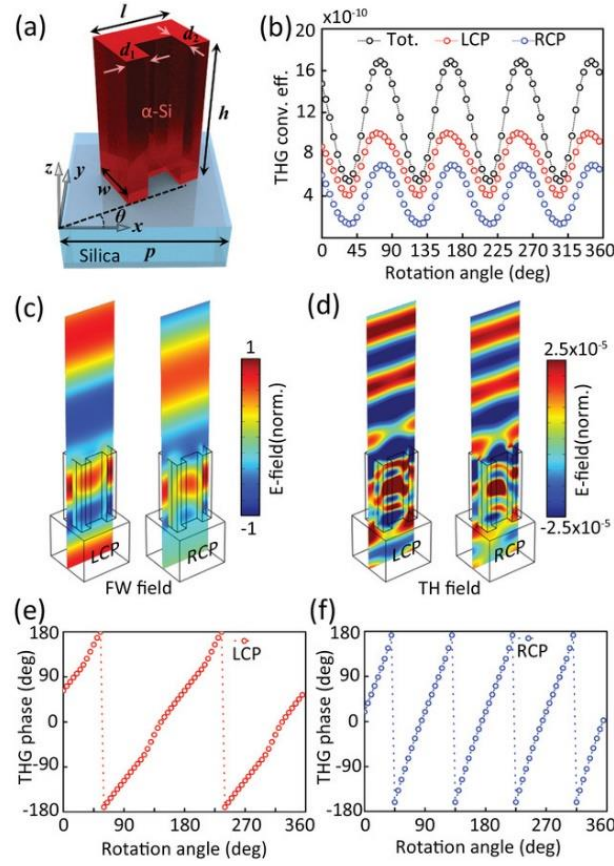


Figure 34. Numerical calculation of the TH signals generated by the all-dielectric geometric-phase metasurface consisting of a locally rotated silicon nanostructures with C_1 rotational symmetry. a) Schematic of the nanostructures and its geometry parameters. Selection of LCP FW at 1240 nm, b) the simulated THG conversion efficiency with stepwise rotation of the silicon nanostructures from 0° to 360° with a rotation angle step of 5° . Simulated field distribution of the LCP and RCP components of the c) total FW fields and d) TH fields. All fields are normalized to the intensity of the input FW electric field. Nonlinear geometric phase of the e) LCP and f) RCP TH wave due to rotation of the silicon nanofins from 0° to 360° with a rotation angle of 5° [79].

In addition to the C_2 case, we fabricated nanostructures with C_1 rotational symmetry, as shown in Figure 34. The C_1 nanostructure has a "U-shape" and the geometrical parameters are set to $w = 150$ nm, $l = 300$ nm, $d_1 = 80$ nm and $d_2 = 60$ nm, as illustrated in Figure 34a. The nanostructures' height and unit cell size were set to $h = 550$ nm and $p = 400$ nm to achieve higher THG conversion efficiency. When the nanostructures are rotated from 0° to 360° , the THG conversion efficiency changes due to the variation of the coupling between the unit cells, as shown in Figure 34b. The modulation shows a fourfold dependence on the rotational angle, compatible with the symmetry of the lattice. Figure 34c,d is the calculated electric field

distributions at the fundamental and third harmonic wavelengths for a fundamental wavelength of 1240 nm (413.33 nm TH wavelength). Note that the design is again

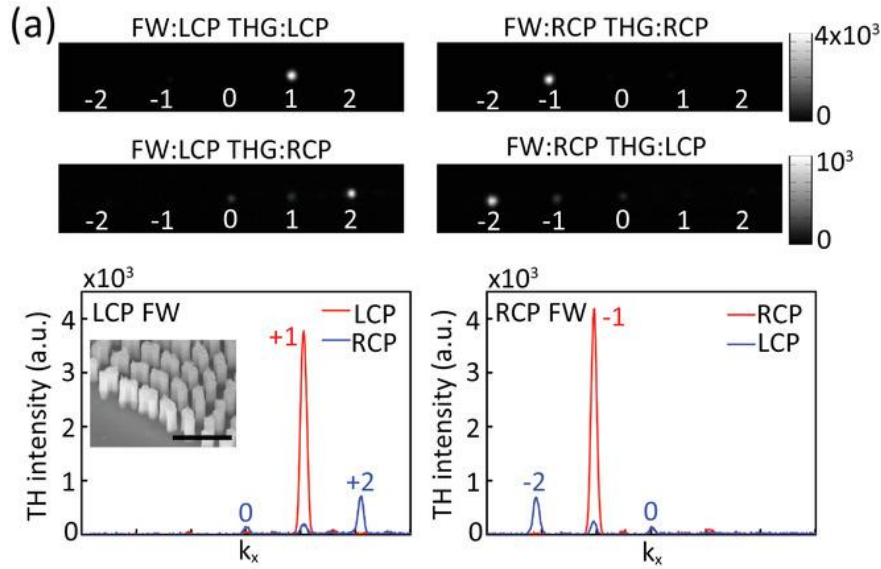


Figure 35. Measured diffraction pattern and intensity profile of TH waves radiated from the geometric phase gradient metasurface made of nanostructures with C_1 rotational symmetry. The scale of the inset SEM image is $1 \mu\text{m}$ [79].

non-resonant and therefore has low conversion efficiencies. However, again, the large fluctuation of the THG conversion efficiency as a function of rotation (here the THG conversion efficiency varies by a factor of 2.2) and the strong field outside the nanoresonator indicate strong coupling between the unit cells and distortion of the geometric phase, as already discussed for the C_2 symmetry case. Note that, as discussed in Chapter 4.11, the intensity of the TH light in co- and cross polarization is different, since the light is elliptically polarized in the case of a C_1 symmetric structure. Figure 34e and f show the numerically obtained nonlinear geometric phase change in response to rotation, which is consistent with the nonlinear geometric phase change expected from equation 58 and the nonlinear selection rules for a structure with C_2 rotational symmetry.

4.15 Experimental verification for C_1

The experimental outcomes from the C_1 metasurface is shown in Figure 35. Here, one gradient period contains 15 nanostructures, and the metasurface is illuminated with a circularly polarized laser beam with an average power of 50 mW and a fundamental wavelength of 1240 nm. The measured diffraction angles are $7.54^\circ \pm 0.001^\circ$ (co-pol.) and $15.29^\circ \pm 0.001^\circ$ (cross-

pol.), respectively, which are close to the theoretical values of 7.92° and 16.00° obtained from equation 59 for co- and cross-polarization. Further, as seen in the numerical investigation, the co-polarization shows a much stronger signal than the cross-polarization. The principle of the nonlinear geometric phase again determines the overall nonlinear phase response of the metasurface. However, unwanted diffraction spots appear in the measurements, but the contribution from these diffraction orders to the overall THG is small.

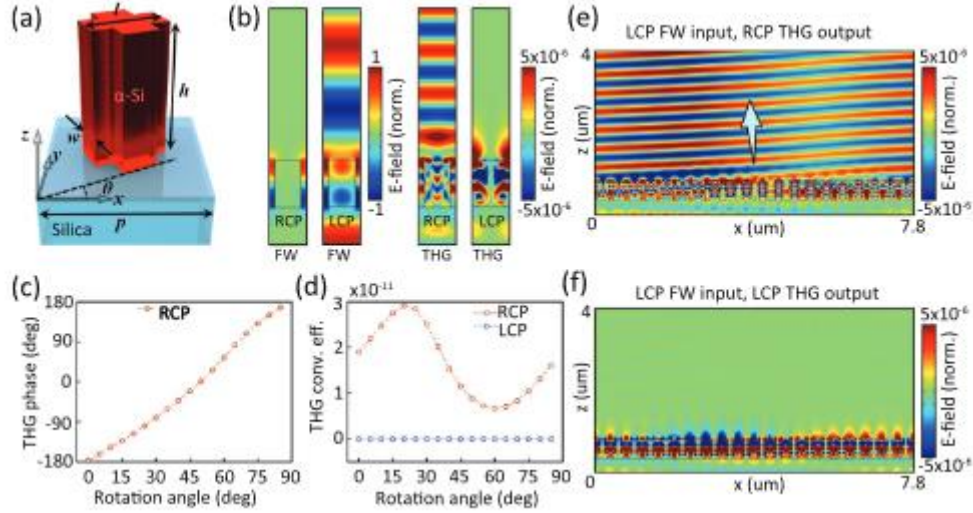


Figure 36. Numerical calculation of the nonlinear beam steering of the TH waves generated by the dielectric geometric-phase metasurface composed of silicon nanofin with C_4 in-plane rotational symmetry. a) Schematic representation of the silicon nanofin. Select the LCP FW wavelength as 1350 nm, b) the field distribution of the different circularly polarized components of the FW and TH fields excited in the silicon nanofin array whose local rotation angle ϑ is 0° . The nonlinear geometric phase c) of the RCP TH signal and d) the THG conversion efficiency of the RCP (red circle) and LCP (blue circle) TH waves when the silicon nanofins are rotated from 0° to 90° with a rotation angle step of 5° . The simulated TH field distribution in free space of e) the anomalously refracted RCP TH waves and f) the LCP TH waves, which are bound to the surface. All fields are normalized to the intensity of the FW electric field [79].

4.16 C_4 Rotational Symmetry

Next, we explain the case of a nanostructure with C_4 symmetry. As illustrated in Figure 36a, the width, length, height, and lattice constant are optimized as $w = 130$ nm, $l = 280$ nm, $h = 500$ nm, and $p = 390$ nm, respectively. In the numerical investigation, the metasurface was illuminated normally with a left circularly polarized fundamental excitation at 1350 nm (450 nm TH wavelength). Figure 36b shows the electric field plots at the fundamental and third harmonic excitation. The field enhancement in the case of the RCP component is much

stronger than the LCP component. Which Indicates that the nonlinear polarization for cross-polarized light χ_{RLLL} is much stronger than the nonlinear polarization for the co-polarized light, χ_{LLLL} , which means that only cross-polarized light is obtained in the THG process. Figure 36c, shows the geometric phase response if the nanostructures are rotated. We obtain a phase shift equal to four times the rotation angle, which is consistent with the nonlinear PB phase principle for cross-polarized light. Figure 26d shows the THG conversion efficiency as a function of rotation for co- and cross-polarized light. From the figure, the conversion efficiency in co-polarization is negligible, and the efficiency in cross-polarization is much stronger. Further, the conversion efficiency modulates with the rotational angle, and the maximum is approximately three times stronger than the minimum, indicating a stronger coupling between adjacent unit-cells. A brief phenomenological explanation for the disappearance of the THG for co-polarized light can be given with the geometric phase principle that was given in Chapter 4.11.

In addition, Figure 36e and f show the electric field distribution of the THG for co- and cross-polarization for nanostructures with a C_4 rotational symmetry which is rotated along one direction. Here, a full rotation of 90° is completed with 20 nanofins. The fundamental wavelength is set to 1350 nm in the simulation to increase the linearity between the local rotation angle and the geometric phase, which is due to the subwavelength nature of the array. Here, one can see that only a negligible part of the THG is radiated in the co-polarization, and the cross-polarization shows a strong THG. According to this numerical investigation, the diffraction angle is 3.36° , close to the theoretical value of 3.31° , as calculated using equation 59. The coupling is also evident in the numerical data, as discussed earlier for C_2 rotational symmetry: The wavefront shows modulation of the electric field amplitude in the x-direction. Moreover, although the rotation increases linearly from unit cell to unit cell, the phase front of the electric field at the third harmonic is not a straight line. Compared to the case of a geometric phase gradient with C_2 nanostructures, the modulation is even more significant. In co-polarization, the TH light is confined by the structure and does not radiate into the far field, according to the selection rules for nonlinear generation.

4.17 Experimental Results C_4

Experimentally, fabricated metasurface sample consists of rotationally symmetric C_4 nanostructures which complete a full rotation from 0° to 90° in 10 steps. In the experiment, the metasurface was illuminated with circularly polarized FW light of wavelength 1340 nm with average power of 50 mW. A diffraction angle of $6.12^\circ \pm 0.01^\circ$ was measured that agrees with the theoretical value of 6.58° . In the case of co-polarization, there is no THG to be

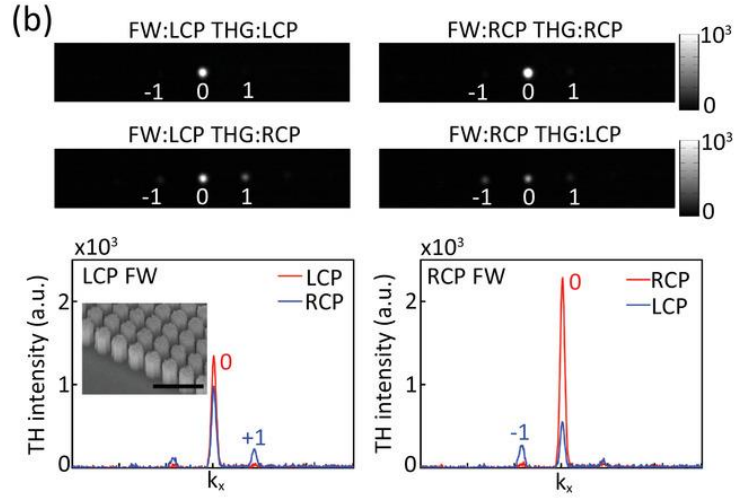


Figure 37. Measured diffraction pattern and intensity profile of TH waves radiated from the geometric phase gradient metasurface obtained for nanostructures with C_4 rotational symmetry. The scale of the inset SEM image is $1\ \mu\text{m}$ [79].

observed in a higher diffraction order. However, there is a strong TH light in the zeroth-diffraction order in co- and cross-polarization, which carries no phase information. This differs from the simulations, which show a generation of TH light only in the cross-polarization. In addition, the zeroth-order contributions are stronger than the phase response from the Pancharatnam-Berry phase principle, indicating an essential change in the geometry of the structures of the fabricated metasurface compared to the simulations. As can be seen from the SEM images, the C_4 structures exhibit strong rounding, and the geometry resembles a nano-cylinder rather than a cross with C_4 rotational symmetry. Therefore, the overall diffraction efficiency in the desired diffraction order decreases, and the zeroth-order response increases. Further, the coupling between adjacent unit cells, which is also apparent from the simulations, will decrease conversion efficiency, due to the modulation of the amplitude and phase of the THG light, as evident from the numerical model.

4.18 Conclusion

In summary the geometric phase can be integrated into the nonlinear generation process and used to direct and shape the generated light. It is possible to encode a wavefront into the rotation of any nanoresonator—for example, holographic images in the generation of higher harmonics from silicon metasurfaces. Furthermore, we can use the different geometric phase responses in co- and cross-polarization to multiplex holographic images with a modified Gerchberg-Saxton algorithm. One expects different geometric phase responses depending on the rotational symmetry. In the case of C_1 or C_2 rotational symmetry, the geometric phase is proportional to two times the rotation angle (co-polarization) and four times the rotation

angle in cross-polarization. Further, for a structure with C_4 rotational symmetry, we see only a geometric phase in the cross-polarization, proportional to 4 times the rotation angle, following the nonlinear selection rules.

Moreover, we have shown that due to the three-dimensional extension of the nanostructures, the linear phase behavior is distorted by the interaction between the nanostructures and the lattice. Here, we use amorphous silicon to realize the metasurfaces. However, as shown in this chapter, the nonlinear PB phase principle requires a circularly polarized fundamental excitation compared to a linearly polarized excitation in the case of nonlinear Huygens metasurfaces. Therefore, there appears a disadvantage for amorphous silicon in the context of nonlinear PB phase control because of its isotropic nature, as THG from an isotropic material under circularly polarized excitation is forbidden. In this chapter, the conversion efficiency (in the order of 10^{-9} 1/W^2) of the fabricated metasurfaces remains low compared to the similar works based on nonlinear extension of Huygens principle reported in the literature, presented in the Table 1 in Chapter 2.6, and the value is comparable to plasmonic systems. Consequently, the design of the amorphous silicon resonator for nonlinear PB phase control requires special attention to the design of the electromagnetic field and the symmetry of the nanostructure to achieve high nonlinear conversion efficiency for THG.

Chapter 5 Third harmonic generation and phase control with quasi-BIC and Mie resonances

In the last chapter, we used the rotation of silicon nanostructures to encode arbitrary wavefronts in a dielectric metasurface. However, the conversion efficiencies of the metasurfaces for THG presented in this work remain low compared to the state-of-the-art, presented in Table 2 in chapter 2.7. Two resonance mechanisms are mainly used to enhance the nonlinear conversion efficiency in metasurfaces: First, Mie resonances with finite lifetimes that lie within the light cone and consequently can couple to the free space. The excellent coupling between the resonance and the free space and the strong light-matter interaction make them ideal for wavefront shaping and efficient generation of higher harmonics. They allow easy coupling of an electromagnetic field with the strong nonlinear coefficients of high refractive index dielectric materials. On the other hand, metasurfaces or nanostructures can support electromagnetic modes that are decoupled from the radiation spectrum and therefore have very high quality factors (in theory $Q > 10,000$) [86], limited only by the non-radiative losses of the material that makes up the metasurface [53, 87]. However, there are several reasons why a mode can be decoupled from radiation spectra. First, these so called Bound states in the continuum (BIC) emerge from the destructive interference of different resonances in a single nanostructure [21, 86–89]. Second, they can be the result from a symmetry mismatch between the free space radiation spectrum and the mode, the so-called symmetry-protected BIC [21, 22, 87, 90].

Interference-based BICs are the result of destructive interference of different radiation channels. Destructive interference can occur between resonances of different resonators or different resonances in the same resonator. For example, if two nanoresonators are arranged on top of each other to form a cavity, the light that interacts with the two resonators accumulates an overall phase at a certain distance and wavelength, that may result in destructive interference [86]. On the other hand, BICs resulting from the interference of two resonances in the same nanostructure are called accidental BIC [21]. In order to understand accidental BIC, it is helpful to use multipole expansion and explain accidental BIC using their multipole modes [91]: The interference between two multipole resonances depends on their multipole expansion coefficients [23], as explained in Chapter 2.2: In general, the multipole expansion coefficients of a mode in a nanostructure are complex numbers. However, if the structure has inversion and time-reversal symmetry, the electric field of the structure's eigenmodes must satisfy the following conditions: $\vec{E}(\vec{r}) = \vec{E}^*(-\vec{r})$ [92]. This situation leads to a strict condition for the phase of each multipole in the multipole expansion due to the symmetry of the multipoles: The coefficients of the multipole expansion are all real and all multipoles are either in-phase (+) or opposite phase (-) [91, 92]. Therefore, one can find a resonance with a specific set of multipoles and a specific wave vector \vec{k}_1 where all multipoles

in the direction of \vec{k}_1 add up to zero. According to the optical theorem, for this particular radiation channel, an excitation or reradiation to free space is not possible. Figure 38a illustrates the formation of such an accidental BIC. Here, different Mie resonances destructively interfere in a nanostructure and close the radiation channels in the direction \vec{k}_1 [91]. On the other hand, a symmetry-protected BIC decouples from free space by a different mechanism, but a multipole decomposition can also explain this [91]. Consider a plane wave propagating in the z-direction, and an array of nanostructures expands in the x-y direction, as shown in Figure 38b. Here, all nanostructures are excited by a plane wave and oscillate in phase with each other. Note that in a photonic band diagram, in the Brillouin zone this case is called the Γ -point [90, 91]. However, due to their three-dimensional expanse, each nanostructure in the array has modes with multipole moments along the x, y, and z directions. Due to the symmetry of certain multipoles, when the multipole moment is aligned along the z-direction, the nanostructures cannot radiate in the z-direction under normal incidence because their multipole moments are parallel to the propagation direction of the light. This fact is illustrated in Figure 38b. For example, a dipole or a quadrupole oriented in the z-direction cannot radiate in the z-direction. In addition, the subwavelength nature of these arrays suppresses higher-order diffraction and closes all radiation channels. As a result, the mode is completely decoupled from free space, and the quality factor of the resonance is determined only by non-radiative losses.

This idea of decoupling a mode from the radiation spectra by utilizing its symmetry causes the various experimental realizations, and applications of BIC. BIC are an excellent choice for applications where high quality factors are essential. For example, lasers made from GaAs Metasurface, as shown in Figure 38c [93]. The metasurface is designed to support a BIC at the fundamental wavelength of 830 nm to enable lasing at the GaAs band gap emission wavelength of 830 nm at a temperature of 77 K. The nanostructures support vertical magnetic dipoles aligned along the z-axis. In addition, the period of the unit cell in the x-direction is sub-diffractive to confine the vertical magnetic dipole in that direction and enable a high quality factor mode to form the BIC. On the other hand, the period in the y-direction is larger to enable diffractive outcoupling of the emitted light at 830 nm under a certain wavevector, as shown in Figure 38c. Since the quality factor of the BIC resonance in this experiment reaches $Q = 2750$, the metasurface can be pumped at 780 nm, can reach the laser threshold, and starts lasing at a wavelength of 830 nm.

However, in addition to lasing, high quality factors become important in applications where strong light-matter interaction is vital, such as higher harmonic generation. For example, Figure 38d shows a metasurface that supports symmetry-protected BIC. The metasurface was designed to enhance THG [22]. By introducing an asymmetry in the geometry, it is possible to transform the symmetry-protected BIC into a quasi-BIC (QBIC) that can couple to the free space. The strength of the free-space coupling, which can be quantified by the linewidth or quality factor of a resonance, depends on the strength of the asymmetry, which can be

quantified by a parameter α . α compares the geometry of the symmetric structure with that of the asymmetric one. Figure 38e shows an example definition. Figure 38f shows the measured transmission of the metasurface for different asymmetry factors. As the asymmetry gets larger, the linewidth increases. Note that the quality factor decreases with increasing asymmetry, since $Q \sim 1/\alpha^2$ [94]. Figure 38g shows the THG intensity of the nonlinear

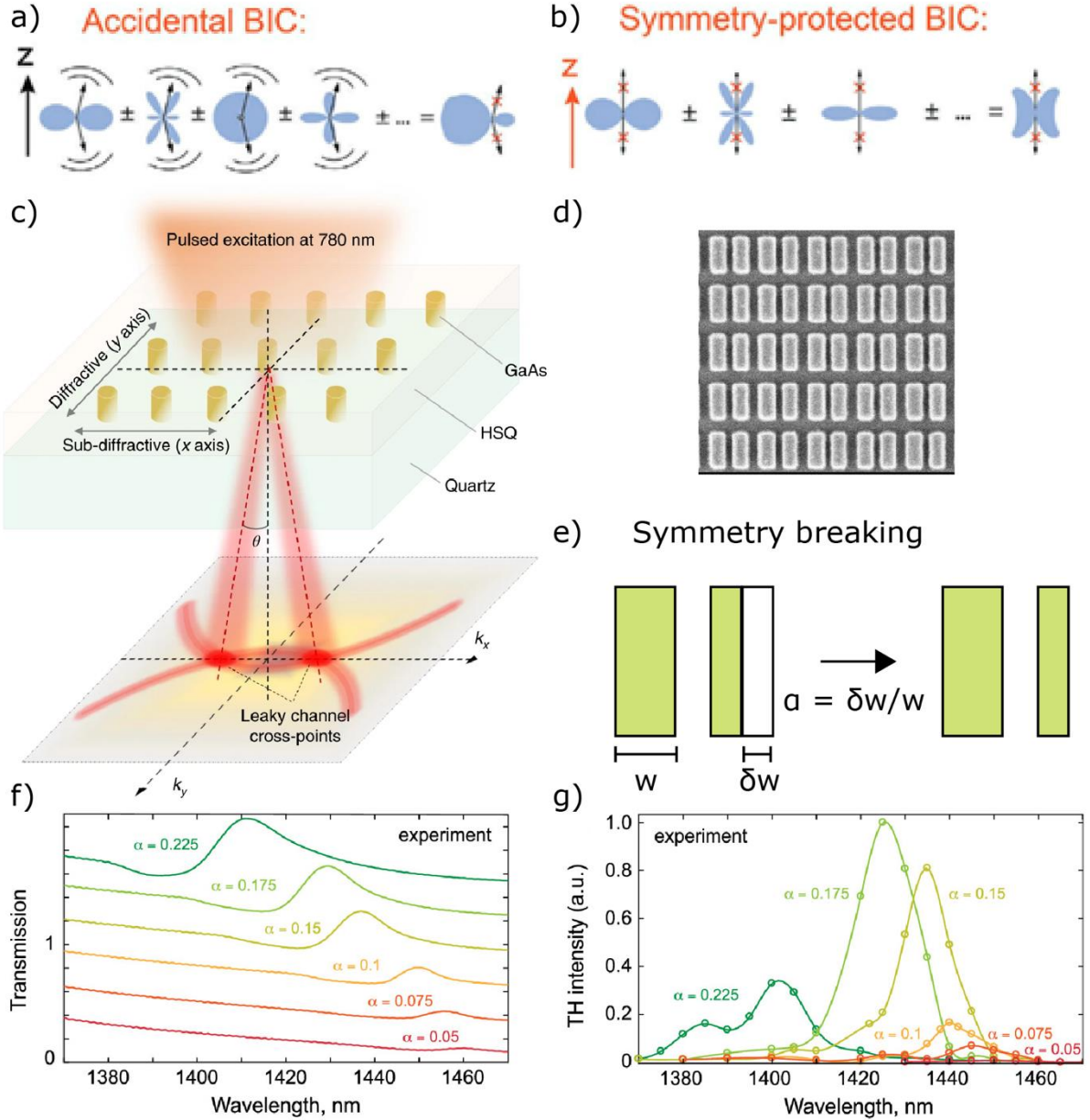


Figure 38. The formation of a) an accidental and b) symmetry protected BIC. c) Principle of a metasurface consisting of GaAs nano cylinders on a SiO₂ substrate embedded in hydrogen silsesquioxane (spin-on-glass). Along the y-axis, the period ($P_y = 540$ nm) was chosen to allow diffraction in the emission wavelength range of GaAs (~ 830 nm at 77 K). Along the x-axis, the period was fixed as 300 nm and is subwavelength. d) SEM image of a metasurface that

supports symmetry-protected BIC. e) Symmetry breaking in metasurface with two bars enabling QBIC with a width of w . By cutting one edge by a length of δw , one can break the symmetry. The asymmetry factor α is determined by the quotient of w and δw . f) Change of the measured transmission spectra as a function of the meta-atom asymmetry α . Note that the transmission is stacked. g) Measurement of the THG signal for different asymmetric metasurfaces in the region of the QBIC resonance. The circles show the experimental data. The solid curves are for orientation. a) and b) are taken from Ref. [91]. C) is taken from Ref. [93]. d) to g) from Ref. [22].

metasurface for different asymmetry parameters. One can see that the THG intensity increases with increasing asymmetry, peaks for a critical value of the asymmetry, and then decreases again. This observation contrasts with the naive view of QBIC resonance that an increasing quality factor leads to an increasing conversion efficiency, as explained in Chapter 2.6. This is because the coupling with free space modes becomes more difficult as the asymmetry/linewidth decreases. As a result, the energy that can be transferred from free space to the QBIC is limited as we use smaller and smaller spectral fractions of the pump light. Therefore, there is a trade-off between a high quality factor (small linewidth), which increases the conversion efficiency, and the energy that can be effectively transferred to the QBIC and converted into higher harmonic light. However, when this critical coupling condition is satisfied, the conversion efficiency of nonlinear processes can be increased by four orders of magnitude or more [53, 95] compared to Mie resonances. Note that lasers with a bandwidth of a few nanometers (femtosecond lasers) or less (picosecond lasers) are often used for nonlinear experiments. To effectively utilize the QBIC resonance, the linewidth of the laser λ_L and the resonance linewidth of the QBIC λ_Q should be matched such that $\lambda_L \approx \lambda_Q$ [20, 53]. Third harmonic conversion efficiencies for quasi-bound states in the continuum can reach $10^{-8} 1/W^2$ [53].

Given nonlinear wavefront shaping, QBIC resonances offer great potential because they produce strong nonlinear signals. To introduce a geometric phase, one needs to break the rotational symmetry of the nanoresonator. At the same time, a QBIC can be formed by symmetry breaking, which is a great tool to control the resonance and geometric phase with only one parameter, the asymmetry of the system. However, since symmetry-protected BICs form at the Γ -point of the first Brillouin zone, they are collective oscillations of many nanoresonators oscillating in phase [90, 94]. On the other hand, the geometric phase introduces a spatially varying rotation that can change the phase of the oscillations of QBIC from unit cell to unit cell. Since nonlinear optical properties are susceptible to small geometric changes, it is worthwhile to investigate the feasibility of QBIC in terms of nonlinear wavefront shaping.

5.1 Symmetry protected BIC in cylindrical nanostructures and quasi-BIC

We use a two-dimensional array of cylindrical amorphous silicon nanoresonators in this work. The metasurface consists of an array of cylindrical nanoresonators with an off-center air hole that changes the rotational symmetry of the cylinder from C_∞ to C_1 , as shown in Figure 39a. The geometry of the unit cell was designed based on the BIC mode to achieve high nonlinear conversion efficiency for THG with a fundamental excitation wavelength of ~ 1300 nm. The calculated linear transmission of the metasurface for a unit cell period of 664 nm under circularly polarized light is shown in Figure 39b. The figure shows a broad resonance dip at a wavelength of 1300 nm with a linewidth of ~ 50 nm that resembles a magnetic Mie resonance. A peak accompanies the Mie resonance at a wavelength of 1325 nm with a linewidth of ~ 8 nm, resembles QBIC. The magnetic field diagram at the wavelength of 1300 nm (top inset in Figure 39b) shows the magnetic dipole nature of the resonance in the x-y plane. Figure 39c shows the corresponding plots of the electric field in the x-z and y-z planes for the magnetic field in the x-y plane at the same wavelength. The electric field resembles a vortex in the x-z and y-z planes, typical of a magnetic Mie resonance with a magnetic dipole moment in the x-y plane. The magnetic dipole mode can enhance the nonlinear conversion efficiency as it allows efficient coupling of an electromagnetic field with the nonlinear susceptibility [96]. In contrast, the sharp transmission peak at 1325 nm shows an entirely different electromagnetic field profile compared to the Mie resonance at 1300 nm. At 1325 nm, the electric field diagram shows an asymmetric vortex in the x-y plane (lower part of Figure 39d), which is enhanced near the air hole. The magnetic field plots in the y-z plane show that the magnetic dipole moment of this resonance is slightly tilted compared to the cylinder axis, as shown in the bottom row of Figure 39d.

Let us consider the nanoresonator without the small hole to better understand the QBIC. The electric and magnetic field diagrams of such a cylinder are shown in the top row of Figure 39d. As can be seen in the magnetic field diagram, this nanocylinder features a vertical magnetic dipole mode parallel to the cylinder axis; therefore, the electric field of the mode forms a

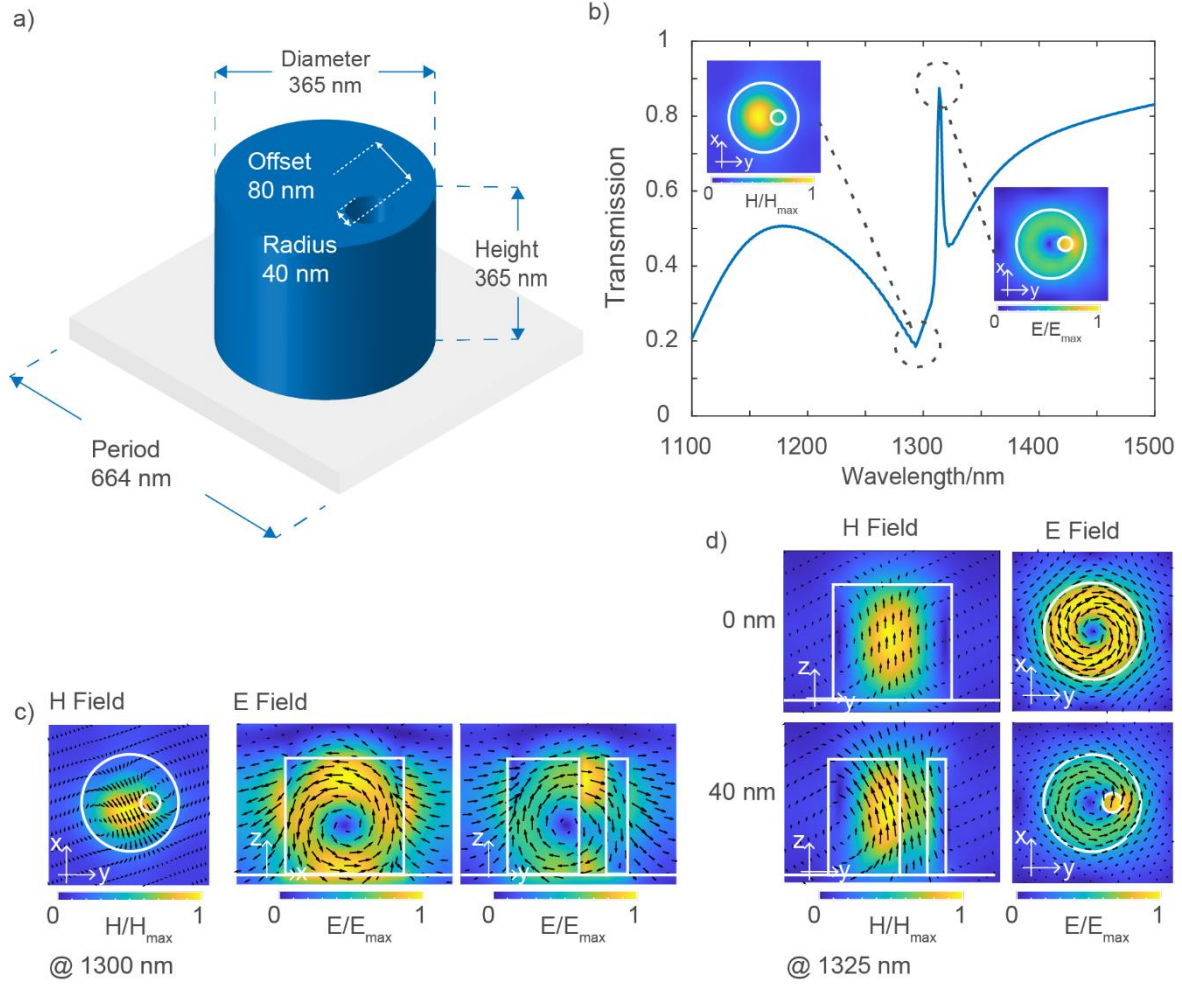


Figure 39. a) Design of a unit cell from a silicon cylinder with broken symmetry. b) Numerically obtained transmission spectrum of an array of such cylinders with a hole of radius 40 nm. The QBIC presents itself as a sharp transmission peak within a broad resonance dip. The insets show the mode profiles for the broad Mie resonance around the QBIC and the QBIC itself. c) Left, the magnetic field plot in the x-y plane for the magnetic Mie resonance at 1300 nm inside an amorphous Si cylinder with a hole of radius 40 nm arranged in a subwavelength array. Right, the corresponding electric field plots in the x-z and y-z plane of the magnetic Mie resonance. d) Electric and magnetic field curves inside an amorphous Si cylinder arranged in subwavelength arrays featuring BIC (without a hole, top row) and QBIC (with a hole of radius 40 nm, bottom row). The plots in the x-y plane show the electric fields at 1325 nm, while the plots in the y-z plane show the corresponding magnetic fields [97].

symmetric vortex in the x-y plane. The mode cannot couple to free space because the symmetry of the mode in the x-y plane does not match the symmetry of a plane wave at perpendicular incidence, and the period of the unit cell below the wavelength prevents any wave vector that is not perpendicular to the metasurface. These properties eliminate possible channels for radiation decay, resulting in a high quality factor and long lifetime. The long

lifetime of these BICs is crucial for high nonlinear conversion efficiency, as it allows for more prolonged interaction between the trapped energy and the nonlinear susceptibility of the material. By incorporating an off-center hole in the cylinder, one can break the in-plane symmetry of the nanoresonator, open two radiation channels perpendicular to the metasurface, and the BIC is then converted into quasi-bound states in the continuum (QBIC) capable of coupling to the free space [90]. The corresponding electric and magnetic fields

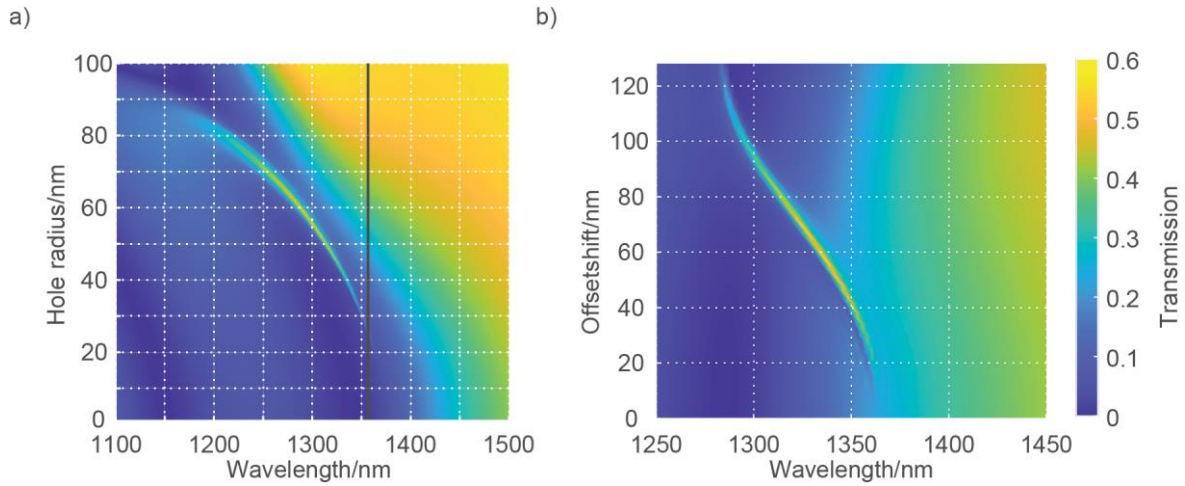


Figure 40. a) The numerically determined transmission of the nanoresonator array between 1100 nm and 1500 nm as a function of the hole sizes. The line width increases with increasing hole size. The gray line represents the spectral position of the BIC without interference. b) The numerically determined transmission of the nanostructure between 1100 nm and 1500 nm as a function of the offset of the hole from the center. At an offset of 0 nm, the hole is located directly in the center of the nanocylinder [97].

for the QBIC for an arrangement of cylinders with holes of radius 40 nm are shown in the bottom row of Figure 39d. Compared to the electric field diagrams for a cylinder without a hole, the hole leaves the electric field vortex largely intact but leads to a field enhancement in its surrounding area. This feature leads to a nonzero electric dipole moment in the x-y plane, which matches the plane wave's symmetry at normal incidence.

In this example of QBIC, the asymmetry is controlled by the off-center air hole. Therefore, the asymmetry can be characterized by the size of the air hole and its position from the center of the cylinder. Figure 40a shows the numerically determined nanostructure transmission between 1100 nm and 1500 nm as a function of hole sizes. The QBIC resonance shifts to shorter wavelengths with increasing hole size from about 1350 nm to 1150 nm. Moreover, the linewidth increases with increasing hole size from 0 nm to 20 nm because the hole size controls the asymmetry of the resonator and the QBIC. A larger asymmetry leads to stronger

coupling with free space as the net dipole moment becomes stronger. As a result, the coupling with free space increases, which shortens the mode lifetime and increases the linewidth. When the hole size becomes too large, the QBIC resonance "merges" with the Mie resonance in its surrounding. In addition, the hole can be placed at different locations away from the center of the cylinder, as shown in Figure 40b. The influence of QBIC resonance as a function of offset of the air hole from the center of the cylinder is shown. Here, the distance of the air hole to the center of the cylinder is varied, while all other variables are as described in Figure 39a. At zero offset, the air hole is at the center of the cylinder, so the symmetry of the system is not broken, and the QBIC resonance disappears. However, as the displacement increases, the QBIC resonance becomes visible as its linewidth increases, reaching its most apparent appearance at a displacement of 60 nm from the center of the cylinder. At this position, the air hole begins to overlap with the "center" of the vorticity in Figure 39d. Beyond this shift, the visibility of the QBIC resonance decreases again as the linewidth decreases again.

5.2 Nonlinear geometric Phase of QBIC

The symmetry breaking due to the air hole allows the BIC to couple to free space by modifying the system's symmetry. In addition, one can introduce the geometric phase approach to this system. As explained in the last chapter, a C_1 symmetric structure allows for a geometric phase response in the co- and cross-polarization of $2\sigma\theta$ and $4\sigma\theta$, respectively. However, for functional applications such as nonlinear holography, a high spatial density of nanoresonators is required to obtain high-fidelity holographic images since the image quality increases with spatial phase resolution. On the other hand, as the density of the resonators increases, the near-field coupling between the neighboring unit cells increases, leading to a deviation from the geometric TH phase relationship as shown in equation 58 in Chapter 4.3. This results in increased crosstalk between the different polarization channels and introduces phase noise that limits diffraction efficiency, as discussed in chapter 4.12. Due to the near-field coupling, there is always a compromise between the PB phase relationship and a high spatial phase resolution. To evaluate the trade-off between the near-field coupling and the geometric phase, we numerically investigated our design with third-harmonic generation and the corresponding nonlinear phase for different periods. The color plot of the transmission spectra in the wavelength range of 1100-1500 nm as a function of the period of the unit cell p (500-900 nm) is shown in Figure 41b. The transmission spectrum shows a sharp peak embedded in a much broader resonance corresponding to the QBIC, as shown previously in Figure 39b. By increasing the unit cell period, the QBIC resonance wavelength can be varied from 1225 nm to 1400 nm. At the same time, the peak remains spectrally narrow with a linewidth of ~ 8 nm since the linewidth is mainly controlled by the size of the hole and its position from the center, which were kept constant in these simulations. The plots of the simulated nonlinear geometric phase and TH intensity in the zeroth diffraction order for different periods of the unit cell (609

nm to 730 nm) are shown in Figure 41c-e. The Figures show that the TH intensity for different unit cell sizes remains within the same order of magnitude as expected by the uniform linewidth of the QBIC peak. Moreover, the TH intensity in co-polarization is stronger than the TH intensity in cross-polarization, since the overall TH from the nanostructure is elliptically polarized. In addition, the TH signal is susceptible to the fundamental wavelength around the QBIC resonance. The intensity of the signal is significantly reduced when the excitation wavelength deviates further from the resonance. The above observations prove that QBIC is the main contributor to the THG in the numerical simulation. Figure 41c-e also show the TH geometric phase change as a function of the rotation of the cylinder at the QBIC wavelength.

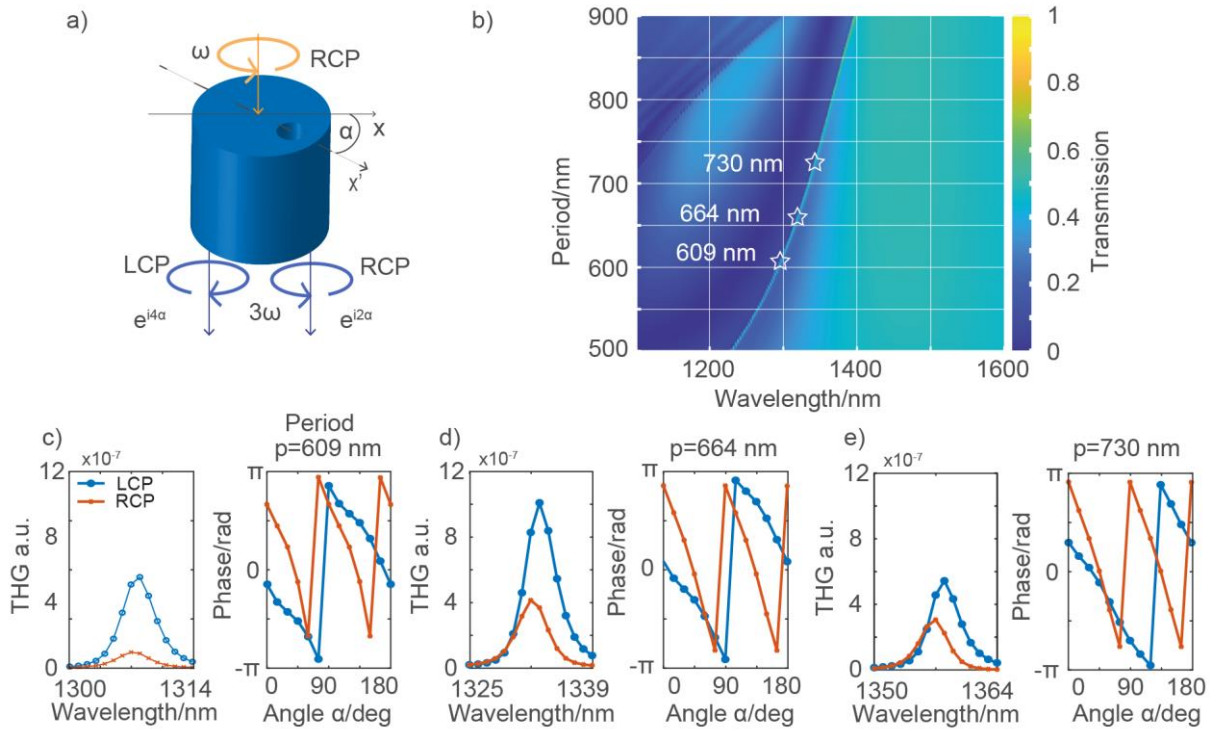


Figure 41. a) geometric phase for THG from a nanoresonator with C_1 rotational symmetry. Due to the broken symmetry in the cylinder, the light at the TH frequency carries a phase in co- (RCP to RCP) and cross-polarization (RCP to LCP). b) Two-dimensional plot of the transmission spectra of the metasurface, which consists of cylinders with an off-center hole, for different periods from 500 nm to 900 nm. The QBICs form a transmission peak in a broader resonance cavity. The inserts represent different periods for nonlinear investigation. (c-e) Left: Plots of TH signal strength as a function of pump wavelength in the vicinity of the QBIC resonance for the different periods (609 nm, 664 nm, and 730 nm) as marked in b). The fundamental wavelength ranges from 1300 nm to 1314 nm (609 nm period), 1325 nm to 1339 nm (664 nm period), and 1350 nm to 1364 nm (730 nm period), corresponding to TH wavelengths of 433.33 nm to 438.00 nm, 441.67 nm to 446.33 nm, and 450.00 nm to 454.67 nm, respectively. Right: The nonlinear geometric phase of the generated TH light as a function of the rotation of the C_1

cylinder between 0° and 180° for the fundamental wavelengths of 1307 nm (c), 1332 nm (d), and 1357 nm (e) [97].

In addition, the nonlinear phase relationship becomes more linear with larger periods as the near-field coupling becomes weaker with the increasing period. Therefore, the period is critical to optimize the system for nonlinear geometric phase control while maintaining a uniform TH intensity.

5.3 Experimental Results

Based on the design described in the last chapter, we fabricated ten different metasurfaces of size $100 \times 100 \mu\text{m}^2$ for five different periods of the unit cell (562 nm, 609 nm, 664 nm, 730 nm, 811 nm). For every period, we fabricated two metasurfaces, one with and one without a blazed phase grating. In the case of the phase grating, the angle of rotation of the nanoresonator along the x-direction increases by 22.5° from unit cell to unit cell. Consequently, a full rotation of 360° is achieved in 16 unit cells. Two scanning electron microscopy (SEM) images of the metasurfaces, one without phase gradient and one with phase gradient, are shown in Figure 42a and b. Details of the nanofabrication processes can be found in the Chapter 3. From several SEM images, it is possible to determine the average radius of the cylinders to be (182.5 ± 3.5) nm which is close to the desired diameter of 182.5 nm. However, the average radius of the off-center holes is smaller than desired, varying from 20 nm for a period of 562 nm to 35 nm for 811 nm.

5.4 Linear Transmission

The linear transmission spectra were measured with a white light laser source (Fianium Whitelase) in the spectral range from 1150 nm to 1300 nm. We also controlled the input polarization with a linear polarizer. A 10x infinity-corrected microscope objective captured the transmission of the metasurface. The light was directed to a spectrometer (Andor Shamrock Kymera 193) with a series of lenses. The spectrometer was equipped with an InGaAs detector (Andor IDus 491A InGaAs) to measure optical transmission in the infrared. The spectral resolution of the setup is 1.43 nm. Figure 42a and b show the linear transmission for different input polarization of the metasurfaces for different unit cell sizes. The polarization state is defined in the inset. The plots show a broad transmission dip within the wavelength range from 1250 nm to 1300 nm. However, the transmission shows an obvious difference between the two polarizations. The resonance dips for horizontally polarized light are at a shorter wavelength than the resonance dips for vertically polarized light at the same periods. The broad transmission dip shifts to a longer wavelength as the unit cell size increases, which is

consistent with the simulations. In addition, the shape of the resonance dip differs for the two polarization states. In the case of vertical polarization, the resonance dips are asymmetric for all unit cell sizes, while they are symmetric in the case of horizontal polarization. The apparent asymmetry in the vertically polarized transmission of the metasurfaces could be due to the influence of QBIC since the QBIC mode is linearly polarized in the vertical direction, as shown in Figure 39d and as discussed in Ref. [90] and since the asymmetry vanishes in the cross (horizontal) polarization. However, the expected sharp transmission peak observed in the numerical study of the transmission spectra is not observed experimentally. Possible reasons for this behavior are discussed later.

5.5 Nonlinear Measurement Setup

The nonlinear measurements were done in a similar setup to the one explained in chapter 4.6 but some of the components were changed to accommodate the experimental demands. Here, we use an optical parametric oscillator with a pulse length of 200 fs and a repetition rate of 80 MHz as a coherent light source for the nonlinear optical experiments.

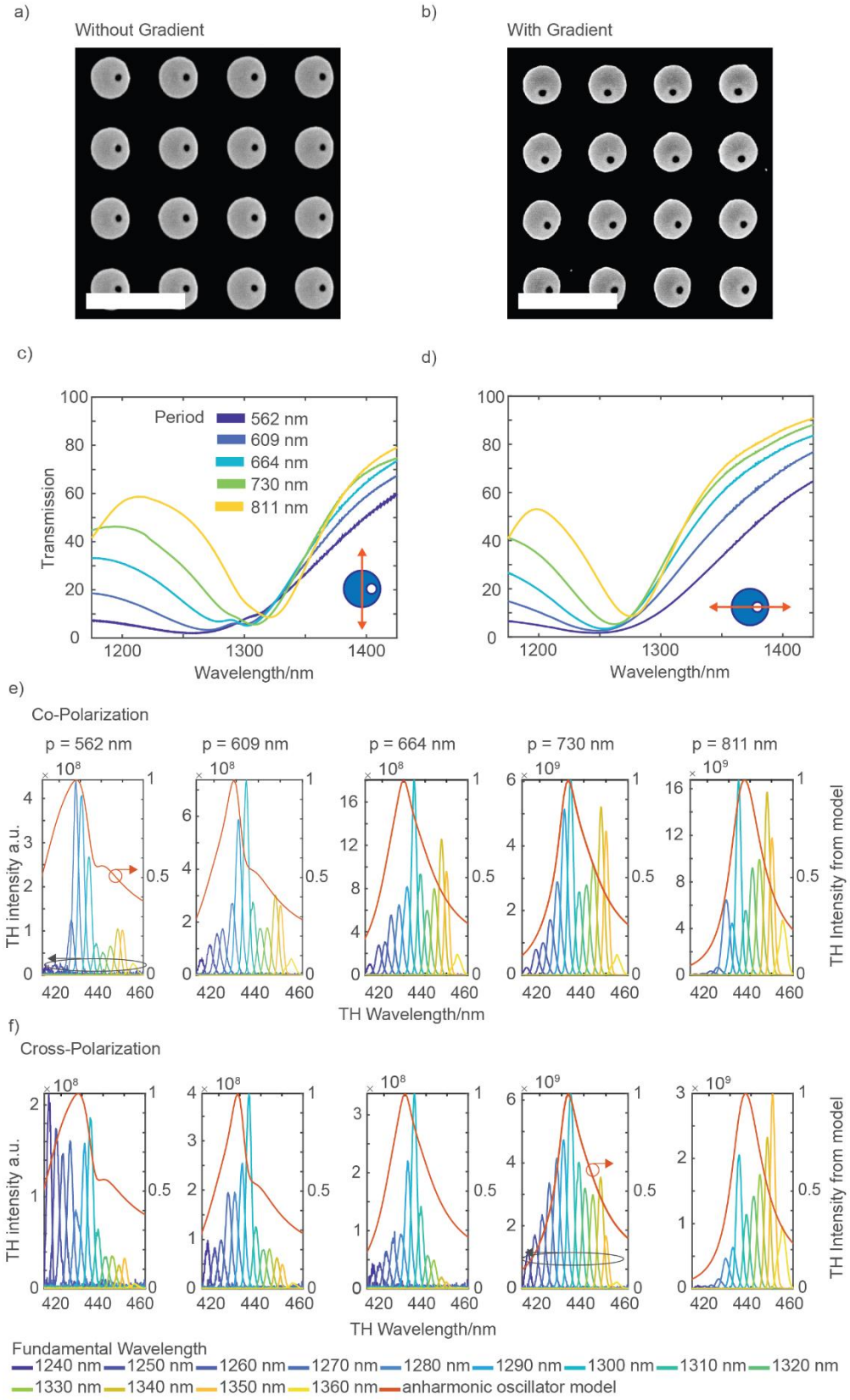


Figure 42. a,b) SEM images of the fabricated metasurfaces with and without blazed phase grating. Scale bar 1 μm . c,d) Experimentally obtained transmission spectra for vertically (c) and horizontally (d) polarized input light with wavelengths in the range of 1240-1360 nm for different unit cell sizes. e,f) Third harmonic intensity for fundamental excitations with wavelengths between 1240 nm and 1360 nm for different periods in (e) co- and (f) cross-circular polarization. The red curves show the overall nonlinear response of an anharmonic oscillator model, with the fitting parameters of the model extracted from the linear transmission spectra in Figure 42c [97].

We change the fundamental pump wavelength between 1200 nm and 1350 nm during the experiment, but the average laser power remained at 50 mW. We used a 50-mm achromatic lens optimized for the infrared range to focus the laser light on the metasurface. The resulting beam waist is about 45 μm . Therefore, the average pump peak power density is $0.32 \text{ GW}/\text{cm}^2$. We apply a 50x microscope objective with a numerical aperture of 0.42 to collect the generated third harmonic light from the metasurface. To capture the Fourier Plane of the objective, we use a set of two lenses and image the Fourier plane on an imaging spectrometer. With the imaging spectrometer (Andor Shamrock 303 equipped with an iDUS 420 detector, spectral resolution of the setup is 1.44 nm), we can resolve the wavelength of the frequency-converted light and different diffraction orders orthogonal to the diffraction grating. Using a set of quarter wave plates and polarizers in front of the specimen and behind the microscope objective, one can prepare a co-and cross-polarization state, as explained in Chapter 4.6.

5.6 Nonlinear Measurements

Figure 42e to f show the TH measurement results of the metasurfaces without phase gradient for different periods in the co- or cross-polarization state. The red plot in Figure 42e to f represents the TH response of the anharmonic oscillator model, which is discussed later. The measurements were performed for the fundamental excitations in the wavelength range from 1240 nm to 1360 nm. The plots show that the intensity of the generated TH light is higher for co-polarization than for cross-polarization. Moreover, the total intensity of TH light increases with unit cell size for co-polarization and cross-polarization. The increase in TH intensity with a larger unit cell size associated with the decrease in the linewidth of the magnetic Mie resonance could be related to the increase in its quality factor. All nonlinear measurements show a broadband TH response of the metasurfaces accompanied by a peak a few times higher than the surrounding TH intensity. The spectral width (FWHM) of the TH light is 5 nm to 6 nm. It is possible to estimate the conversion efficiency from the TH intensity. An average pump beam power of $100.00 \pm 1.00 \text{ mW}$ (P_{in}) is measured with a power meter. One can estimate an average THG power of $0.14 \pm 0.02 \text{ }\mu\text{W}$ (P_{THG}) derived from the spectrometer data

after normalization to the beam path's optical components and the detector's quantum efficiency. We estimated the maximum achievable nonlinear conversion efficiency of the metasurfaces we fabricated to be $H_{\text{THG}} = \frac{\hat{P}_{\text{THG}}}{(\hat{P}_{\text{in}})^3} \approx 10^{-14} \frac{1}{W^2}$. The average power conversion efficiency is $\zeta_{\text{THG}} = 10^{-4} 1/W^2$ (for definitions see Chapter 2.6). Note that we assume that the TH pulse length is equal to the pulse length of the fundamental beam due to the low-quality factor ($Q \approx 40 - 50$) of the resonances and the low height of the metasurfaces compared to the wavelength of the fundamental excitation in its propagation direction. Moreover, a comparison with Table 2 shows that the nonlinear conversion efficiency $\hat{\eta}_{\text{THG}}$ is closer to what would be expected from a Mie resonance instead of a QBIC. Note that the estimated efficiency is based only on the zeroth diffraction order of the two-dimensional metagrating. Since the TH wavelength is smaller than the unit cell period, higher diffraction orders are expected. The higher diffraction orders occur at an angle greater than 45° and are therefore not detected by the microscope objective since the numerical aperture only allows the detection of light within a cone of 24° . It is worth noting that the maximum THG efficiency (at zero-order) of the metasurface is $\hat{\eta}_{\text{THG,lin}} = \frac{\hat{P}_{\text{THG}}}{(\hat{P}_{\text{in}})^3} \approx 10^{-13} \frac{1}{W^2}$ ($10^{-3} \frac{1}{W^2}$ is the average efficiency) when the metasurface is illuminated with a vertically polarized fundamental beam. Since a circularly polarized fundamental beam has a vertical and a horizontal component and one loses 50% of the power during excitation, the TH nonlinear conversion efficiency is $\sim \left(\frac{1}{2}\right)^3 = \frac{1}{8}$ times weaker for circular polarization compared to linear polarization. Compared to an unpatterned silicon layer of the same thickness, the patterned metasurface shows 10,000 times higher TH intensity when illuminated with a linearly polarized fundamental excitation.

5.7 Coupled Harmonic Oscillator Model

In this section, the metasurface's linear and nonlinear optical properties are investigated in the framework of a classical coupled anharmonic oscillator model, since the numerical and experimental results show a significant difference between them. As shown previously, the numerically determined linear transmission spectrum shows a defined peak with a narrow linewidth related to the QBIC. However, this property is not present in the experimental linear transmission. While the nonlinear numerical results show a strong THG due to the presence of the QBIC, the experimentally determined THG response exhibits a broadband behavior that coincides with the transmission dip, as shown previously. To better evaluate the discrepancy, we employed the toy model of the coupled anharmonic oscillator [98, 99]. The model consists of two oscillators, one of which represents the magnetic Mie mode (with an oscillator amplitude of x_D), which can interact with an external electromagnetic field f_1 and couples to free space. On the other hand, we define the oscillator strength of the BIC mode as x_B . This mode cannot couple to free space since it is assumed to be a dark mode but can only couple

to x_D . This configuration is called the Fano resonant regime which is realized in the coupled oscillator model if only one resonator is driven where the damping of the resonator is larger than the coupling constant [100]. With these assumptions, the two coupled differential equations for the anharmonic oscillator model are as follows:

$$\begin{aligned}\ddot{x}_D + 2\gamma_D \dot{x}_D + \omega_D^2 x_D - kx_B + \alpha x_D^3 &= -f_1 \\ \ddot{x}_B + 2\gamma_B \dot{x}_B + \omega_B^2 x_B - kx_D + \alpha x_B^3 &= 0\end{aligned}$$

74

Where $x_{D/B}(t)$, $\gamma_{D/B}$ and $\omega_{D/B}$ represent the amplitude, linewidth, and resonance frequency of the Mie mode and the BIC, respectively, and k is the coupling constant between the oscillators. The third-order nonlinear response of this model is given by the anharmonic term αx_D^3 , where α is the nonlinear coefficient. To solve the coupled equations, one can use a Taylor expansion as follows:

$$\begin{aligned}x_D(t) &= x_{D,0} + \alpha x_{D,1} + O(n^2) \\ x_B(t) &= x_{B,0} + \alpha x_{B,1} + O(n^2)\end{aligned}$$

75

Here, $x_{D/B,0}$ represents the solution of the classical coupled harmonic oscillator, while $x_{D/B,1}$ are the first-order correction terms that describe the nonlinear response of both oscillators, as will be shown later. If we insert the Taylor expansion 75 into the system of coupled equations 1 and compare the terms of the same order ($x_{D/B,0}$ vs. $x_{D/B,1}$) of the perturbation parameter α in both equations, we find that the anharmonic oscillator model splits into two sets of differential equations. One describes the linear response of the coupled harmonic oscillator, and another set of equations describes the nonlinear response. The system of equations for the first is given by:

$$\begin{aligned}\ddot{x}_{D,0} + 2\gamma_D \dot{x}_{D,0} + \omega_D^2 x_{D,0} - kx_{B,0} &= -f_1 \\ \ddot{x}_{B,0} + 2\gamma_B \dot{x}_{B,0} + \omega_B^2 x_{B,0} - kx_{D,0} &= 0\end{aligned}$$

76

While the nonlinear response is given by:

$$\ddot{x}_{D,1} + 2\gamma_D \dot{x}_{D,1} + \omega_D^2 x_{D,1} - kx_{B,1} = x_{D,0}^3$$

$$\ddot{x}_{B,1} + 2\gamma_B \dot{x}_{B,1} + \omega_B^2 x_{B,1} - kx_{D,1} = x_{B,0}^3$$

77

From the decoupled systems of equations 76 and 77, one can see that the linear coupled harmonic oscillator drives the nonlinear oscillation in equations 77. To calculate the nonlinear response, one must first calculate the linear response from the system of equation 76, which serves as the source for the nonlinear response in equation 77. Therefore, we first give the solution to the system of equations 76. The solution can be calculated by a Fourier Transformation. In the frequency domain, equation 76 transforms to:

$$\frac{1}{(w_D^2 + i\gamma_D \omega - \omega^2)} x_{D,0} + kx_{B,0} = -f_1$$

$$\frac{1}{(w_B^2 + i\gamma_B \omega - \omega^2)} x_{B,0} + kx_{D,0} = 0$$

78

Therefore, the linear oscillator strength of $x_{D,0}$ and $x_{B,0}$ to the linear coupled harmonic oscillator is given by:

$$x_{D,0} = \frac{w_B^2 + i\gamma_B \omega - \omega^2}{(w_D^2 + i\gamma_D \omega - \omega^2)(w_B^2 + i\gamma_B \omega - \omega^2) - k^2} f_1$$

$$x_{B,0} = \frac{k}{(w_D^2 + i\gamma_D \omega - \omega^2)(w_B^2 + i\gamma_B \omega - \omega^2) - k^2} f_1$$

79

From the equations 79, several observations can be made. First, the amplitude of $x_{D,0}$ is modified around the resonance frequency of the oscillator $x_{B,0}$. Second, in the case of $\omega_{D,0} = \omega_{B,0}$, the lineshape of $x_{D,0}$ is symmetric and when they are detuned from each other, an asymmetric lineshape arises composed of a local minimum and maximum. This is a signature of a Fano-like resonance. Third, the amplitude and its modulation depth increase with an increased coupling constant k . The solution of the nonlinear coupled oscillator equation 77 can be found by a Fourier Transform too. In the frequency domain, equation 77 becomes as follows:

$$\frac{1}{(w_D^2 + i\gamma_D\omega - \omega^2)} x_{D,1} + kx_{B,1} = F[x_{D,0}^3]$$

$$\frac{1}{(w_B^2 + i\gamma_B\omega - \omega^2)} x_{B,1} + kx_{D,1} = F[x_{B,0}^3]$$

80

Therefore, the nonlinear oscillator strength of the nonlinear coupled anharmonic oscillator is given by:

$$x_{D,1} = \frac{1}{1 - k^2 g_D^2 g_B^2} (g_D F[x_{D,0}^3] - k^2 g_B^2 F[x_{B,0}^3])$$

$$x_{B,1} = \frac{1}{1 - k^2 g_D^2 g_B^2} (g_B F[x_{B,0}^3] - k^2 g_D^2 F[x_{D,0}^3])$$

81

Equation 81 gives the nonlinear response of the anharmonic oscillator model, where $g_{B/D} = (w_{D/B}^2 + i\gamma_{D/B}\omega - \omega^2)$. The equations for $x_{B,1}$ and $x_{D,1}$ consists of two terms. The first term $g_{D/B} F[x_{D/B,0}^3]$ describes the nonlinear response of the Mie or BIC mode in response to the linear oscillation of it. The second term $k^2 g_{D/B}^2 F[x_{B/D,0}^3]$ describes the energy transfer from one oscillator to the other.

5.8 Model Results

To relate the model of the anharmonic coupled oscillator to the numerical and experimental results in the linear and nonlinear optical domain, we need to relate solution 79 to the experimentally and numerically determined transmission values. The model of the coupled anharmonic oscillator described above depends on several parameters, such as the resonant frequency and linewidths of both modes and the coupling constant between them. One way to derive the model parameters from the numerical values is to use the extinction spectra [98, 99]:

$$\alpha(\omega) = f_1 \omega \operatorname{Im} \left(\frac{(-\omega^2 - \omega_a^2 + 2i\gamma_a\omega)^{-1}}{1 - k^2 (-\omega^2 - \omega_a^2 + 2i\gamma_a\omega)^{-1} (-\omega^2 - \omega_b^2 + 2i\gamma_b\omega)^{-1}} \right) + \alpha_0$$

82

At the same time, the extinction spectra can be calculated from the experimentally and numerically obtained transmission spectra T as [98]:

$$\alpha(\omega) = -\ln(T)$$

83

Therefore, it is possible to convert the transmission spectrum into the corresponding extinction spectrum using Equation 83, and the spectrum obtained can be used for fitting with equation 82. From the fit, the values for the coupling constant, resonance frequency, and linewidth of the Mie mode and BIC can be derived. The parameters are listed in Table 1. Note that we fitted the model to the transmission of vertically polarized light since the QBIC resonance should only appear for a vertical polarization, as evident from Figure 39d and Ref. [90].

Table 6. Model parameters of the coupled anharmonic oscillator model. The parameters were obtained by fitting the numerically and experimentally achieved transmission spectra using equations 82 and 83. Note that the values in the table are converted from frequency values to wavelength for better comparison with Figure 39b and Figure 42c.

	p [nm]	ω_d [nm]	γ_d [nm]	ω_B [nm]	γ_b [nm]	k [nm]
Experimental spectra (Figure 42c)	563	1263	49	1307	12	19
	609	1276	42	1296	11	22
	664	1290	39	1294	11	21
	730	1301	32	1296	19	20
	811	1313	39	1315	23	32
Simulation (Figure 39b)	664	1300	25	1320	0.1	16

Therefore, the nonlinear response of the metasurfaces can be estimated from the extracted values of $\gamma_{D/B}$, $\omega_{D/B}$, and k from the fit of the extinction spectra obtained experimentally from the transmission spectra shown in Figure 42c.

Figure 42e-f show the relationship between the experimentally observed TH response for a range of wavelengths for co- and cross-polarized configurations and the corresponding TH response from the model calculation, $I_{THG} = |x_{D,1} + x_{B,1}|^2$ (red curve). The model qualitatively mirrors the experimentally observed broadband nonlinear response by considering only the linear optical properties of the system. However, from a quantitative point of view, the model may not provide a good estimate because it does not consider the transmission and reflection of the oscillator but only the oscillator strength. Further, the

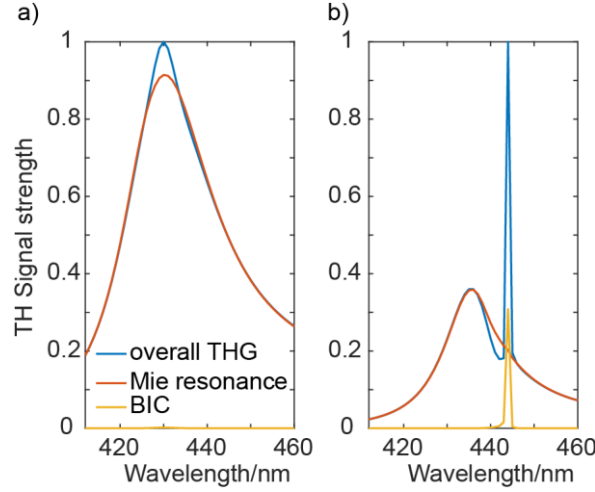


Figure 43. Plots of the TH oscillator strength as estimated from the anharmonic oscillator model for the experimentally obtained linear transmission spectrum for a period of 664 nm (a), shown in Figure 42c, and for the simulated spectrum for the same period as shown in Figure 39b. The overall TH signal $I_{THG} = |x_{D,1} + x_{B,1}|^2$; $I_D = |x_{D,1}|^2$ and $I_B = |x_{B,1}|^2$ are the contributions from the magnetic Mie mode and the BICs, respectively. The plots are normalized to the maximum oscillator strength of I_{THG} [97].

model parameters are obtained from the measured linear transmission. In addition, the model describes the metasurfaces as a single coupled oscillator, but the metasurface itself has many resonators. Therefore, small geometric changes that may leave the overall transmission unchanged can significantly affect the nonlinear properties. Moreover, the nonlinear susceptibility of the material is not considered in this model, but only the nonlinear behavior due to the resonance itself. As a result, there are discrepancies between the model and the experimental data. However, the model helps us to understand the nonlinear behavior because it allows us to separate the nonlinear contributions of the Mie resonance and the BIC and to reduce a complicated behavior to six model parameters.

To understand the response of the model, we discuss exemplarily the metasurface with a period of 664 nm, but the behavior is the same for all fabricated metasurfaces. The linear fitting reveals that the resonance wavelengths corresponding to the resonance frequencies ω_D and ω_B , are in the broad transmission dip (1287 nm), and the asymmetric shoulder (1293 nm) of the transmission spectrum, respectively. The linewidth of the Mie resonance and the BIC are estimated to be 52 nm and 12 nm, respectively. Figure 43a shows the overall THG response from the model and the individual contributions from $x_{D,1}$ and $x_{B,1}$ for the experimentally obtained data. One can see that the Mie resonance dominates the nonlinear response $x_{D,1}$, while $x_{B,1}$ plays only a minor role in the experiment, since the pump excites mainly $x_{D,1}$. Similar results can be estimated for the other experimentally obtained transmission spectra, and in every case, the nonlinear response of the Mie resonance $x_{D,1}$ dominates the overall nonlinear response of the anharmonic coupled oscillator model. In the

case of the numerical simulations, the nonlinear response is dominated by the response of the BIC $x_{B,1}$.

On the other hand, one can fit the anharmonic oscillator model to the numerically obtained transmission values, as shown in Table 6, the resonance wavelength ω_D obtained from the fit appears to be 1300 nm which agrees with Figure 39b. Further, the spectral position of ω_B appears to be 1320 nm, which corresponds to the sharp peak in Figure 39b. The linewidth γ_D appears to be 25 nm and $\gamma_B = 0.1 \text{ nm}$, which leads to a Quality factor of the mode x_B of 13.200, which agrees with the assumption that the dark mode x_B is a BIC mode [86]. Further, the coupling constant is smaller than γ_D which gives a connection of the coupled harmonic oscillator model to the Fano resonant regime [81, 100]. In this case, the nonlinear response of the model, as shown in Figure 43b of the coupled anharmonic oscillator, is dominated by the BIC mode, and the TH response shows a sharp peak at the position of ω_B , which originates from x_B . Further a broader “background” TH is visible which originates from magnetic Mie resonance x_D .

To link the numerical results with the experiments, we varied the linewidth γ_B of the BIC while keeping the other model parameters constant. Figure 44a shows the transmission

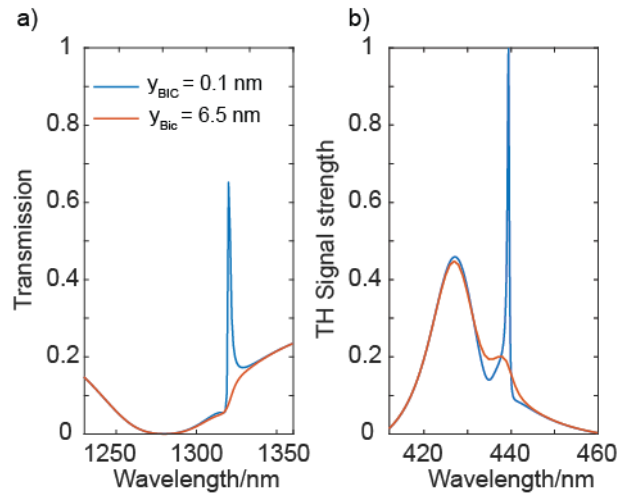


Figure 44. a) Linear transmission as calculated from the anharmonic oscillator model. We extracted the parameters for the model from the simulated transmission values in Figure 1d. However, the linewidth γ_B of the BIC was varied from 0.1 nm to 6.5 nm. b) the corresponding nonlinear oscillator strength for 0.1 nm and 6.5 nm linewidth [97].

values of the model if the linewidth γ_B is changed from 0.1 nm to 6.5 nm. With a linewidth of 0.1 nm, the anharmonic oscillator model shows a sharp transmission peak at 1320 nm, as expected from the numerical results. However, when the linewidth increases from 0.1 nm to

6.5 nm, the transmission peak decreases, and the peak becomes a shoulder in the transmission dip of the mode x_D . This observation agrees with the experimentally determined transmission values of the metasurface for different periods in Figure 42c. The decrease in visibility of the QBIC peak is related to a decrease in the TH response of the nonlinear oscillator strength $x_{B,1}$, as shown in Figure 44b. Figure 44b shows a pronounced peak in the overall TH response related to the THG of the BIC $x_{B,1}$. However, by increasing the linewidth γ_B to 6.5 nm, the peak due to the BIC $x_{B,1}$ becomes insignificant and the nonlinear response of the whole system is dominated by $x_{D,1}$. That means a decrease in the quality factor of the BIC quickly deteriorates its TH response.

In summary, this model shows good qualitative agreement with the experimental and numerical results and predicts that the Mie mode is the main contributor to the overall TH response of the system. Moreover, this assumption also agrees with the experimentally determined conversion efficiency. In the nonlinear experiments, the conversion efficiency is of the order of $10^{-14} 1/W^2$. This conversion efficiency is comparable to the conversion efficiency reported in the literature for magnetic Mie resonances (see Table 2), while QBIC resonance enhances the TH conversion efficiency by orders of magnitude.

Moreover, the experimentally obtained transmission shows a significant change in the resonance frequency of the Mie resonance, as shown in Figure 42c and d, compared to the simulations in Figure 41b, even though the average size of the cylinders in every fabricated Metasurface is similar. Moreover, the change in the material properties seems to increase with decreasing unit-cell size. In addition, the anharmonic oscillator model predicts increased losses in the material with decreasing unit-cell size. Therefore, it looks like the losses depend on the density of the nanoresonators on the Metasurface. It appears that higher densities of resonators lead to more losses, suggesting that the losses may occur during a fabrication step in which the damage to the material depends on the density of the resonators. Possible steps are electron beam lithography, since the amount of scattered high-energy electrons in the material is higher, or reactive ion etching, since it is a chemical process that depends on the density of the structures. It is known from previous work that reactive ion etching can distort the material structure and introduce lossy surface states that increase the absorption of the material [99, 101]. It is already known that this mechanism broadens the Fano resonances in metasurfaces. In addition, a strong increase in absorption also leads to a change in the refractive index of the material since the Kramers-Kronig relationship links absorption and refractive index [3]. Since it is difficult to estimate the extent of the change in refractive index and absorption, we can only make a qualitative statement about the influence of various factors. However, the increased absorption does not appear to be the only mechanism playing a role in the low visibility of the QBIC. Another influence may come from the unavoidable manufacturing variations in nanofabrication, as explained in chapter 5.9.

Other reasons for the losses occurring in the system are due to symmetry breaking compared to the experiment. First, the nanoresonator array must be fabricated on a substrate, which breaks the symmetry of the metasurface in the direction of light propagation. However, the system was simulated by considering a substrate, so, the losses due to this asymmetry were already considered. However, since the simulation of the entire metasurface was not feasible, only the unit cell of the design was investigated numerically. A real metasurface has a limited size and therefore the translational symmetry is broken at the edge of the metasurface. Therefore, the radiation from the vertical magnetic dipole forming the BIC is no longer suppressed and thus a radiation channel opens. It has already been shown that the quality factor of the QBIC resonance increases with the size of the metasurface [81]. This is because for larger metasurfaces, the ratio of nanoresonators located inside the metasurface to nanoresonators located at the edge of the metasurface improves with the size of the metasurface, as the ratio of area to circumference also increases with the size of the metasurface. However, the metasurface used in Ref. [53] has a quality factor of $Q > 1000$ and a linewidth of less than 1 nm, while the metasurface size is only $25 \times 25 \mu\text{m}^2$. In addition, they use rectangular nanostructures but also target a vertical magnetic dipole to create a QBIC resonance. Working QBIC metasurfaces with quality factors around 200 have been successfully realized with metasurface sizes ranging from $50 \times 50 \mu\text{m}^2$ to $200 \times 200 \mu\text{m}^2$ [53, 81, 89, 102].

5.9 Influence of fabrication tolerances

The linear experiments and the model show a substantial broadening of the Mie resonance for smaller periods. On the other hand, the measured THG intensity decreases for metasurfaces with a smaller period. This indicates that the absorption of the material increases with smaller periods. On the other hand, the Mie resonances for the metasurface with 730 nm and 811 nm periods show a very narrow linewidth that is closer to the linewidth observed in the simulations. However, the QBIC resonance is not observable even for this metasurface. The different observations in the experiment and the model suggest that there may be different mechanisms that may broaden the BIC, which are summarized in two parameters in the anharmonic oscillator model: The line width of the Mie resonance and the line width of the BIC. However, the broadening of the linewidth can have two causes: a homogeneous broadening due to material and scattering losses, and an inhomogeneous broadening where variation in geometry changes the resonant frequency and the average linewidth over all resonators becomes wider than the resonance when each resonator has the same size [3].

To account for the inhomogeneous broadening, I adapted a method from Ref. [102]. In their work, they simulate the metasurface unit cell supporting QBIC resonances for different geometric parameters and average the spectral response over the different geometries

according to a Gaussian distribution. The parameters of the Gaussian distribution, such as average magnitude and variance, are derived from the SEM image and analyzed using OpenCV in Python. Here we have used a similar approach, exemplified by the metasurface with a period of 664 nm, as shown in Figure 39a. As shown earlier, the two main parameters controlling the spectral position of the QBIC resonance, and the Mie resonance are the cylinder radius and the radius of the air hole. Due to nanofabrication, both parameters can vary. To determine the effect of the fabrication-induced variances on the transmission spectrum, one can simulate the spectrum of the unit cell for different combinations of air hole radius and cylinder radius. We used the value of the air hole radius and the cylinder radius around their respective average values, $\tilde{r}_c = 183 \text{ nm}$ in the case of the cylinder and $\tilde{r}_H = 23 \text{ nm}$ in case of air hole. Here I swept the radius r_c of the cylinder (radius r_H , air hole) from 165 nm (10.4 nm, air hole) to 200 nm (39.4 nm, air hole) in steps of 0.2 nm (0.2 nm, air hole). The obtained spectra are then averaged according to the two-dimensional Gaussian distribution with standard deviations σ_c and σ_H [103]:

$$f_X(r_c, r_H) = \frac{1}{2\pi\sigma_c\sigma_H\sqrt{1-k^2}} \exp\left(-\frac{1}{2(1-k^2)}\left[\frac{(r_c - \tilde{r}_c)^2}{\sigma_c^2} + \frac{(r_H - \tilde{r}_H)^2}{\sigma_H^2} - \frac{2k(r_c - \tilde{r}_c)(r_H - \tilde{r}_H)}{\sigma_H\sigma_c}\right]\right)$$

84

Where X represents the set of all possible combinations of (r_c, r_H) and k denotes the correlation between r_c and r_H , and we assume here that the correlation $k = 0$. Note that this may not be the case depending on the nanostructure's geometry and manufacturing method. Figure 45a shows the average transmission spectra for different standard deviations of the geometric variation from 0 nm to 2 nm, where for simplicity, $\sigma = \sigma_c = \sigma_H$. The spectral position of the Mie resonance and the QBIC does not change with increasing standard deviation and is at about 1300 nm and 1325 nm, respectively. Moreover, the linewidth of the Mie resonance does not increase much with the standard deviation and remains around 30 nm because the standard deviation σ is much smaller than the linewidth of the Mie resonance. However, the visibility of the QBIC resonance decreases with increasing standard deviation σ . Even small

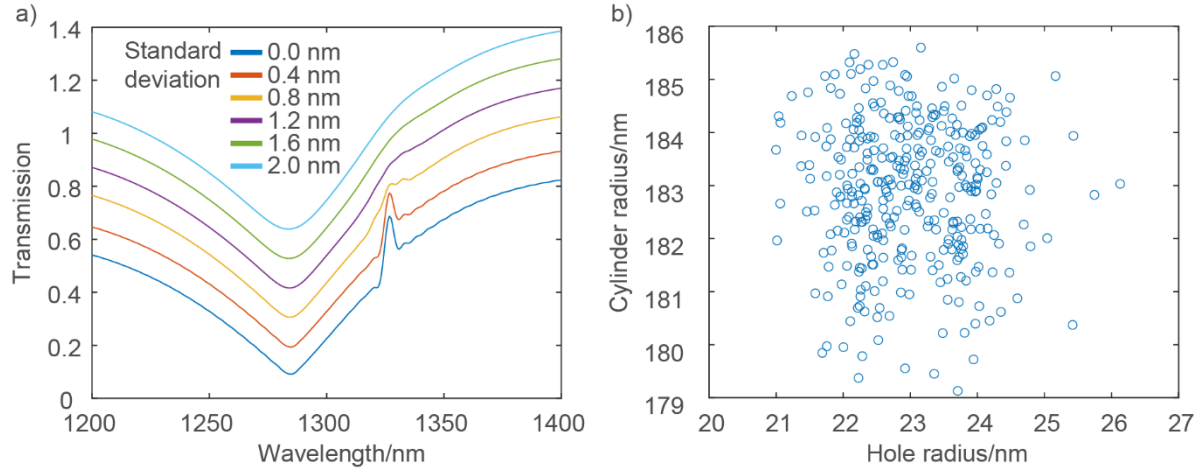


Figure 45. a) Numerically determined averaged QBIC resonance spectra for the nanocylinders designs for different standard deviation values for the geometric variation from $\sigma = 0$ to $\sigma = 2$ nm. Even for small standard deviations of 0.8 nm, the visibility of the QBIC resonance is greatly reduced. b) Scatter plot of the different metasurface with 664 nm period for the hole radius and the cylinder radius.

standard deviations of only $\sigma = 1$ nm strongly influence the QBIC resonance and lead to a broadening where the visibility of the QBIC resonance decreases. At larger standard deviations, the QBIC resonance becomes a broad shoulder in the transmission dip of the Mie resonance before disappearing completely. This broadening is qualitatively similar to what can be seen in the linear transmission obtained experimentally. Note that the transmission spectra do not quantitatively agree with the experimentally measured transmission spectrum since other effects in the fabrication chain may also influence the material's refractive index, as explained above. For this simulation, we used the refractive index shown in Figure 7. Furthermore, these results agree with those from Ref. [102]. Here, a similar effect of fabrication tolerances on the visibility of the QBIC resonance was found. However, Kühne et al. used other nanoresonator designs. The QBIC resonance was still visible even at larger standard deviations of the geometry parameters of up to 2 nm to 3 nm, and the decrease in QBIC resonance visibility is different for different nanoresonator designs.

This analysis was performed for arbitrary standard deviations. However, to understand how strong the influence of manufacturing tolerances is, we estimate the standard deviation from several SEM images by a circle-Hough transformation in Matlab. To estimate the radii and their standard deviations, we first convert the grayscale SEM images to black and white images and then use the circle-Hough algorithm to derive the radii of the air holes and cylinders. However, the process has uncertainties. First, the imaging quality is affected by the lens aberration in the SEM optics, which leads to an enlargement of the objects at the image corners and thus to an increased size of the nanostructures, while the objects in the center remain almost unchanged. Second, the position of the electron beam changes slightly due to the charging of the sample and distorts the image. Due to this, we may overestimate the

standard deviation of the radii. However, the obtained radii pairs (r_C, r_H) can be plotted in a scattering plot in Figure 45b. From the scattering plot, one can derive the average values, $\tilde{r}_C = 183 \text{ nm}$ in the case of the cylinder and $\tilde{r}_H = 23 \text{ nm}$ in the case of the hole. The standard deviations are $\tilde{r}_C = 1.5 \text{ nm}$ in the case of the cylinder and $\tilde{r}_H = 3.5 \text{ nm}$. The values of the standard deviations are close to the value of 1.5 nm, at which the QBIC resonance is no longer observable.

5.10 Diffraction Efficiency

To analyze the behaviour of a metasurface, it is interesting to consider a blazed step phase grating, as it provides an easy model of how the geometry parameter, e.g., the period of the metasurface, affects the geometric phase itself and what constraints exist. The phase grating is illustrated in Figure 46; it has N equidistant phase steps of $2\pi/N$. Here p is the period of the unit cell and every step has a size of $p = d/N$, where d is the period of the blazed phase

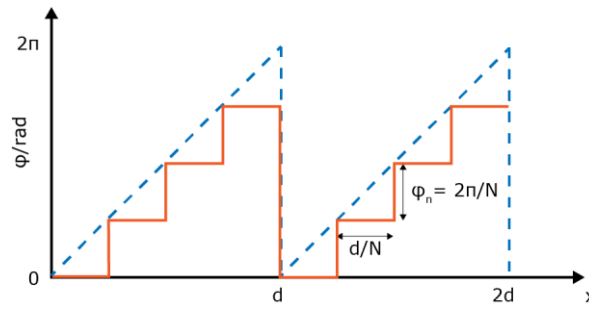


Figure 46. Phase profile of a stepped blazed grating with a period of d which consisting of N equidistant phase steps ϕ_n . In this example $N = 4$.

grating. Each phase step n of the stepped blazed grating is given by $\phi_n = (n - 1) \frac{2\pi}{N}$ and we assume that every step can be approximated as an independent scatterer. The diffraction angle of a blazed grating can be calculated from equation 59 in chapter 4.4. The transmission of such a stepped blazed grating from each element n is given as follows:

$$t_n(x) = e^{i\phi_n}$$

85

Where $\phi_n = 2\pi(n - 1)/N$ is the constant phase steps. Here we assume that each element transmits or generates the same amount of light. We also assume no "shadowing effect" of the metasurface, i.e., each element emits unobstructed light over the entire unit cell of the phase step. Chapter 4.12 indicates that this effect is negligible in the nonlinear domain since

the nonlinearly generated light is passed almost vertically through each nanoresonator on the metasurface, as shown in Figure 29g and h.

However, when the grating is excited by light, the phase grating generates third harmonic light with an abrupt phase change from element to element, and the third harmonic light is diffracted into multiple diffraction orders. We showed that diffractive optical elements can be constructed and analyzed by a Fourier transform, but since a blazed diffraction grating is a periodic structure, instead of an continuous Fourier transform, one decompose the diffraction grating into a Fourier series, which is easier to analyze [104]. Here, the diffraction efficiency for each order of the stepped blazed grating can be determined by analyzing the Fourier series of the stepped blazed grating and its Fourier coefficient c_q [104, 105]:

$$p_k = |c_q|^2 = \left| \frac{1}{d} \int_0^d e^{-i\phi_n} e^{2\pi i k \frac{x}{d}} dx \right|^2 \quad 86$$

Since ϕ_n are constant steps, it is possible to split the integral into several integral over the different constant steps [106]:

$$p_k = \left| \sum_{n=0}^{N-1} \int_{n/d}^{(n+1)/d} e^{-i\phi_n} e^{2\pi i k x'} dx' \right|^2 \quad 87$$

Further, we can use the mathematical identity [106]: $\sum_{m=0}^{N-1} \exp(-\frac{2\pi i}{N} Am) = \frac{\sin(\pi A)}{\sin(\frac{\pi A}{N})}$ to simplify equation 87:

$$p_k = \left[\frac{\sin\left(\frac{\pi k}{d}\right)}{\frac{\pi k}{d}} \right]^2 \left[\frac{\sin\left(d(0.5\phi_1 - \frac{\pi k}{N})\right)}{d \sin\left(d(0.5\phi_1 - \frac{\pi k}{N})\right)} \right]^2 \quad 88$$

In total, the diffraction efficiency for the first diffraction order $k = 1$ is given by:

$$\eta = \left(\frac{\sin\left(\frac{\pi}{N}\right)}{\frac{\pi}{N}} \right)^2$$

89

From this equation, it can be seen that the diffraction efficiency increases with the number of phase steps. Thus, as the phase resolution increases, the diffraction efficiency also increases. However, since we use discrete nanoresonators to build a metasurface for wavefront control, we cannot decrease the spacing arbitrarily. First, we cannot allow the individual elements to overlap. Second, since the nanoresonators have an evanescent field that decreases exponentially outside the resonator, decreasing the distance of the nanoresonator leads to increasing near-field coupling between the resonators, which changes the properties of the resonance, such as its frequency and phase relationship. Since each resonator has a different angle of rotation from its neighbor, the coupling strength between the individual elements varies, which has a negative effect on the nonlinear geometric phase. Part of this work was to determine the practical consequences of this behavior. As shown before, the period seems to influence the phase relation, which would make the period a good parameter to improve the diffraction efficiency.

We fabricated a metasurface resembling a blazed-phase grating by using the geometric phase principle for experimental realization. We added a rotation from unit cell to unit cell by 22.5° in the x-direction to realize the phase steps ϕ_n of the stepped blazed grating. Therefore, a full rotation of 360° is covered by 16 unit cells, and a PB phase shift of 4π (8π) in co-polarization (cross-polarization) is achieved. Therefore, we realize a total phase change of 0 to 2π with $N = 16$ (8) steps in co-polarization (cross-polarization). Depending on the period, the diffraction orders appear at an angle of 4.64° (co-polarization) and 9.29° (cross-polarization) for a TH wavelength of 430 nm, with a maximum achievable diffraction efficiency of 98.72% in co-polarization and 94.96% in cross-polarization, according to equation 89 and the diffraction efficiency decreases with phase resolution.

5.11 Experimental Results

To experimentally realize the nonlinear phase tailoring properties, we studied the third harmonic generation from our metasurfaces with the phase gradient based on the geometric phase principle for different unit cell periods, resulting in beam deflection (for details, see Chapter 4.4). Since the phase gradient is similar to a phase blazed grating, the diffraction spots can be assigned to the individual phase gradients based on the phase factors of the geometric phase ($\pm 2\text{nd} \leftrightarrow \pm 4\alpha$, $\pm 1\text{st} \leftrightarrow \pm 2\alpha$). To resolve and measure the deflection of the third harmonic light, we imaged the Fourier plane of the microscope objective that gathers the light from the specimen. The obtained TH intensity in different diffraction orders and the estimated

diffraction efficiencies for co-polarization and cross-polarization are shown in Figure 47. The Fourier space image for the co-polarized TH light shows a prominent spot in the first diffraction order (at the desired angle) with small contributions in the 0th and 2nd diffraction orders. In contrast, the TH light appears mainly in the second diffraction order when cross-polarized. The zeroth-order diffraction spot in the center of the Fourier space carries no geometric phase.

However, we calculated the diffraction efficiency for a given diffraction order as the quotient of the intensity of this diffraction order I_x (marked by the dashed white lines), where x is the diffraction order and the total TH intensity I_{total} . In the co-polarization, the first diffraction order (proportional to 2α) appears with a very high diffraction efficiency ($\sim 90\%$) for periods from 664 nm to 811 nm, which is close to the theoretically possible value of 99.76%. In addition, the plots show that for a wide range of fundamental wavelengths, the high diffraction efficiency is maintained because the THG originates from the magnetic Mie resonance. However, at smaller periods (609 nm and 562 nm), the diffraction efficiency decreases dramatically due to the increase in near-field coupling strength between the neighboring nanoresonators. Moreover, the diffraction

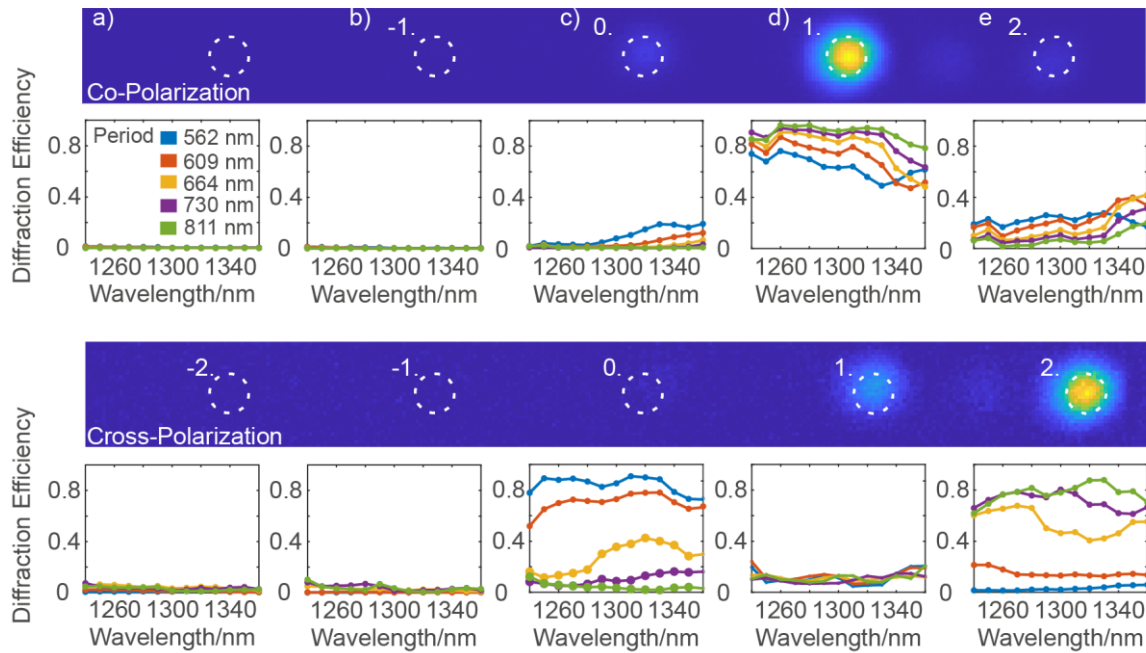


Figure 47. Diffraction efficiencies of TH light in different diffraction orders for different periods of phase gradient metasurface under excitation of fundamental beams with wavelengths from 1240 nm to 1360 nm in co- and cross-circular polarized configurations. The Fourier images above the diagrams of diffraction efficiencies are shown for a period of 811 nm and for a fundamental wavelength of 1300 nm. The first row shows the same for the co-polarized measurement, while the second row represents the cross-polarized measurement [97].

efficiency is negligible for the -1^{st} (Figure 47b) and -2^{nd} (Figure 47a) diffraction orders because the phase gradients appear like blazed gratings. The same trend of variation of diffraction efficiency is observed for the third harmonic in cross-polarization. In cross-polarization, the phase shift from unit cell to unit cell is 4α . As a result, the dominant diffraction occurs at the $+2^{nd}$ diffraction order (Figure 47e). In this case, we achieve a maximum diffraction efficiency of $\sim 75\%$ to 80% compared to a theoretically achievable diffraction efficiency of 94.96% . However, the overall diffraction efficiency is lower for the cross-polarization than for the co-polarized configuration. This is mainly because the TH phase changes at 4α for cross-polarization, while the phase changes at 2α for co-polarization, which decreases the phase resolution by a factor of 2. Subsequently, the diffraction efficiency decreases in cross-polarization compared to co-polarization.

5.12 Vortex Beam Array

To determine the functionality of our metasurface for applications, we developed a vortex beam array for realization at triple frequency, as discussed above. We chose a 3×3 array of vortices with different topological charges m to transform a Gaussian beam at the fundamental wavelength into an array of vortex beams at the TH wavelength. Considering the trade-off between conversion and diffraction efficiency described in Chapter 5.11, we designed and fabricated a geometric phase metasurface with a period of 664 nm . Taking advantage of the design freedom of the geometric phase principle, we have encoded two different vortex beam arrays in the co- and cross-polarization channels of the TH light (corresponding to phase factors of $2\sigma\alpha$ and $4\sigma\alpha$, respectively). The vortex beam array can be expressed by a Fourier series as follows:

$$T_{NDVG}^{(n\pm 1)\sigma\alpha} = \exp(i(n \pm 1)L_0\alpha) \sum_{m=-\infty}^{\infty} \sum_{n=-\infty}^{\infty} T_{mn}^{(n\pm 1)\sigma\theta} \exp\left(i\frac{2\pi}{T_x}(mx + ny) + i(mL_x + nL_y)\alpha\right)$$

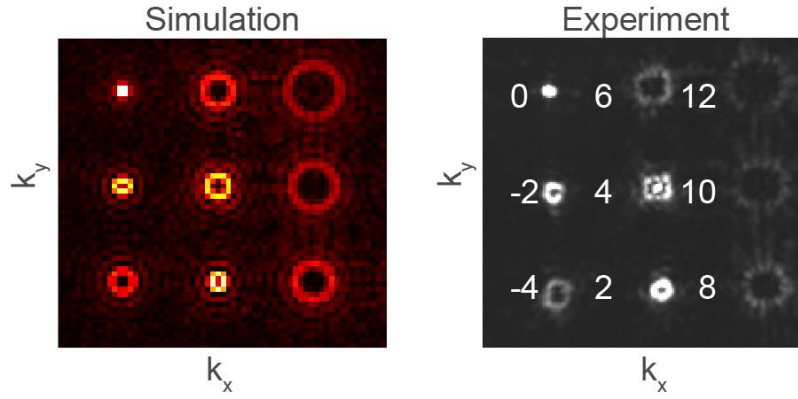
90

The topological charges are $L_0 = 2$, $L_x = 2$, $L_y = 6$ and n represent the harmonic generation order, 1 (for fundamental frequency) and 3 (for THG). Here, $(n-1)$ and $(n+1)$ describe the co- and cross-polarization configuration, respectively. The first point in the series expansion predicts the location of each diffraction order, which also relates to the generated frequency. The topological charges of each diffraction order follow the rule $L_0 + mL_x + nL_y$ for the $2\sigma\theta$ case and $2L_0 + mL_x + nL_y$ for the $4\sigma\theta$ case. For each diffraction order, the numerical aperture is $NA = \frac{\lambda}{T_x} \sqrt{m^2 + n^2}$, which changes with the TH wavelength. Then, the phase profile in co- and cross-polarization can then be determined by a computer-generated

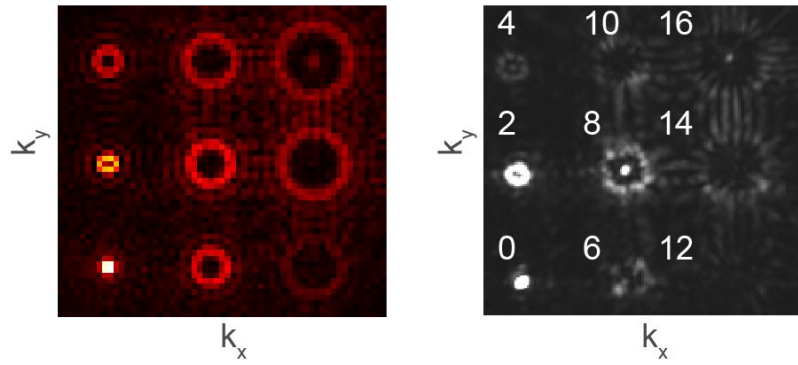
holography algorithm such as the Gerchberg-Saxton Algorithm or a genetic algorithm [107], using equation 90 as a target.

The experimental and numerical results for the generation of nonlinear optical vortex arrays with corresponding topological charges are shown in Figure 6. The measurement setup is the same as explained in chapter 4.6, but the spectrometer is replaced by Andor Zyla 4.2 sCMOS camera to record the image of the vortex beam. There is also a tiny spot in the center of the Fourier plane, which is visible in the experimentally reconstructed arrays. It comes from the rest of the TH light, which does not contain geometric phase information. Note that the vortex beams with high topological charges start to interfere (e.g., the vortex beams with topological charges 14 and 16 shown in Figure 48a and b), as all vortices are packed within an angular range of 17.46° ($NA = 0.3$). In addition, one can see that the measured vortex arrays have a minor speckle pattern, which is typical of pure phase holograms. When one inverts the polarization state of the background illumination, the metasurfaces generate the conjugate images due to the sign change of the circular polarization state in the phase factor of the TH signal. In addition, another vortex beam array at the fundamental wavelength was encoded by wavelength multiplexing. The reconstructed holographic image at the fundamental wavelength in the cross-polarization channel as determined by the linear PB phase principle (allowed only in cross-polarization) is given in Figure 48e and f. The vortex beam array at the fundamental wavelength is reconstructed within an angular range of 36.86° ($NA = 0.6$); therefore, the interference between different vortices is small. Again, the conjugate vortex beam can be reconstructed by reversing the polarization state. Careful observation reveals

a) Third Harmonic Wavelength



b)



c) Fundamental Wavelength

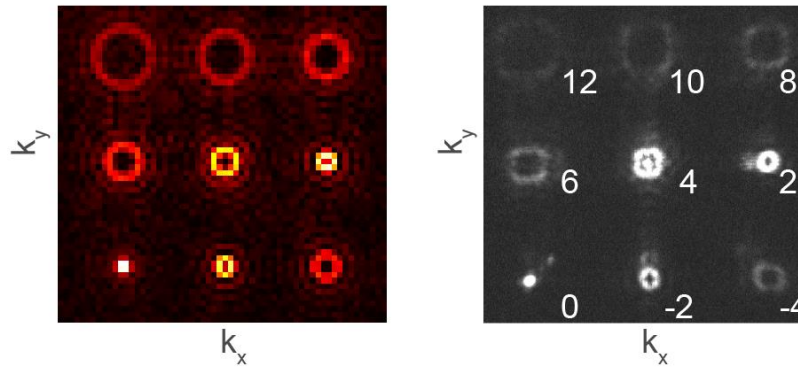


Figure 48. The left column shows the numerically determined vortex beam arrays with different topological charges at the TH wavelength for both polarization states: a) co-polarization and b) cross-polarization. The right column shows the experimentally reconstructed TH images in the Fourier plane, which resemble the numerically obtained arrays in a) co-polarization or b) cross-polarization. The numbers on the experimentally reconstructed images represent the topological charges of each generated vortex beam. c) shows the numerically simulated (left) and the experimentally measured (right) vortex beam arrays in cross-polarization at the fundamental wavelength [97].

that the individual vortex beams in an array produce ghost images due to internal reflections in the camera. The anti-reflection coating and the camera are designed for the visible spectral range. The ghost images are stronger for the vortex beam with low topological charges, e.g., for $m = -2$, because the intensity is concentrated on a smaller area of the camera sensor.

5.13 Conclusion

We show numerically and experimentally that a metasurface made of amorphous silicon nanoresonators can efficiently generate and shape TH light using Mie resonances and the geometric phase principle. The design achieves third-harmonic conversion efficiencies of up to 10^{-14} 1/W^2 when illuminated with circularly polarized fundamental laser light in a wavelength range of 1240 to 1360 nm. The numerical studies show that the design supports QBIC to enhance the nonlinear conversion efficiency. However, in the experiments, the main contribution to the nonlinear signal comes from the Mie resonances that are also present in this wavelength range. This is confirmed by the model of the coupled harmonic oscillator. The main reason for the dominance of Mie resonance is the low quality factor of QBIC mode, which is due to inaccuracies in the nanofabrication process, such as surface roughness and surface states formed by reactive ion etching. Therefore, it can be challenging to implement a QBIC resonance in an experiment since it is easy to over-or under-couple to modes with a very low linewidth. During the design process, one must keep in mind and account for broadening mechanisms, such as material-induced losses and variations in the QBIC resonance wavelength due to the variance in the geometry of the individual nanoresonators in the metasurface. However, a good design process for QBIC resonant metasurfaces must include a sensitivity analysis of the resonance for each factor. Note that due to the low visibility of the QBIC resonance, we can only make qualitative arguments for specific loss mechanisms, as material properties appear to change significantly during nanofabrication.

However, the metasurface provides high diffraction efficiency at the third harmonic wavelength based on the nonlinear geometric phase principle. Moreover, the principle of geometric phase can be used to encode a vortex beam array in the nonlinear generation process with high fidelity. However, since the Mie resonance was the main contributor to the nonlinear signal, the question of how the geometric phase affects the QBIC state was not investigated in the experiment. Nevertheless, the concept offers a path to obtain miniaturized nonlinear metadevices that can control light flow in applications which require a small spatial footprint.

Chapter 6 Outlook

In this work, we studied dielectric metasurfaces in terms of their third-order nonlinear geometric phase response. We have investigated whether one can encode an arbitrary phase profile into the third harmonic generation process and manipulate the light propagation in nonlinear optical metasurfaces. On the other hand, we tried to improve the nonlinear conversion and diffraction efficiencies of the nonlinear generation process to control the generation and propagation of third harmonic light.

These results are a prerequisite for applications where one wants to replace bulky classical optical elements to meet tight space constraints. In the linear domain, metasurfaces are investigated to replace optical components in systems such as smartphone cameras [108] or to couple light from a chip to a fiber and vice versa as integrated elements. The latter is becoming increasingly important as semiconductor manufacturers begin to integrate optical components directly onto their chips [5]. In the nonlinear domain, applications are limited. Although the efficiencies shown in this work represent the state of the art for metasurfaces, the overall third harmonic efficiency of the metasurfaces are lower than the conventional nonlinear crystals. Therefore, applications of nonlinear metasurfaces in areas like augmented reality or holography are not yet feasible. Even though that higher harmonic generation can have an advantage in this area since the nonlinear conversion process would allow to filter out “background” or stray light at the fundamental wavelength and enhancing the image contrast. Nevertheless, the nonlinear efficiencies are high enough that cheaper and smaller optical detectors can detect the generated light if the metasurface is pumped with a sufficiently high peak power. For this reason, nonlinear dielectric metasurfaces may find their first applications in femtosecond laser diagnostics, as ultrashort pulse lasers deliver high peak powers and often require nonlinear operations to measure the properties of their pulses [3]. Optical devices such as autocorrelators or FROG/GRENOUILLE measurement systems are quite large and difficult to integrate into a laser system with tight spatial constraints [109]. A nonlinear metasurface that is less than one micrometer thick and integrates multiple functions into a single device can perhaps be integrated into a laser system to monitor laser function in-situ without the need for another device on the optical table.

In addition, although optical computing is still a distant goal, it has already been shown that metasurfaces with high third-order susceptibility that support bound states in the continuum can modulate light with light. Here, a laser beam can shift the QBIC resonance because it can change the refractive index of the material, which can change the transmission at that pump wavelength and make the metasurface transparent to another beam at the pump wavelength. This nonlinear optical gating is the first step towards a nonlinear optical element that can switch light with light [110, 111].

Another application where nonlinear metasurfaces can have an impact is spontaneous parametric downconversion (SPDC). Spontaneous parametric downconversion is the opposite of second harmonic generation or higher harmonic generation. In this process, a photon with a fundamental frequency ω_F is split into several photons with lower frequencies. For example a photon can be split into two photons at frequencies ω_S and ω_I , called signal and idler, respectively [3, 4]. Compared to higher harmonic generation, where the fundamental and the higher harmonic must satisfy certain energy relations, SPDC has different constraints in terms of energy, while the phase matching condition in nanostructures is relaxed [112]. This is because the energy of the signal and idler photons is not fixed. For example, a photon with a fundamental wavelength of 400 nm can be split into two photons with a wavelength of 800 nm or into a pair where one photon has a wavelength of 300 nm and the other has a wavelength of 1200 nm, or infinite other combinations, since in Metasurfaces the phase matching condition is relaxed [112]. However, since all photon pair combinations are equally possible and one distributes a finite amount of energy over a vast space of possible photon pair combinations [3, 4]. Therefore, the efficiency of spontaneous parametric downconversion is limited. Metasurfaces can play a role here too, as the Mie resonances or BIC may be used to enhance SPDC at a particular wavelength. First examples of SPDC with nanoresonators and metasurface made of GaAs, GaP and lithium niobate have already been demonstrated [112–116]. However, in the future, one could combine the holographic functionality of geometric phase or Huygens metasurfaces with SPDC and realize various effects with these metasurfaces. In this context, it would be interesting to see if one can introduce a geometric or resonant phase into the SPDC process and steer the photons in a certain direction by phase manipulation. Since SPDC has no classical analogue and the photon pairs can be quantum mechanically correlated, it would be interesting to see what the consequences of phase control are in SPDC processes.

In summary, nonlinear metasurfaces are versatile for encoding information in a nonlinear process and for functional applications that are more challenging than generating higher harmonic light alone. Therefore, the research field of nonlinear optical metasurfaces continues to expand, and exciting applications are published every day.

Chapter 7 References

- [1] P. A. Franken and J. F. Ward, "Optical Harmonics and Nonlinear Phenomena," *Rev. Mod. Phys.*, vol. 35, no. 1, pp. 23–39, 1963, doi: 10.1103/RevModPhys.35.23.
- [2] M. D. Levenson, C. Flytzanis, and N. Bloembergen, "Interference of Resonant and Nonresonant Three-Wave Mixing in Diamond," *Phys. Rev. B*, vol. 6, no. 10, pp. 3962–3965, 1972, doi: 10.1103/physrevb.6.3962.
- [3] R. W. Boyd, *Nonlinear Optics*. London: Elsevier, 2020. [Online]. Available: <https://www.sciencedirect.com/science/book/9780128110027>
- [4] M. Fox, *Quantum optics: An introduction*. Oxford: Oxford University Press, 2014.
- [5] Intel, *Intel® Silicon Photonics: How Does It Work? | Intel*. [Online]. Available: <https://www.intel.com/content/www/us/en/architecture-and-technology/silicon-photonics/silicon-photonics-overview.html> (accessed: Apr. 18 2022).
- [6] J. Feldmann *et al.*, "Parallel convolutional processing using an integrated photonic tensor core," *Nature*, vol. 589, no. 7840, pp. 52–58, 2021, doi: 10.1038/s41586-020-03070-1.
- [7] EKSMA Optics, *FEMTOKITS FOR THIRD HARMONIC GENERATION OF FEMTOSECOND Ti:Sapphire LASER*. [Online]. Available: <https://web.archive.org/web/20210615130629/https://eksmaoptics.com/femtoline-components/femtoline-nonlinear-laser-crystals/femtokits-for-third-harmonic-generation-of-ti-sapphire-laser/>
- [8] G. Li *et al.*, "Continuous control of the nonlinearity phase for harmonic generations," *Nature Mater*, vol. 14, no. 6, pp. 607–612, 2015, doi: 10.1038/nmat4267.
- [9] C. Schlickriede *et al.*, "Imaging through Nonlinear Metalens Using Second Harmonic Generation," *Adv. Mater.*, vol. 30, no. 8, p. 1703843, 2018, doi: 10.1002/adma.201703843.
- [10] W. Ye *et al.*, "Spin and wavelength multiplexed nonlinear metasurface holography," *Nat. Commun.*, vol. 7, no. 1, p. 11930, 2016, doi: 10.1038/ncomms11930.
- [11] E. Almeida, O. Bitton, and Y. Prior, "Nonlinear metamaterials for holography," *Nat. Commun.*, vol. 7, no. 1, pp. 1–7, 2016, doi: 10.1038/ncomms12533.
- [12] S. Chen *et al.*, "Giant Nonlinear Optical Activity of Achiral Origin in Planar Metasurfaces with Quadratic and Cubic Nonlinearities," *Adv. Mater.*, vol. 28, no. 15, pp. 2992–2999, 2016, doi: 10.1002/adma.201505640.

- [13] M. Kauranen and A. V. Zayats, "Nonlinear plasmonics," *Nature Photon*, vol. 6, no. 11, pp. 737–748, 2012, doi: 10.1038/nphoton.2012.244.
- [14] V. Zubyyuk, L. Carletti, M. Shcherbakov, and S. Kruk, "Resonant dielectric metasurfaces in strong optical fields," *APL Mater.*, vol. 9, no. 6, p. 60701, 2021, doi: 10.1063/5.0048937.
- [15] T. Liu, R. Xu, P. Yu, Z. Wang, and J. Takahara, "Multipole and multimode engineering in Mie resonance-based metastructures," *Nanophotonics*, vol. 9, no. 5, pp. 1115–1137, 2020, doi: 10.1515/nanoph-2019-0505.
- [16] Y. Gao, Y. Fan, Y. Wang, W. Yang, Q. Song, and S. Xiao, "Nonlinear Holographic All-Dielectric Metasurfaces," *Nano Lett.*, vol. 18, no. 12, pp. 8054–8061, 2018, doi: 10.1021/acs.nanolett.8b04311.
- [17] L. Wang, S. Kruk, K. Koshelev, I. Kravchenko, B. Luther-Davies, and Y. Kivshar, "Nonlinear Wavefront Control with All-Dielectric Metasurfaces," *Nano Lett.*, vol. 18, no. 6, pp. 3978–3984, 2018, doi: 10.1021/acs.nanolett.8b01460.
- [18] S. Liu *et al.*, "Resonantly Enhanced Second-Harmonic Generation Using III–V Semiconductor All-Dielectric Metasurfaces," *Nano Lett.*, vol. 16, no. 9, pp. 5426–5432, 2016, doi: 10.1021/acs.nanolett.6b01816.
- [19] S. V. Makarov *et al.*, "Efficient Second-Harmonic Generation in Nanocrystalline Silicon Nanoparticles," *Nano Lett.*, vol. 17, no. 5, pp. 3047–3053, 2017, doi: 10.1021/acs.nanolett.7b00392.
- [20] Lei Xu *et al.*, "Dynamic Nonlinear Image Tuning through Magnetic Dipole Quasi-BIC Ultrathin Resonators," *Advanced Science*, vol. 6, no. 15, p. 1802119, 2019, doi: 10.1002/advs.201802119.
- [21] S. I. Azzam and A. V. Kildishev, "Photonic Bound States in the Continuum: From Basics to Applications," *Adv. Optical Mater.*, vol. 9, no. 1, p. 2001469, 2021, doi: 10.1002/adom.202001469.
- [22] K. Koshelev, Y. Tang, K. Li, D.-Y. Choi, G. Li, and Y. Kivshar, "Nonlinear Metasurfaces Governed by Bound States in the Continuum," *ACS Photonics*, vol. 6, no. 7, pp. 1639–1644, 2019, doi: 10.1021/acsp Photonics.9b00700.
- [23] C. F. Bohren and D. R. Huffman, *Absorption and Scattering of Light by Small Particles*. New York, Chichester, Brisbane, Toronto, Singapore: John Wiley & Sons, Ltd, 1998. Accessed: Jun. 8 2022. [Online]. Available: <https://onlinelibrary.wiley.com/doi/book/10.1002/9783527618156>

- [24] F. W. Went, "Blue Hazes in the Atmosphere," *Nature*, vol. 187, no. 4738, pp. 641–643, 1960, doi: 10.1038/187641a0.
- [25] F. Papoff and B. Hourahine, "Geometrical Mie theory for resonances in nanoparticles of any shape," *Opt. Express*, vol. 19, no. 22, pp. 21432–21444, 2011, doi: 10.1364/OE.19.021432.
- [26] G. Mie, "Beiträge zur Optik trüber Medien, speziell kolloidaler Metallösungen," *Ann. Phys.*, vol. 330, no. 3, pp. 377–445, 1908, doi: 10.1002/andp.19083300302.
- [27] *Particle size analysis: Laser diffraction methods*, 13320, International Organization for Standardization, Jan. 2020. [Online]. Available: <https://www.iso.org/standard/69111.html>
- [28] C. D. Stevens, *Clinical immunology & serology: A laboratory perspective*, 3rd ed. Philadelphia, PA: F.A. Davis, 2010. [Online]. Available: <http://lib.myilibrary.com/detail.asp?id=249568>
- [29] A. S. Solntsev, G. S. Agarwal, and Y. S. Kivshar, "Metasurfaces for quantum photonics," *Nat. Photonics*, vol. 15, no. 5, pp. 327–336, 2021, doi: 10.1038/s41566-021-00793-z.
- [30] S. Wang *et al.*, "Broadband achromatic optical metasurface devices," *Nat. Commun.*, vol. 8, no. 1, p. 187, 2017, doi: 10.1038/s41467-017-00166-7.
- [31] C. Gigli, "Second harmonic generation and control in dielectric metasurfaces," Dissertation, Matériaux et Phénomènes Quantiques, Université de Paris, Paris, 2021. Accessed: May 10 2022.
- [32] J. D. Jackson, *Classical electrodynamics*, 3rd ed. Hoboken, NY: Wiley-VCH Verlag GmbH & Co. KGaA, 2009.
- [33] $3e\phi p$, *VSHwiki.svg: Vector spherical harmonics (Magnetic and electric multipoles, far-fields, until order $n=3$)*. [Online]. Available: <https://commons.wikimedia.org/w/index.php?curid=85346484> (accessed: Jan. 23 2022).
- [34] L. Xu *et al.*, "Boosting third-harmonic generation by a mirror-enhanced anapole resonator," *Light Sci. Appl.*, vol. 7, no. 1, pp. 1–8, 2018, doi: 10.1038/s41377-018-0051-8.
- [35] Tianji Liu, Rongyang Xu, Peng Yu, Zhiming Wang, and Junichi Takahara, "Multipole and multimode engineering in Mie resonance-based metastructures," *Nanophotonics*, vol. 9, no. 5, pp. 1115–1137, 2020, doi: 10.1515/nanoph-2019-0505.

- [36] W. Fuhs, "Amorphous Hydrogenated Silicon, a-Si:H," in *Silicon: Evolution and Future of a Technology*, P. Siffert and E. F. Krimmel, Eds., Berlin, Heidelberg: Springer Berlin Heidelberg, 2004, pp. 123–137.
- [37] S. E. Geißendörfer, "Numerische Simulationen von Dünnschichtsolarzellen aus amorphem und mikrokristallinem Silizium Modellvalidierung und Einflüsse der Substrattopographie auf die elektrischen Solarzeleigenschaften," Dissertation, Institut für Physik, Carl von Ossietzky Universität Oldenburg, Oldenburg, 2013. Accessed: Jun. 8 2022. [Online]. Available: <http://oops.uni-oldenburg.de/1428/>
- [38] X. L. Yang and S. W. Xie, "Expression of third-order effective nonlinear susceptibility for third-harmonic generation in crystals," *Appl. Opt.*, vol. 34, no. 27, pp. 6130–6135, 1995, doi: 10.1364/AO.34.006130.
- [39] C. L. Tang and Herbert Rabin, "Selection Rules for Circularly Polarized Waves in Nonlinear Optics," *Phys. Rev. B*, vol. 3, no. 12, p. 4025, 1971, doi: 10.1103/PhysRevB.3.4025.
- [40] C. Schinke *et al.*, "Uncertainty analysis for the coefficient of band-to-band absorption of crystalline silicon," *AIP Advances*, vol. 5, no. 6, p. 67168, 2015, doi: 10.1063/1.4923379.
- [41] N. K. Hon, R. Soref, and B. Jalali, "The third-order nonlinear optical coefficients of Si, Ge, and Si_{1-x}Ge_x in the midwave and longwave infrared," *J. Appl. Phys.*, vol. 110, no. 1, p. 11301, 2011, doi: 10.1063/1.3592270.
- [42] T. Amotchkina, M. Trubetskov, D. Hahner, and V. Pervak, "Characterization of e-beam evaporated Ge, YbF₃, ZnS, and LaF₃ thin films for laser-oriented coatings," *Appl. Opt.*, vol. 59, no. 5, A40-A47, 2020, doi: 10.1364/AO.59.000A40.
- [43] K. Papatryfonos *et al.*, "Refractive indices of MBE-grown Al_xGa_(1-x)As ternary alloys in the transparent wavelength region," *AIP Advances*, vol. 11, no. 2, p. 25327, 2021, doi: 10.1063/5.0039631.
- [44] A. Zilli *et al.*, "Frequency Tripling via Sum-Frequency Generation at the Nanoscale," *ACS Photonics*, vol. 8, no. 4, pp. 1175–1182, 2021, doi: 10.1021/acsphotonics.1c00112.
- [45] T. Siefke *et al.*, "Materials Pushing the Application Limits of Wire Grid Polarizers further into the Deep Ultraviolet Spectral Range," *Advanced Optical Materials*, vol. 4, no. 11, pp. 1780–1786, 2016, doi: 10.1002/adom.201600250.
- [46] X. Guan, H. Hu, L. K. Oxenløwe, and L. H. Frandsen, "Compact titanium dioxide waveguides with high nonlinearity at telecommunication wavelengths," *Opt. Express*, vol. 26, no. 2, pp. 1055–1063, 2018, doi: 10.1364/OE.26.001055.

- [47] W. L. Bond, "Measurement of the Refractive Indices of Several Crystals," *J. Appl. Phys.*, vol. 36, no. 5, pp. 1674–1677, 1965, doi: 10.1063/1.1703106.
- [48] A. Zappettini *et al.*, "Wavelength dependence of the third order non - linear coefficient in hydrothermally grown ZnO crystals," *phys. stat. sol. (c)*, vol. 1, no. 4, pp. 997–1000, 2004, doi: 10.1002/pssc.200304274.
- [49] P. E. Powers, *Field Guide to Nonlinear Optics*. Bellingham: Society of Photo-Optical Instrumentation Engineers (SPIE), 2013. [Online]. Available: <https://ebookcentral.proquest.com/lib/kxp/detail.action?docID=1386869>
- [50] Luca Carletti, Sergey S. Kruk, Andrey A. Bogdanov, Costantino De Angelis, and Yuri Kivshar, "High-harmonic generation at the nanoscale boosted by bound states in the continuum," *Phys. Rev. Research*, vol. 1, no. 2, p. 23016, 2019, doi: 10.1103/PhysRevResearch.1.023016.
- [51] M. R. Shcherbakov *et al.*, "Enhanced third-harmonic generation in silicon nanoparticles driven by magnetic response," *Nano Lett.*, vol. 14, no. 11, pp. 6488–6492, 2014, doi: 10.1021/nl503029j.
- [52] G. Grinblat, Y. Li, M. P. Nielsen, R. F. Oulton, and S. A. Maier, "Efficient Third Harmonic Generation and Nonlinear Subwavelength Imaging at a Higher-Order Anapole Mode in a Single Germanium Nanodisk," *ACS Nano*, vol. 11, no. 1, pp. 953–960, 2017, doi: 10.1021/acsnano.6b07568.
- [53] Zhuojun Liu *et al.*, "High-Q Quasibound States in the Continuum for Nonlinear Metasurfaces," *Phys. Rev. Lett.*, vol. 123, no. 25, p. 253901, 2019, doi: 10.1103/PhysRevLett.123.253901.
- [54] M. W. Klein, M. Wegener, N. Feth, and S. Linden, "Experiments on second- and third-harmonic generation from magnetic metamaterials," *Opt. Express*, vol. 15, no. 8, pp. 5238–5247, 2007, doi: 10.1364/OE.15.005238.
- [55] M. A. Green, "Self-consistent optical parameters of intrinsic silicon at 300K including temperature coefficients," *Solar Energy Materials and Solar Cells*, vol. 92, no. 11, pp. 1305–1310, 2008, doi: 10.1016/j.solmat.2008.06.009.
- [56] P. B. Johnson and R. W. Christy, "Optical Constants of the Noble Metals," *Phys. Rev. B*, vol. 6, no. 12, pp. 4370–4379, 1972, doi: 10.1103/PhysRevB.6.4370.

- [57] G. Rosenblatt, B. Simkhovich, G. Bartal, and M. Orenstein, "Nonmodal Plasmonics: Controlling the Forced Optical Response of Nanostructures," *Phys. Rev. X*, vol. 10, no. 1, p. 11071, 2020, doi: 10.1103/PhysRevX.10.011071.
- [58] C. Gigli *et al.*, "Tensorial phase control in nonlinear meta-optics," *Optica*, vol. 8, no. 2, p. 269, 2021, doi: 10.1364/OPTICA.413329.
- [59] L. Carletti, A. Locatelli, O. Stepanenko, G. Leo, and C. De Angelis, "Enhanced second-harmonic generation from magnetic resonance in AlGaAs nanoantennas," *Opt. Express*, vol. 23, no. 20, pp. 26544–26550, 2015, doi: 10.1364/OE.23.026544.
- [60] B. Reineke *et al.*, "Silicon Metasurfaces for Third Harmonic Geometric Phase Manipulation and Multiplexed Holography," *Nano letters*, vol. 19, no. 9, pp. 6585–6591, 2019, doi: 10.1021/acs.nanolett.9b02844.
- [61] Allresist DE, *Allresist: Innovation, Kreativität, kundenspezifische Lösungen*. [Online]. Available: <https://www.allresist.de/> (accessed: Mar. 1 2022).
- [62] Rafael Abargues Lopez, "Conducting polymers as charge dissipator layers for electron beam lithography," Dissertation, Naturwissenschaftliche Fakultät, Friedrich-Alexander-Universität Erlangen-Nürnberg, Erlangen, 2006. [Online]. Available: https://www.researchgate.net/publication/221932402_Conducting_polymers_as_charge_dissipator_layers_for_electron_beam_lithography
- [63] Liming Ren and Baoqin Chen, "Proximity effect in electron beam lithography," in *Proceedings. 7th International Conference on Solid-State and Integrated Circuits Technology, 2004*, 2004, 579-582 vol.1.
- [64] G. S. May and S. M. Sze, *Fundamentals of semiconductor fabrication*. Hoboken, NJ: Wiley, 2004.
- [65] Samco, "What is the Bosch Process (Deep Reactive Ion Etching)?," *SAMCO Inc*, 10 Dec., 2020. <https://www.samcointl.com/what-is-the-bosch-process-deep-reactive-ion-etching/> (accessed: Mar. 2 2022).
- [66] W. Demtröder, *Experimentalphysik 2: Elektrizität und Optik*, 7th ed. Berlin, Heidelberg: Springer Berlin Heidelberg, 2017. [Online]. Available: <http://nbn-resolving.org/urn:nbn:de:bsz:31-epflicht-1562960>
- [67] P. C. D. Hobbs, *Building electro-optical systems: Making it all work*. Hoboken, NJ: John Wiley & Sons, Ltd, 2022. [Online]. Available: <https://onlinelibrary.wiley.com/doi/book/10.1002/9781119439080>

- [68] A. Vijayakumar, *Design and Fabrication of Diffractive Optical Elements with MATLAB*. Bellingham: Society of Photo-Optical Instrumentation Engineers (SPIE), 2017. [Online]. Available: <https://ebookcentral.proquest.com/lib/kxp/detail.action?docID=4947323>
- [69] Carlo Gigli, Qitong Li, Pierre Chavel, Giuseppe Leo, Mark L. Brongersma, and Philippe Lalanne, "Fundamental Limitations of Huygens' Metasurfaces for Optical Beam Shaping," *Laser & Photonics Reviews*, vol. 15, no. 8, p. 2000448, 2021, doi: 10.1002/lpor.202000448.
- [70] Y. Kivshar and A. Miroshnichenko, "Meta-Optics with Mie Resonances," *Optics & Photonics News*, 01 Jan., 2017. https://www.optica-opn.org/home/articles/volume_28/january_2017/features/meta-optics_with_mie_resonances/ (accessed: Mar. 1 2022).
- [71] B. Sain, C. Meier, and T. Zentgraf, "Nonlinear optics in all-dielectric nanoantennas and metasurfaces: a review," *AP*, vol. 1, no. 02, p. 1, 2019, doi: 10.1117/1.AP.1.2.024002.
- [72] C. Pfeiffer and A. Grbic, "Metamaterial Huygens' surfaces: tailoring wave fronts with reflectionless sheets," *Phys. Rev. Lett.*, vol. 110, no. 19, p. 197401, 2013, doi: 10.1103/PhysRevLett.110.197401.
- [73] C. Schlickriede, S. S. Kruk, L. Wang, B. Sain, Y. Kivshar, and T. Zentgraf, "Nonlinear Imaging with All-Dielectric Metasurfaces," *Nano Lett.*, vol. 20, no. 6, pp. 4370–4376, 2020, doi: 10.1021/acs.nanolett.0c01105.
- [74] J. D. Sautter *et al.*, "Tailoring Second-Harmonic Emission from (111)-GaAs Nanoantennas," *Nano Lett.*, vol. 19, no. 6, pp. 3905–3911, 2019, doi: 10.1021/acs.nanolett.9b01112.
- [75] V. F. Gili *et al.*, "Monolithic AlGaAs second-harmonic nanoantennas," *Opt. Express*, vol. 24, no. 14, pp. 15965–15971, 2016, doi: 10.1364/OE.24.015965.
- [76] J. S. Gomez-Diaz, M. Tymchenko, J. Lee, M. A. Belkin, and A. Alù, "Nonlinear processes in multi-quantum-well plasmonic metasurfaces: Electromagnetic response, saturation effects, limits, and potentials," *Phys. Rev. B*, vol. 92, no. 12, p. 125429, 2015, doi: 10.1103/PhysRevB.92.125429.
- [77] J. Lee *et al.*, "Giant nonlinear response from plasmonic metasurfaces coupled to intersubband transitions," *Nature*, vol. 511, no. 7507, pp. 65–69, 2014, doi: 10.1038/nature13455.
- [78] M. Tymchenko, J. S. Gomez-Diaz, J. Lee, N. Nookala, M. A. Belkin, and A. Alù, "Gradient Nonlinear Pancharatnam-Berry Metasurfaces," *Phys. Rev. Lett.*, vol. 115, no. 20, p. 207403, 2015, doi: 10.1103/PhysRevLett.115.207403.

- [79] B. Liu *et al.*, “Nonlinear Wavefront Control by Geometric - Phase Dielectric Metasurfaces: Influence of Mode Field and Rotational Symmetry,” *Adv. Optical Mater.*, vol. 8, no. 9, p. 1902050, 2020, doi: 10.1002/adom.201902050.
- [80] E. Hecht, *Optik*, 5th ed. München: Oldenbourg, 2009. [Online]. Available: http://subhh.ciando.com/book/?bok_id=22613
- [81] Y. Yang *et al.*, “Nonlinear Fano-Resonant Dielectric Metasurfaces,” *Nano Lett.*, vol. 15, no. 11, pp. 7388–7393, 2015, doi: 10.1021/acs.nanolett.5b02802.
- [82] Shumei Chen *et al.*, “Symmetry-Selective Third-Harmonic Generation from Plasmonic Metacrystals,” *Phys. Rev. Lett.*, vol. 113, no. 3, p. 33901, 2014, doi: 10.1103/PhysRevLett.113.033901.
- [83] G. K. Ackermann and J. Eichler, *Holography: A Practical Approach*: John Wiley & Sons, 2007.
- [84] R. Gerchberg and W.O. Saxton, “A practical algorithm for the determination of phase from image and diffraction plane pictures,” *Optik*, vol. 35, pp. 237–246, 1972. [Online]. Available: <https://www.semanticscholar.org/paper/A-practical-algorithm-for-the-determination-of-from-Gerschberg/5a114d3050a0a33f8cc6d28d55fa048a5a7ab6f2>
- [85] E. R. Dufresne, G. C. Spalding, M. T. Dearing, S. A. Sheets, and D. G. Grier, “Computer-generated holographic optical tweezer arrays,” 3, 2000. [Online]. Available: <https://arxiv.org/pdf/cond-mat/0008414>
- [86] D. C. Marinica, A. G. Borisov, and S. V. Shabanov, “Bound States in the continuum in photonics,” *Phys. Rev. Lett.*, vol. 100, no. 18, p. 183902, 2008, doi: 10.1103/PhysRevLett.100.183902.
- [87] C. W. Hsu, B. Zhen, A. D. Stone, J. D. Joannopoulos, and M. Soljačić, “Bound states in the continuum,” *Nat. Rev. Mater.*, vol. 1, no. 9, pp. 1–13, 2016, doi: 10.1038/natrevmats.2016.48.
- [88] K. Koshelev, G. Favraud, A. Bogdanov, Y. Kivshar, and A. Fratalocchi, “Nonradiating photonics with resonant dielectric nanostructures,” *Nanophotonics*, vol. 8, no. 5, pp. 725–745, 2019, doi: 10.1515/nanoph-2019-0024.
- [89] M. V. Rybin *et al.*, “High-Q Supercavity Modes in Subwavelength Dielectric Resonators,” *Phys. Rev. Lett.*, vol. 119, no. 24, p. 243901, 2017, doi: 10.1103/PhysRevLett.119.243901.

- [90] Adam C. Overvig, Stephanie C. Malek, Michael J. Carter, Sajan Shrestha, and Nanfang Yu, "Selection rules for quasibound states in the continuum," *Phys. Rev. B*, vol. 102, no. 3, p. 35434, 2020, doi: 10.1103/PhysRevB.102.035434.
- [91] Z. Sadrieva, K. Frizyuk, M. Petrov, Y. Kivshar, and A. Bogdanov, "Multipolar origin of bound states in the continuum," *Phys. Rev. B*, vol. 100, no. 11, p. 115303, 2019, doi: 10.1103/PhysRevB.100.115303.
- [92] C. W. Hsu *et al.*, "Observation of trapped light within the radiation continuum," *Nature*, vol. 499, no. 7457, pp. 188–191, 2013, doi: 10.1038/nature12289.
- [93] S. T. Ha *et al.*, "Directional lasing in resonant semiconductor nanoantenna arrays," *Nat. Nanotechnol.*, vol. 13, no. 11, pp. 1042–1047, 2018, doi: 10.1038/s41565-018-0245-5.
- [94] K. Koshelev, S. Lepeshov, M. Liu, A. Bogdanov, and Y. Kivshar, "Asymmetric Metasurfaces with High-Q Resonances Governed by Bound States in the Continuum," *Phys. Rev. Lett.*, vol. 121, no. 19, p. 193903, 2018, doi: 10.1103/PhysRevLett.121.193903.
- [95] P. P. Vabishchevich, S. Liu, M. B. Sinclair, G. A. Keeler, G. M. Peake, and I. Brener, "Enhanced Second-Harmonic Generation Using Broken Symmetry III–V Semiconductor Fano Metasurfaces," *ACS Photonics*, vol. 5, no. 5, pp. 1685–1690, 2018, doi: 10.1021/acsp Photonics.7b01478.
- [96] M. R. Shcherbakov *et al.*, "Enhanced Third-Harmonic Generation in Silicon Nanoparticles Driven by Magnetic Response," *Nano Lett.*, vol. 14, no. 11, pp. 6488–6492, 2014, doi: 10.1021/nl503029j.
- [97] B. Reineke Matsudo *et al.*, "Efficient Frequency Conversion with Geometric Phase Control in Optical Metasurfaces," *Advanced Science*, vol. 9, no. 12, e2104508, 2022, doi: 10.1002/advs.202104508.
- [98] B. Metzger, "Ultrafast nonlinear plasmonics : from dipole nanoantennas to hybrid complex plasmonic structures," Dissertation, Fakultät Mathematik und Physik, Universität Stuttgart, Stuttgart, 2014. [Online]. Available: <https://elib.uni-stuttgart.de/handle/11682/5152>
- [99] Y. Yang, I. I. Kravchenko, D. P. Briggs, and J. Valentine, "All-dielectric metasurface analogue of electromagnetically induced transparency," *Nat. Commun.*, vol. 5, no. 1, p. 5753, 2014, doi: 10.1038/ncomms6753.
- [100] M. F. Limonov, M. V. Rybin, A. N. Poddubny, and Y. S. Kivshar, "Fano resonances in photonics," *Nat. Photonics*, vol. 11, no. 9, pp. 543–554, 2017, doi: 10.1038/nphoton.2017.142.

- [101] K. J. Vahala, "Optical microcavities," *Nature*, vol. 424, no. 6950, pp. 839–846, 2003, doi: 10.1038/nature01939.
- [102] J. Kühne, J. Wang, T. Weber, L. Kühner, S. A. Maier, and A. Tittl, "Fabrication robustness in BIC metasurfaces," *Nanophotonics*, vol. 10, no. 17, pp. 4305–4312, 2021, doi: 10.1515/nanoph-2021-0391.
- [103] H. Toutenburg, "Mardia, K. V./Kent, J. T./Bibby, J. M., Multivariate Analysis. London-New York-Toronto-Sydney-San Francisco, Academic Press 1979. XV, 521 S., \$ 34.00 P/B. ISBN 0-12-471252-5," *Z. angew. Math. Mech.*, vol. 61, 3-5, p. 206, 1981, doi: 10.1002/zamm.19810610315.
- [104] L. Papula, *Mathematik für Ingenieure und Naturwissenschaftler*, 13th ed. Wiesbaden: Springer Vieweg, 2012.
- [105] I. A. Erteza, "Diffraction efficiency analysis for multi-level diffractive optical elements," Sandia National Laboratories SAND--95-1697, 1995. [Online]. Available: <https://digital.library.unt.edu/ark:/67531/metadc620317/>
- [106] I. N. Bronstein, H. Mühlig, G. Musiol, and K. A. Semendjajew, *Taschenbuch der Mathematik (Bronstein)*, 10th ed. Haan: Europa-Lehrmittel, 2016. [Online]. Available: http://www.europa-lehrmittel.de/t-1/taschenbuch_der_mathematik_bronstein-2657/presseinformation/9783808557891.pdf
- [107] S. Zhang, L. Huang, G. Geng, J. Li, X. Li, and Y. Wang, "Full-Stokes polarization transformations and time sequence metasurface holographic display," *Photon. Res.*, vol. 10, no. 4, p. 1031, 2022, doi: 10.1364/PRJ.450354.
- [108] Zemax, *Zemax CTO Insights: Optics Role in Developing Consumer Electronics*. [Online]. Available: <https://web.archive.org/web/20210901215614/https://www.zemax.com/blogs/news/cto-industry-insights-august-2021> (accessed: Apr. 20 2022.071Z).
- [109] LIGHT CONVERSION, *GECO*. [Online]. Available: <https://web.archive.org/web/20210613131659/https://lightcon.com/product/geco-scanning-autocorrelator/#drawings> (accessed: Apr. 20 2022.062Z).
- [110] N. Karl *et al.*, "Frequency Conversion in a Time-Variant Dielectric Metasurface," *Nano Lett.*, vol. 20, no. 10, pp. 7052–7058, 2020, doi: 10.1021/acs.nanolett.0c02113.
- [111] Z. Han and Y. Cai, "All-optical self-switching with ultralow incident laser intensity assisted by a bound state in the continuum," *Opt. Lett.*, vol. 46, no. 3, pp. 524–527, 2021, doi: 10.1364/OL.415531.

- [112] T. Santiago-Cruz *et al.*, “Photon Pairs from Resonant Metasurfaces,” *Nano Lett.*, vol. 21, no. 10, pp. 4423–4429, 2021, doi: 10.1021/acs.nanolett.1c01125.
- [113] Matthew Parry, Andrea Mazzanti, Alexander N. Poddubny, Giuseppe Della Valle, Dragomir N. Neshev, and Andrey A. Sukhorukov, “Enhanced generation of nondegenerate photon pairs in nonlinear metasurfaces,” *AP*, vol. 3, no. 5, p. 55001, 2021, doi: 10.1117/1.AP.3.5.055001.
- [114] S. E. Harris, M. K. Oshman, and R. L. Byer, “Observation of Tunable Optical Parametric Fluorescence,” *Phys. Rev. Lett.*, vol. 18, no. 18, pp. 732–734, 1967, doi: 10.1103/PhysRevLett.18.732.
- [115] Giuseppe Marino *et al.*, “Spontaneous photon-pair generation from a dielectric nanoantenna,” *Optica*, vol. 6, no. 11, pp. 1416–1422, 2019, doi: 10.1364/OPTICA.6.001416.
- [116] Anna Nikolaeva, Kristina Frizyuk, Nikita Olekhno, Alexander Solntsev, and Mihail Petrov, “Directional emission of down-converted photons from a dielectric nanoresonator,” *Phys. Rev. A*, vol. 103, no. 4, p. 43703, 2021, doi: 10.1103/PhysRevA.103.043703.

Chapter 8 Appendix

8.1 Journal Publication during PhD

- **Silicon Metasurfaces for Third Harmonic Geometric Phase Manipulation and Multiplexed Holography**
Bernhard Reineke, Basudeb Sain, Ruizhe Zhao, Luca Carletti, Bingyi Liu, Lingling Huang, Costantino De Angelis, and Thomas Zentgraf
Nano Letters. 2019, 19, 9, 6585–6591
- **Nonlinear Wavefront Control by Geometric-Phase Dielectric Metasurfaces: Influence of Mode Field and Rotational Symmetry**
Bingyi Liu, Basudeb Sain, **Bernhard Reineke**, Ruizhe Zhao, Cedrik Meier, Lingling Huang, Yongyuan Jiang, and Thomas Zentgraf
Advanced Optical Materials 2020, 8, 1902050
- **Efficient Frequency Conversion with Geometric Phase Control in Optical Metasurfaces**
Bernhard Reineke Matsudo, Basudeb Sain, Luca Carletti, Xue Zhang, Wenlong Gao, Costantino de Angelis, Lingling Huang, and Thomas Zentgraf
Advanced Science 2022, 9, 210450

8.2 Conference Presentations

- **Efficient Frequency Conversion with Geometric Phase Control in Optical Metasurfaces**
Bernhard Reineke Matsudo, Basudeb Sain, Luca Carletti, Xue Zhang, Wenlong Gao, Costantino de Angelis, Lingling Huang, and Thomas Zentgraf
Nanometa, 8th International Topical Meeting on Nanophotonics and Metamaterials, 2022, **Oral**, as substitute for Basudeb Sain
- **Third Harmonic Wavefront Control and Multiplexed Holography with a Pancharatnam-Berry Phase Silicon Metasurface**
Bernhard Reineke, Basudeb Sain, Ruizhe Zhao, Luca Carletti, Bingyi Liu, Lingling Huang, Costantino De Angelis, and Thomas Zentgraf
Metamaterials, The 14th International Congress on Artificial Materials for Novel Wave Phenomena, 2020, **Oral**

8.3 Other Contributions

- **Imaging through nonlinear metalens using second harmonic generation**
Christian Schlickriede, Naomi Waterman, **Bernhard Reineke**, Philip Georgi, Guixin Li, Shuang Zhang, and Thomas Zentgraf
Advanced Materials 30 (8), 1703843
- **Volumetric Generation of Optical Vortices with Metasurfaces**
Lingling Huang, Xu Song, **Bernhard Reineke**, Tianyou Li, Xiaowei Li, Juan Liu, Shuang Zhang, Yongtian Wang, and Thomas Zentgraf
ACS Photonics 2017, 4, 2, 338–346
- **Strong nonlinear optical activity induced by lattice surface modes on plasmonic metasurface**
Shumei Chen, **Bernhard Reineke**, Guixin Li, Thomas Zentgraf, and Shuang Zhang
Nano Letters 19 (9), 6278–6283
- **Simultaneous Spectral and Spatial Modulation for Color Printing and Holography Using All-Dielectric Metasurfaces**
Qunshuo Wei, Basudeb Sain, Yongtian Wang, **Bernhard Reineke**, Xiaowei Li, Lingling Huang, and Thomas Zentgraf
Nano Letters 19 (9), 6278–6283
- **Reconfigurable metasurface hologram by utilizing addressable dynamic pixels**
Tianyou Li, Qunshuo Wei, **Bernhard Reineke**, Felicitas Walter, Yongtian Wang, Thomas Zentgraf, and Lingling Huang
Optics Express 27 (15), 21153–21162
- **Selective Etching of (111)B-Oriented Al_xGa_{1-x}As-Layers for Epitaxial Lift-Off**
Tobias Henksmeier, Martin Eppinger, **Bernhard Reineke**, Thomas Zentgraf, Cedrik Meier, and Dirk Reuter
physica status solidi (a) 218 (3), 2000408
- **Electrically switchable metasurface for beam steering using PEDOT polymers**
Juliane Ratzsch, Julian Karst, Jinglin Fu, Monika Ubl, Tobias Pohl, Florian Sterl, Claudia Malacrida, Matthias Wieland, **Bernhard Reineke**, Thomas Zentgraf, Sabine Ludwigs, Mario Hentschel, and Harald Giessen
Journal of Optics 22 (12), 124001

Chapter 9 Acknowledgements

I would like to express my sincere gratitude to the people who accompanied me on the way to completing this work. Without your support this project would not have been possible.

I am deeply indebted to Prof. Dr. Thomas Zentgraf for giving me the opportunity to work on my dissertation and contribute to the scientific community. I am grateful for the patient guidance, encouragement, and advice he gave me during my time as a student. He has assembled an extraordinary team, and I am proud to be a part of it. Great thanks are also due to Prof. Dr. Cedrik Meier for reviewing this work and his contributions to our scientific publications. Many thanks to Prof. Dr. Thorsten Meier and to Dr. Marc Sartison for reviewing my work and serving on the committee.

Over the past few years, I have had the opportunity to work with many people who have become good friends. Dr. Felicitas Walther, Dr. Daniel Frese, René Geromel, Dr. Christian Schlickriede, Dr. Florian Spreyer, Dr. Wenlong Gao and Philip Georgi. We had a lot of fun in the office and helped each other with any problems along the way. A special thanks to Dr. Basudeb Sain for his help and support during his time in Paderborn. I learned a lot from his expertise. It was a pleasure to work and spend time with all of you. I have had the pleasure of working with great scientists: Dr. Lingling Huang, Ruizhe Zhao, Xue Zhang, Dr. Bingyi Liu, Dr. Luca Carletti, and Dr. Costantino De Angelis, who have supported me in many projects. I thank you all for the good cooperation.

I would like to express my deepest appreciation to my wife Sandra Harumi Reineke Matsudo for her love, trust, and support during difficult times. I would also like to thank my parents Anette and Willi Reineke. Without their great understanding and encouragement over the past few years, it would have been impossible for me to complete my studies.